A Three-Dimensional Numerical Model of an Anion Exchange Membrane Fuel Cell

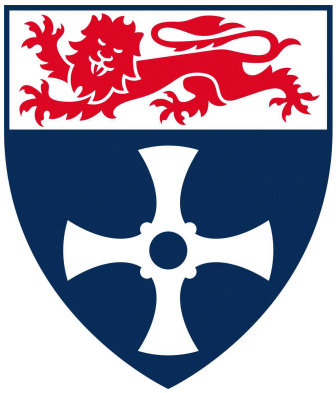

Bruno de Souza Machado

School of Engineering

Newcastle University

This dissertation is submitted for the degree of

Doctor of Philosophy

November, 2018

This thesis is dedicated to my parents and wife.
We did it.

Declaration

I hereby declare that except where specific reference is made to the work of others, the contents of this dissertation are original and have not been submitted in whole or in part for consideration for any other degree or qualification in this, or any other University. This dissertation is the result of my own work and includes nothing which is the outcome of work done in collaboration, except where specifically indicated in the text. This dissertation contains approximately 37000 words including appendices, bibliography, footnotes, tables and equations and has 37 figures.

Bruno de Souza Machado
November, 2018

Acknowledgements

Firstly, I would like to express my sincere gratitude to my supervisor, Prof. Nilanjan Chakraborty for his relentless support, inspiration, guidance and encouragement during the challenges faced throughout this PhD. I am truly thankful to have you as my mentor. I am also grateful to Dr Prodip K. Das and Dr. Mohamed Mamlouk for the support provided during this journey.

I would like to extend my gratitude to my colleagues in T4 office: Dr Dipal Patel, Dr Jiawei Lai, Dr Sahin Yigit, Sam Wood, Chris Stafford, Gulcan Ozel, Bill Papapostolou, Ilias Konstantinou and Lizhong Yi. The countless cups of coffee and discussions we had together were essential to the completion of this thesis.

The financial support of Coordenacao de Aperfeicoamento de Pessoal de Nivel Superior (CAPES) through the Science without Borders Project (Grant n. BEX / 13011-13-8) is gratefully acknowledged.

This work is also dedicated to my parents, Silvia and Omar, who have always supported me in all possible ways throughout this journey.

Last but not least, I would like to thank my dear wife Caroline for continuously and patiently supporting me during this entire journey. Your encouragement when the times got rough are much appreciated and duly noted.

Abstract

The global demand for alternative energy conversion procedures has increased considerably in the past few decades. As a result, increasing attention has been given to proton exchange membrane fuel cells as they offers several advantages over fossil fuel engines such as high efficiency, high power density and the absence of greenhouse gas emission to name a few. Polymer exchange membranes can be classified as either proton exchange membrane or anion exchange membrane (AEM). The latter has several distinct advantages including the possibility of precious metal free catalysts, enhanced oxygen reduction catalysis, and a wider option of fuels. Even though significant progress has been made on the experiment analysis of the AEM fuel cells, further improvement of the current numerical models is necessary in order to better describe the transportation phenomena within the catalyst layer and to enhance the accuracy of the numerical results.

The numerical simulation presented in this thesis is performed applying the methodologies of computational fluid dynamics. A finite volume method-based methodology was used and conservation equations of mass, momentum, species, liquid water, membrane water content, electronic and ionic potential and energy were solved in a coupled manner. The SIMPLE algorithm was used to link velocity and pressure. Grid sensitivity and convergence criteria analysis were performed in order to ensure that the grid size does not significantly affect the solution and that the numerical solution is converged.

In this thesis, firstly, a three-dimensional multiphase macro-homogeneous models is proposed which was subsequently used to evaluate the effects of operating temperature, inlet relative humidity, and flow direction (anode and cathode flowing in the same and opposite direction) on the overall performance of the fuel cell. Secondly, a three-dimensional multiphase agglomerate model for an AEM fuel cell is proposed and, in addition to the length scale present in the macro-

homogeneous model (i.e. catalyst layer thickness), an additional length scale is introduced (i.e. ionomer thickness) to the numerical model. Subsequently, a direct comparison is made between the proposed agglomerate model and the previously developed macro-homogeneous model and a detailed discussion between both models is presented. Finally, further improvement on the agglomerate model is proposed to mimic the transport phenomena within the catalyst layer in a more realistic manner and an investigation of the effects of the catalyst layer composition (i.e. platinum and carbon loading, ionomer loading), structural parameters (i.e. catalyst layer thickness, porosity) and operating parameters is performed.

List of Publication

- B. S. Machado, N. Chakraborty and P. K. Das. Influences of flow direction, temperature and relative humidity on the performance of a representative anion exchange membrane fuel cell: A computational analysis. International Journal of Hydrogen Energy, 42(9):6310 – 6323, 2017. ISSN 0360-3199. doi: https://doi.org/10.1016/j.ijhydene.2016.12.003.

- B. S. Machado, N. Chakraborty, M. Mamlouk and P. K. Das, "A Three-dimensional Agglomerate Model of an Anion Exchange Membrane Fuel Cell" Journal of Electrochemical Energy Conversion and Storage, 15, 0110004-1, 2018.

- B. S. Machado, M. Mamlouk and N. Chakraborty, "Three-dimensional agglomerate model of an anion exchange membrane fuel cell using air at the cathode – A parametric study." Journal of Power Sources, 2018.

Contents

List of Figures

List of Tables

Nomenclature

Roman Symbols

$\dot{q}$	heat flux (W/m^2)
$\mathcal{F}$	Faraday's constant 96485332.0$(C/kmol)$
$\mathcal{R}$	universal gas constantthe 8314 $(J/kmolK)$
$\vec{J}$	diffusive mass flux vector $(kmol/m^2s)$
$\vec{N}$	diffusion flux $(kmol/m^2s)$
$\vec{u}$	velocity (m/s)
a	specific area (m^2/m^3); water activity
A_s	reaction surface area per unit platinum mass (m^2/kg)
A_v	reaction surface area density (m^2/m^3)
B	pre-exponential factor
C	molar concentration $(kmol/m^3)$
C_p	specific heat $(J/kg \cdot K)$
D_i	species diffusivity (m^2/s)
E	reversible potential (V); total energy (J)
E_r	effectiveness factor
EW	equivalent molecular weight of dry membrane $(kg/kmol)$

G	Gibbs free energy (J/mol)
H	Henry's constant ($Pa \cdot m^2/mol$)
h	enthalpy (J); heat transfer coefficient ($W/m^2 \cdot K$)
I	unit tensor
J	current density (A/m^2)
J^{ref}	reference current density (A/m^3)
J_0	exchange current density (A/m^2)
J_0^{ref}	exchange current density at reference(A/m^2)
K	instrinsic permeability (m^2)
k	permeability (m^2)
k	reaction rate constant; reaction rate coefficient ($1/s$); thermal conductivity ($W/m \cdot K$)
k_B	Boltzmann constant $1.38064852 \times 10^{-23}$ ($m^2 \cdot kg/s^2 \cdot K$)
L	volume fraction
M	molecular weight ($kg/kmol$); chemical formula
m	mass loading (kg/m^2)
N	number of species; number of grid points
n	number of moles of electrons
n_d	electro-osmotic drag coefficient ($1/s$)
P	Pressure (Pa)
R	volumetric reaction rate (A/m^3)
r	radius (m)

RH	relative humidity
S	source term; entropy (J/K); entropy (J/K)
s	liquid water fraction
T	temperature (K)
T_0	inlet temperature (K)
T_∞	ambient temperature (K)
X	molar fraction
Y	mass fraction

Acronyms

3D	three-dimensional
ACL	anode catalyst layer
AEM	anion exchange membrane
BP	bipolar plate
CCL	cathode catalyst layer
CFD	computational fluid dynamics
CL	catalyst layer
CV	control volume
EOD	electro-osmotic drag
FC	flow channel
FDM	finite difference method
FEM	finite element method
FVM	finite volume method

GDL	gas diffusion layer
HOR	hydrogen oxidation reaction
IEC	ion exchange capacity
LHS	left hand side
ORR	oxygen reduction reaction
PEM	polymer exchange membrane
PEMFC	proton exchange membrane fuel cell
RHS	right hand side
UDF	user defined function

Greek Symbols

α	transfer coefficient
δ	thickness (m)
ϵ	porosity
η	overpotential (V)
γ	evaporation/condensation rate $(1/s)$
γ_e	ionomer water content factor
κ	electric conductivity (S/m)
λ	membrane water content
μ	dynamic viscosity $(kg/m \cdot s)$
ν	stoichiometric coefficient for the species involved in the reaction
Ω_D	diffusion collision integral
ϕ	electric potential (V)

ϕ_L	Thiele's modulus
Ψ	variable
ρ	density (kg/m^3)
σ	molecular raii ($\mathring{A}$); surface tension (N/m)
$\overline{\overline{\tau}}$	stress tensor
θ	contact angle ($\circ$)
θ	contact angle
φ	reaction order
ξ	stoichiometric ratio

Subscripts

agg	agglomerate
b	backward
C	Carbon
c	capillary pressure
CL	catalyst layer
$cond$	condensation
d	dissolved
e	equilibrium state
$evap$	evaporation
f	forward
i	the i^{th} component
k	phase k

l	liquid
lat	latent
M	ionomer
m	membrane
nb	neighboring cells
P	product
Pt/C	Platinum dispersed Carbon
Pt	Platinum
R	reactant
S	solid phase
sat	saturation
a	anode
abs	absolute
act	activation
c	cathode
cell	cell
con	concentration
g	gas phase
ij	binary
mass	mass
ohm	Ohmic
ref	reference

rev	reversible

Superscripts

eff	effective

Chapter 1

Introduction

1.1 Background

Over the last few decades, the concern regarding the environment and the sustainable energy conversion have driven researchers to the alternative energy conversion procedures. As one of the outcomes of the directed effort, polymer exchange membrane (PEM) fuel cell was developed as an alternative to fossil fuel heat engines. As a basic concept, a fuel cell is a device that from the chemical reaction between fuel and oxidant, directly converts the chemical energy into electrical energy [55]. On PEM fuel cells, hydrogen and oxygen are provided as fuel and oxidant, respectively, and as an outcome of the chemical reaction, three main products are generated: electrical energy, heat and water. Among several advantages of the PEM fuel cell are the lack of greenhouse gas emission and higher efficiency in comparison to internal combustion engines. These make the fuel cell a suitable option for several applications, including automotive, space station, satellites and power generators [5, 29, 37, 40, 64]. In addition to that, low operation temperature and noise production, fast start up and high power density are some other positive aspects of the fuel cells.

Nevertheless, even though PEM fuel cells have several advantages in comparison to other energy conversion devices, there are still technical issues that must be addressed before the widespread commercialisation, such as reliability, air management, water management, thermal management, cost, durability, etc. [1, 2]. In 2015, the specific power and cost for the fuel cell power systems oper-

ating on direct hydrogen is 659 W/kg and 53 $\$/kW_{net}$, respectively. Currently, the U.S. Energy Department aims to reduce the specific power and cost to 650 W/kg and 40 $\$/kW_{net}$, respectively, by 2020 [2]. In order to eliminate, or reduce, these disadvantages, an extensive research has been carried out by both experimental and numerical means. Both methods have advantages and disadvantages when compared to each other. Among the disadvantages of experimental work, when considered the transient mode of operation regime, the different spatial and temporal scales increase the complexity of measurement and observations. In addition to that, the high cost of equipment to produce a fuel cell (or a stack) is also an obstacle to experimental work. Alternatively to the experimental framework and the aforementioned experimental issues, the numerical simulation has been carried out in order to provide a better understanding of interrelated physicochemical phenomena involved in the energy conversion. In the past few decades, several studies have been carried out in order to provide more comprehensive numerical models capable to reproduce experimental results with higher accuracy. Further details about recent experimental and numerical studies will be presented in Chapter 2 of this thesis. Meanwhile, in the current chapter, the operation principles, components of a PEM fuel cell and objectives of this thesis are defined.

1.2 Operating Principles of Proton Exchange Membrane Fuel Cell

Typically, a proton exchange membrane fuel cell (PEMFC), which has an acidic solid membrane, operates with pure hydrogen at the anode side and humidified oxygen (or air) at the cathode side, as shown in Equations (1.1) and (1.2), respectively[21].

$$\frac{1}{2}O_2 + 2H^+ + 2e^- \rightarrow H_2O \ (cathode) \tag{1.1}$$

$$H_2 \rightarrow 2H^+ + 2e^- \ (anode) \tag{1.2}$$

As one can see in Equation (1.3), water, heat and electrical energy are produced as consequence to the oxygen reduction reaction (ORR) and the hydrogen

oxidation reaction (HOR) presented in Equations (1.1) and (1.2), respectively.

$$H_2 + \frac{1}{2}O_2 \rightarrow H_2O + heat + electrical\,energy \tag{1.3}$$

Even though PEMFCs have been extensive analysed in the existing literature, water flooding due to excessive water in the porous of the cathode electrolyte is still one of the challenges to the date [55].

1.3 Operating Principles of Anion Exchange Membrane Fuel Cell

In Figure 1.1, the operational principle of an anion exchange membrane (AEM) fuel cell is presented. As one can see, the anode and cathode side are separated by an AEM, as illustrated in Figure 1.1. Different than the acidic solid membrane from a PEMFC, the AEM creates an alkaline pH environment [21]. As a source of fuel and oxidant in an AEM fuel cell, typically hydrogen and oxygen (or air) are provided, respectively. On the cathode side, the ORR described in the Equation (1.4) occurs and the hydroxide ions (negatively charged) are formed. The formed ions diffuse through the ionomer content from the cathode catalyst layer (CCL) to the anode catalyst layer (ACL), crossing the AEM. On the ACL, the hydrogen supplied at the anode flow channel (FC) inlet and the hydroxide ions supplied from the cathode side are used in the HOR, represented by Equation (1.5), generating electrons and water molecules.

$$H_2O + 2e^- + \frac{1}{2}O_2 \rightarrow 2OH^-\ (cathode) \tag{1.4}$$

$$H_2 + 2OH^- \rightarrow 2H_2O + 2e^-\ (anode) \tag{1.5}$$

After crossing an external circuit, the electrons return to the cathode side to once again be part of the ORR. As a result from the combination of Equations (1.4) and (1.5), the Equation (1.6) describes the overall reaction of an AEM fuel

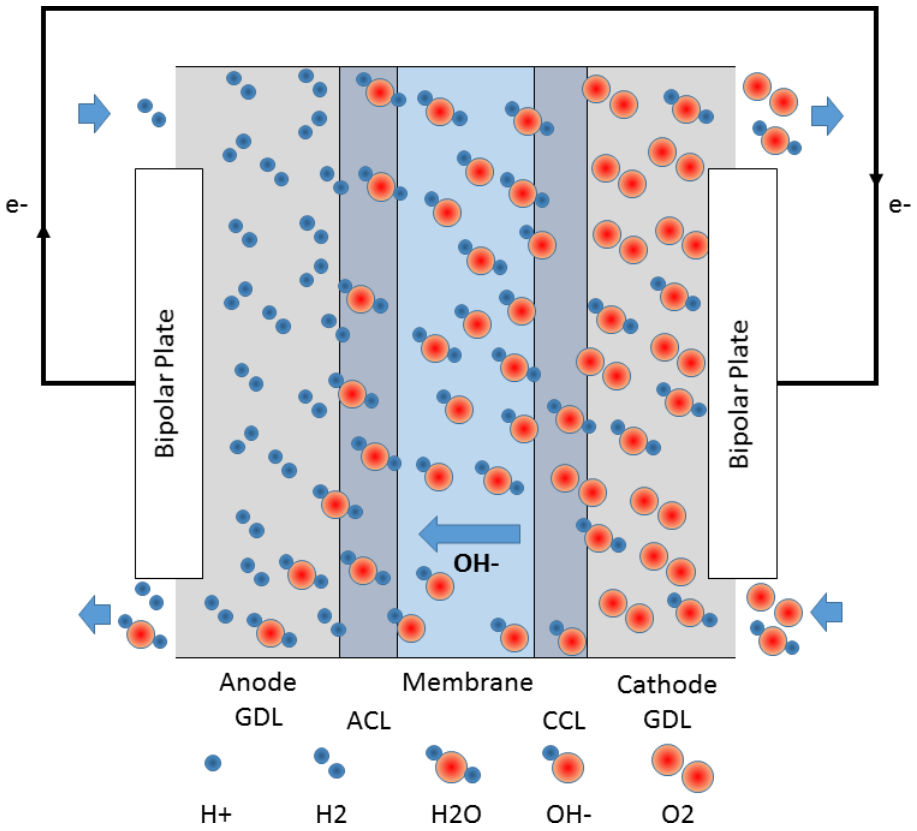

Figure 1.1: Operation principles of a AEM fuel cell.

cell.

$$H_2 + \frac{1}{2}O_2 \rightarrow H_2O + heat + electrical\,energy \tag{1.6}$$

As one can see from Equation (1.7), the Gibbs free energy, ΔG , of the fuel cell reaction is described as [70]:

$$\Delta G = -nFE \tag{1.7}$$

where n is the number of moles of electrons involved, E is the reversible potential and $\mathcal{F}$ is Faraday's constant (96485332.0 $C/kmol$). For the chemical reaction presented at Equation (1.6), the correspondent Gibbs free energy is -229 kJ/mol and the number of moles of electrons involved is $n = 2.0$ [70]. Therefore, the reversible potential for this electrochemical reaction is 1.229 V. Nevertheless, the theoretical voltage can not be obtained, even when operating at zero current

(open circuit), due to several irreversibilities presented in the AEM fuel cell energy conversion. Typically, a single AEM fuel cell operates between 0.4 to 0.8 V cell voltage and the produced current density is lower than 2.0 A/cm^2. Nevertheless, the order of the power produced by a PEM fuel cell can vary from as low as 1.0 W up to 106.0 W, depending on the amount of fuel cell stacks assembled. More detailed information about PEM fuel cell operation and applications can be found in [34, 50, 55].

1.4 Components of an AEM Fuel Cell

1.4.1 Polymer Exchange Membrane

The anion exchange membrane plays a critical role on the fuel cell performance, as it is being responsible for the diffusion of anions from cathode to anode and the blockage of electrons to cross through it, forcing them to cross an external circuit to generate electrical energy. The thickness of the membrane ranges from 0.02 to 0.3 mm, and it has a direct effect on the PEM fuel cell performance due to its relation with water diffusion rate and Ohmic loss. In order to obtain the optimum performance of the AEM fuel cell, water must be supplied in the right amount; excess or lack of water can cause flooding or drying of the membrane, respectively, therefore reducing electrical energy output [48].

1.4.2 Catalyst Layer

In the AEM fuel cell, the catalyst layer (CL) is where the half reaction takes place. Positioned directly in contact with the membrane and the gas diffusion layer, the CL is responsible for facilitating both hydrogen oxidation and oxygen reduction. As the CL composition has a direct impact on mass, ionic and electronic resistance, these transportation phenomena have to be taken into consideration when the CL is manufactured. For instance, in respect of the CL porosity, the augmentation of the CL porosity has a trade-off between the enhancement of the mass transportation and the increase of the ionic resistance [38] . With respect of the ionic phase, the CL is embedded in a matrix of ionomer, which plays an important role on the AEM fuel cell performance, facilitating the anions diffusion

from the CCL through the membrane until they reach the ACL [81]. The possibility of precious metal free CL makes the AEM fuel cell a feasible large scale production option, as it decreases the cost of the fuel cell [51].

1.4.3 Gas Diffusion Layer

With thickness ranging between 100 and 300 μm, the gas diffusion layer (GDL) is responsible for the conduction of electrons from and to the catalyst layer. In addition to that, it is also responsible to ensure that the reactants necessary for the electrochemical reaction reach the CL. Usually manufactured of carbon cloth or carbon paper, it presents a porous structure that is beneficial to keep the membrane hydrated [31]. In addition to that, the GDL can be coated with hydrophobic or hydroponic material, having an impact on the water management of AEM the fuel cell [49, 82].

1.4.4 Bipolar Plate

The bipolar plate (BP) is used to connect the cathode and anode of adjacent cells. Under normal operational condition, a single fuel cell produces a voltage smaller than 0.6 V (lower than the theoretical 1.229 V) due to irreversibilities and losses. When assembled in series, a fuel cell stack is capable to produce voltage in more useful quantities. In order to create a path to feed the GDL with reactants, a FC is embedded into the BP surface. Among several different designs, serpentine and parallel paths are widely used in literature and experimental work [12, 87]. The relation between the area of land and channel plays an important role since it affects the reactant supplies, cell weight and connections between GDL and BP. The Ohmic loss and contact resistance presented in the fuel cell can be reduced with the increase of the land area. In spite of that, a balance between land and flow channel area is necessary in order to ensure the supply of reactants as it is necessary. Some of the important characteristics of a BP are high electrical and thermal conductivity, chemical and mechanical strength [15].

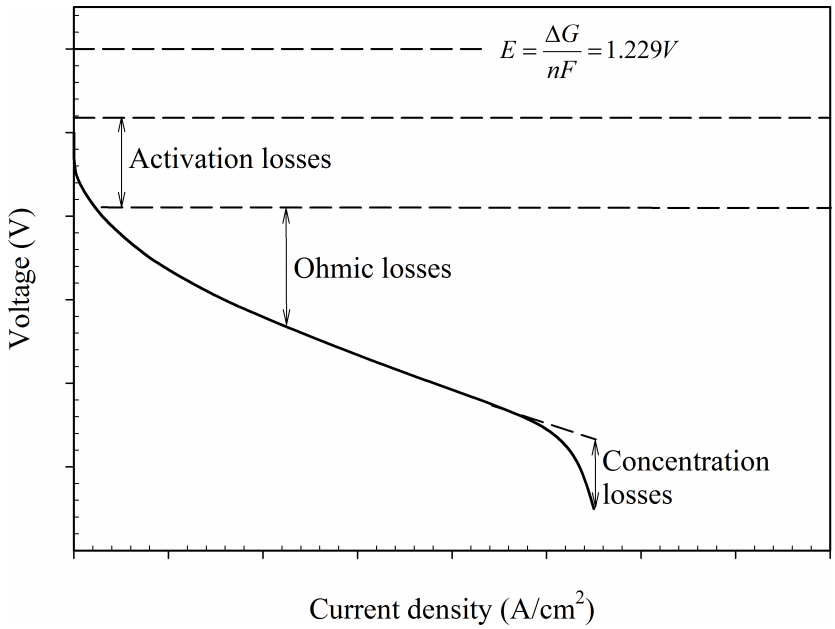

Figure 1.2: Scheme of a typical polarisation curve.

1.5 PEM Fuel Cell Performance

The fuel cell performance is commonly evaluated using the polarisation curve as an indicator; it usually presents the average current density (A/cm^2) and the cell voltage (V), in the abscissa and ordinate coordinate, respectively. Operating under the thermodynamic reversible conditions, a fuel cell is capable of producing the maximum amount of electrical potential between cathode and anode, which is called the reversible cell potential. As shown in the Figure 1.2, the increase of current causes the increase of irreversible losses, also called overpotential or polarisation [45].

According to literature [18, 55], there are three main irreversibilities: activation, Ohmic and concentration losses. The Equation (1.8) presents the relation between the cell voltage, the cell reversible voltage and the sum of the irreversibilities (cell overpotential):

$$\phi_{cell} = \phi_{rev} - (\eta_{act} + \eta_{ohm} + \eta_{conc}) = \phi_{rev} - \eta_{total} \tag{1.8}$$

The activation loss, η_{act}, arises due the energy lost from the increase of the rate of electrochemical reactions as required. The Ohmic loss, η_{ohm}, arises from

the ionic and electronic resistance to flow inside the AEM fuel cell and it presents a linear behaviour. The Ohmic loss presents a dependent behaviour on the cell current, as the increase of the current results in the increase of the Ohmic loss. The concentration loss, η_{conc}, is a consequence of the high demand of species or due to the clogged pores caused by the over accumulation of liquid water, especially under higher current density region.

1.6 Objectives

The main objectives of this thesis are:

- To identify the issues of the numerical macro-homogeneous models for AEM fuel cell currently available in literature;
- To propose an advanced three-dimensional multiphase agglomerate model for an AEM fuel cell;
- To compare the developed agglomerate model with the current available macro-homogeneous model in order to provide insights about the effect of the additional transport resistances within the CL;
- To understand the limitations of mass transport caused by water production, consumption and phase change;
- To perform a parametric analysis on the effects of different catalyst layer composition on the overall performance of the fuel cell.

The objectives proposed in this thesis will be achieved by the development of a three-dimensional (3D) multiphase macro-homogeneous model for an AEM fuel cell. The proposed macro-homogeneous model will be implemented in a computational fluid dynamics (CFD) software in order to evaluate the interrelated physico-chemical processes and operation of the various interactions. Subsequently, the macro-homogeneous model will be upgraded and an agglomerate model for AEM fuel cell will be developed. The proposed agglomerate model will take into account the subtle transportation phenomena that takes place in the CL. A comprehensive comparison between the macro-homogeneous and the agglomerate model is

presented and the behaviour of key quantities such as effectiveness, ionic and concentration losses are analysed. Finally, the developed agglomerate model will be used in an extensive parametric analysis of the effects of the catalyst layer composition (i.e. platinum loading, carbon loading and ionomer volume fraction) on the overall performance of the fuel cell. The results are discussed and optimum values for the operating condition and parameters analyses are proposed.

In this chapter, an overview of the AEM fuel cell, its applications, components and the objectives of this thesis are presented. In Chapter 2, the literature will be reviewed and the state of the art of the AEM experimental and numerical work are discussed. The mathematical formulation and numerical implementation of the developed models will be presented in Chapter 3 and Chapter 4, respectively. The numerical results from macro-homogeneous model, first and final proposed agglomerate model will be presented in Chapter 5, Chapter 6 and Chapter 7, respectively.

Chapter 2

Literature Review

Over the past decade, as one can see in Figure 2.1, the number of published studies related to AEM fuel cells has increased [3]. Even though AEM fuel cell publications have increased significantly, they represent less than 17% when compared to proton exchange membrane fuel cell publications over the same period of time. These recent studies in AEM fuel cells were essential to improve the understanding of the transport mechanisms and the role water and heat transfer play on the overall performance of the fuel cell. Several studies reported significant improvements on the solutions of the already known issues regarding AEM fuel cells.

In the recent past, several studies were published emphasising the most up to date issues remaining on AEM fuel cell [16, 21, 32, 61, 66, 84, 88]. In the most recent study, Dekel [21] has identified three of the main characteristics of high performance AEM fuel cells: a) high ionic conductivity at the membrane and CL; b) highly active CL, providing enhanced HOR; and c) an effective water management strategy. Despite all the aforementioned characteristics highlighted by Dekel [21] being relevant for the achievement of high performance AEM fuel cells, the present thesis will be focusing on the importance of the water management strategy on AEM fuel cells.

The following sections of this chapter present a literature review of the most relevant work related with experimental and numerical model in AEM fuel cell.

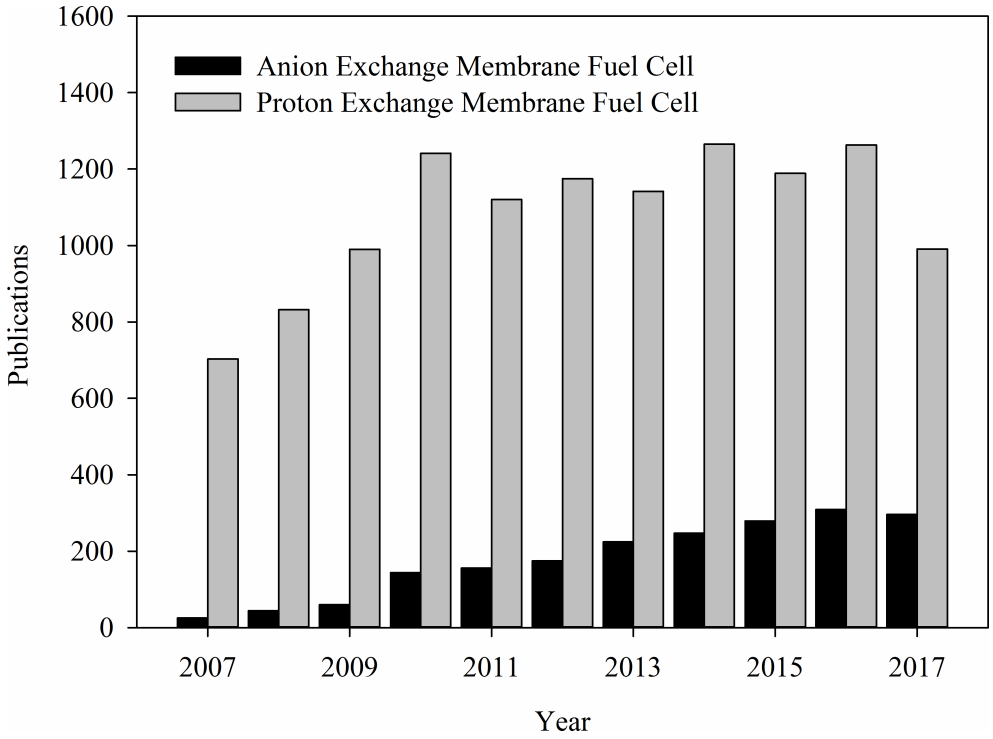

Figure 2.1: Number of publication per year about anion exchange membrane fuel cell and proton exchange membrane fuel cell (key words: anion exchange membrane fuel cell; proton exchange membrane fuel cell) [3].

2.1 Experimental Work

On the experimental field, numerous studies were performed in different frameworks, such as property and coefficient characterisation, water management and material optimisation.

The oxygen reduction kinetics and mass transportation for Tokuyama A201 membrane were analysed by Gunasekar et al. [30]. Under lower current density region, similar oxygen reduction kinetics for the OH^- ion in comparison to Nafion were reported. Nevertheless, under higher current density region, the effects of mass transportation started to play a role in the current density. The Tokuyama A201 membrane presented higher oxygen diffusion for the OH^- when compared with Nafion. This is attributed to the higher ion exchange capacity of the Tokuyama A201 membrane (i.e. 1.8 meq/g) in comparison to Nafion (i.e. 0.91 meq/g), as the higher water uptake enhances the oxygen diffusion in the

aqueous medium. In addition to Gunasekar and his collaborators efforts to characterise the mass transportation of oxygen in AEM fuel cells, Khadke and Kewer [46] quantified the mass transportation characteristics of O_2 in Tokuyama AS-4 ionomer. It was reported to display Fickian behaviour, meaning the diffusion coefficient is independent of the film thickness and concentration. In addition to that, it was also reported that the oxygen diffusion in AS-4 ionomer presents one higher order of magnitude in comparison to the Nafion ionomer.

Among the properties required for a AEM membrane, Couture et al. [16] highlighted the high ionic conductivity, to provide satisfactory barrier to the species crossing through the membrane, chemical stability, durability under different hydration condition and properties stability under the working temperature. The conductivity and thermal durability were the driving factors for the development of new membrane material by Ren et al. [73]. In their study, significant improvements in ionic conductivity (0.0984 S/cm) and membrane swelling (117 $wt\%$ at 22^oC) have been reported when compared to the Tokuyama A201. The hydrophobic network and the reduced tortuosity of the ionic conduction paths are attributed as the reason for the membrane mechanical integrity and high ionic conductivity, respectively. Different composites were used by Zhao et al. [102] to synthesize an alkaline anion exchange membranes. When tested at 30^oC, the hydroxide conductivity reached values up to 0.057 S/cm, with a maximum ion exchange capacity of 1.74 meq/g and a mechanical strength of 102.3 MPa. While operating with H_2/O_2 at 50^oC , the previous membrane reached a maximum power density of 278 mW/cm. In addition to that, durability tests were performed, and under higher temperature (60^oC), higher durability was observed, with no major changes in the ionic conductivity for 1000 h.

Xu et al. [98] has reported higher performance utilising Co_3O_4 electro catalyst layer for ORR in comparison to palladium based catalyst layer, thus reducing the cost of an AEM fuel cell. Asazawa et al. [4] has also observed higher overall performance of an direct hydrazine alkaline AEM fuel cell utilising non-precious metal such as cobalt and nickel at the anode catalyst layer in comparison to platinum.

Enhancement of the dimensional, thermal and alkaline stability of the AEM fuel cell were obtained by Ran et al. [71] by the use of graft architecture and

rational cross-linking. Ran and his collaborators have reported an AEM with ionic conductivity as high as 0.120 S/cm at 90^oC, with low dimensional swelling (6%), an ion exchange capacity (IEC) of 2.57 $mmol/g$ and water uptake of 41 %. With respect of the alkaline stability, an augmentation of the ionic conductivity was reported before reaching alkaline stability after 100 h of immersion.

The water management and the characterisation of parameters involved in such processes were analysed in literature. Li et al. [56] measured not only the water uptake, but also the water diffusivity and the electro-osmotic drag (EOD) coefficient for different temperatures in an AEM. The water uptake of the AEM in equilibrium was found to vary from 17 to 19 for 30 to 60^oC, respectively. The reason for the increment of the water uptake when temperature increases is due to the formation of hydrated ion clusters and the micro pores opening, hence leading to higher water absorption in the membrane. Li and his collaborators also observed an increase in the water uptake when the relative humidity increased. Similarly to the water uptake, the water diffusivity also improved with the increase of the water uptake and also the temperature. With respect to the EOD coefficient, the authors reported EOD coefficients for high values of water uptake, as due to the water gradient from anode and cathode of a typical AEM fuel cell, the water uptake of the membrane is generally observed to stay high.

Duan et al. [24] carried out an experimental investigation of the water uptake, ionic conductivity and dimensional change of the commercial Tokuyama A201 membrane over different values of temperature (50 and 80^oC) and water activity (0-0.95). Duan and collaborators have observed an improvement in the water uptake of the A201 membrane when temperature and water activity were increased. In addition to that, when tested under fully hydration condition, the A201 membrane presented a dimensional change of 9 and 12% for the 50 and 80^oC cases, respectively, whereas fully hydrated Nafion increases by almost 40% [33]. Current effort is still imposed to improve water and heat transfer management. Similar studies were also performed by Barath et al. [10] and, for a membrane of 100 nm thickness, water uptake was reported to be approximately 22.5.

The effect of wet proofing on hydroxide exchange membrane fuel cells performance was reported by Kaspar et al. [44]. The effects of different ionomer loadings (10-30%) in a MEA utilising a Tokuyama A901, Tokuyama AS-4 ionomer, cata-

lyst loading of 0.4 mg_{Pt}/cm^2 TKK 50% and 10% PTFE in Toray GDLs was disclosed by the authors. It was observed that the optimum performance was obtained when utilising 20% ionomer loading, as the utilisation of the CL is compromised when low ionomer volume fraction is considered (i.e. lower ionic conductivity). It has also been observed that the excess of ionomer resulted in an increase of mass loss due to pore clogging. Identical MEAs, considering a 20% ionomer loading, were produced to investigate the effect of waterproofing on the overall performance of the fuel cell. It was reported that waterproofing has significant impact on the overall performance of the fuel cell, especially when the anode GDL is water proofed in comparison to cathode GDL. The authors also suggested that the depletion of the overall performance of the fuel cell is a consequence that arises due to the mass loss as a result from the anode flooding, therefore, the cathode humidification is more appropriated to avoid depletion the overall performance of the fuel cell.

Recently, a water management strategy for a H_2/O_2 AEM fuel cell is proposed by Omasta et al [65] in order to prevent the flooding of the electrodes whilst maintaining the membrane hydrated. Experimental results have shown a diminished performance of the fuel cell when operating under anode and cathode full humidification condition. Nevertheless, when reducing the relative humidity on the anode and cathode side to 87% and 79%, respectively, optimum performance of the fuel cell was obtained. Further reduction of the relative humidity has reduced the performance of the fuel cell due to the dehydration of the MEA components.

2.2 Numerical Modelling

Several numerical models were developed on the PEM fuel cell framework. Among these studies, some of the most important research activities were carried out for PEM over the past few decades and also some up to date work on AEM fuel cell. In 1991, Springer et al. [79] presented a one dimensional, isothermal, steady state model for an entire PEM fuel cell. In their diffusion model, empirical correlations were proposed for the water diffusion coefficient, electro-osmotic drag coefficient and ionic diffusion. These correlations presented a dependence on the membrane

water content. At a fixed temperature of 30°C, experimental data was measured and resulted in an empirical correlation for the ionic diffusivity. This diffusion correlation is widely used in literature [14, 25, 76] due to its good agreement with experimental data. As another outcome of their work, Springer and collaborators [79] concluded that the increase of membrane resistance and current density are related and this resistance can be decreased by reducing membrane thickness.

Later, in 1992, Bernardi and Verbrugge [7] proposed a mathematical convective model of a gas diffusion electrode bonded to a polymer electrolyte. This model provided good agreement with experimental data and focused on polarisation curve, catalyst utilisation and water transportation. The authors [7] reported a sharp drop in current density at lower current density ($<100\ mA/cm^2$) mainly due to the activation potential. Whereas the subsequent almost linear potential drop is mainly associated with the increase of the Ohmic resistance at the membrane. Even though the authors [7] described the importance of ORR over all the practical current densities, they concluded that the CL is utilised more efficiently under lower current density, as the oxygen concentration decreases near the membrane/CL interface.

The complexities of the water transportation within the fuel cell due to electric-potential forces and pressure gradient are raised by Bernardi and Verbrugge. In the three-dimensional model proposed by Bearing et al. [8], all major transport phenomena except phase change were considered. Focusing on the better understanding and the numerical reproduction of physical phenomena involved on PEM fuel cell, important quantities such as concentration, current density, temperature and water flux were widely investigated. Their results showed a high influence of temperature on the fuel cell efficiency, presenting large gradients within the fuel cell domain. Due to the higher species concentration under the flow channel, higher current density was observed in comparison to the region under the bipolar plate. This is related with the limited transportation of the species under the collector. Nevertheless, the 3D model proposed by the authors does not take into account important characteristics of fuel cell operation such as water phase change phenomena and membrane dehydration.

Wang's [86] work provided a substantial summary of the fundamental models of different types of fuel cell, including PEM fuel cell, comprehending both single

and multi-phase models, transient phenomena and the heat, water and electrons transportation. Although the author [86] presented significant advancement in the PEM numerical modelling field, the importance of understanding of the liquid water transportation within CL and GDL is highlighted, in order to address the flooding phenomenon that limits the current density produced by a PEM fuel cell. Sun et al. [80] developed a novel two-dimensional agglomerate model for the CCL of a PEM fuel cell. In this model, instead of considering a macro-homogeneous domain, the CCL was treated as an agglomerate composed of platinum and carbon molecules covered by an ionomer layer. This approach allowed not only an improvement for the modelling of the transportation of electrons, ions and species within the catalyst layer, but also enabled the evaluation of the utilisation of the CL and the effect of the CL composition on the overall performance of the fuel cell. Sun and his collaborators [80] reported a non-uniform overpotential in the CCL, contradicting the common assumption of thin layer models regarding a uniform overpotential through the CL. Hence, the thin layer models are likely to overpredict the overall performance of the fuel cell in comparison to the agglomerate model. Another important finding was the fact that the overpotential that dictates where the highest current density is observed. Instead of the common belief that the higher current density can be found be either under the land or under the flow channel area. Moreover, with the respect of the CL utilisation, an improvement was observed with an increase of the current density, as the oxygen diffusion limits the reaction rate, especially under the land region.

Later, a three-dimensional agglomerate model was proposed by Das et al. [19] and an analysis of the activation potential and current density was provided. Among the different arrangements of agglomerate proposed by the authors [19] (in-line and two staggered), the in-line arrangement presented the lower activation overportential due to the variation of O_2 through the domain. Nevertheless, staggered arrangements present more realistic scenarios, as higher activation overpotential is observed due to the higher resistance to the oxygen transportation (i.e. lower porosity). Xing et al. [93] proposed a two-dimensional isothermal agglomerate model for a PEMFC. The novelty of the proposed model was the inclusion of different water transport mechanisms (i.e. EOD, back diffusion and hydraulic permeation) and the formation of liquid water in the void within the

agglomerate. When increasing the current density and decreasing the temperature, the liquid water formed within the void region in the agglomerate increases. Consequently, the thickness of the carbon-ionomer-liquid water film increases, resulting in an increase in the oxygen transport resistance. In addition to that, the platinum and carbon loading were varied and results were analysed. Xing et al. [93] suggest that an increase of the platinum loading is beneficial to the overall performance of the fuel cell, nevertheless, the effectiveness factor is reduced by doing so. With respect to the carbon loading, it was observed that its increment can be beneficial to the fuel cell performance, nevertheless, at lower voltages, it decreases the current density. Xing et al. [93] also suggested an optimization of the performance of the fuel cell by controlling the CL composition and operating parameters, in order to decrease the liquid water film within the void region in the agglomerate.

Later, Xing et al. [95] proposed a two-dimensional multiphase non-isothermal agglomerate model for a PEMFC. The ionomer swelling effect due to the contact with water vapour has an adverse effect on the fuel cell overall performance, as the coating thickness increased (i.e increase of transportation resistance) and reduced the porosity of the CL. In respect of the operating temperature, increasing it has a positive impact on the fuel cell performance due to the reduced saturation of water in the pores and also the increase of the membrane water content. Despite the previous benefits from increasing temperature, the performance of the fuel cell can be adversely affected under high temperature (e.g. $T = 80^oC$) and fully humidified condition, as the water mole fraction at the inlet increases to 0.48 (from 0.2 at 60^oC), affecting the oxygen supply to the CCL. With respect of the temperature distribution, the CCL usually shows higher average temperature in comparison with other components of the fuel cell, thus suggesting that supplying a high temperature fluid at the anode side is beneficial to the temperature distribution of the components. Even though the aforementioned studies were related to PEMFCs, they were able to provide a deep insight of the interrelated physics of heat, mass and momentum transport present in a fuel cell and also can be used as a good platform for the development of an AEM fuel cell numerical model.

In the AEM fuel cell framework, recently progress has been done by several

groups. An investigation of the water transportation in a three-dimensional numerical model of an alkaline AEM fuel cell anode was proposed by Huo et al. [36]. The authors [36] have observed that the liquid water at the anode CL and GDL is significantly influenced by the current density and the local temperature. On the other hand, the stoichiometry ratio has been proved to have an insignificant influence on the liquid water transportation. The authors [36] also concluded that the current density and the temperature are the parameters which have most influence on the liquid water distribution in anode side.

Hao et al. [23] carried out an analysis focusing on a transient AEM fuel cell. The effect of current density, anode and cathode inlet relative humidity, stoichiometric ratio and operating temperature were analysed at different time instants. It was reported that, when the time step increases, reducing the current density increases the time necessary to achieve a steady state condition. Similar behaviour was also observed when the temperature decreases. Nevertheless, when the time step increases and the current density decreases, it takes longer to reach the steady state regime. This behaviour is attributed to the equilibrium between gaseous water at the anode and cathode, as it takes longer to remove the liquid water from the anode side until an equilibrium condition is achieved.

Jiao et al. [42] proposed a multi-phase three-dimensional model for an AEM fuel cell. Their results have shown that a high humidification at the anode side has no significant influence on the overall fuel cell performance. Nevertheless, low humidification has a significant impact as dehydration of the membrane is observed, thus increasing the Ohmic resistance. Results indicated that the anode liquid water removal mechanism is dependent on the humidification at the anode flow channel, and the water is removed as vapour when partially humidified and removed as liquid water when full humidified mixture is supplied. The humidification on the cathode side plays an important role when operating under high current density due to the diffusion of liquid water from the flow channel to the GDL. When evaluating the thickness of the membrane on the overall performance of the fuel cell, results have shown that a thinner membrane leads to a performance enhancement due to a quicker water back-diffusion from anode to cathode.

Using an isothermal one-dimensional numerical model, Sohn et al. [78] ana-

lysed the water transportation in an AEM fuel cell. The authors [78] reported the water fluxes within the domain. It was observed that, when operating at 100% relative humidity at both anode and cathode inlets, the back-diffusion transportation was dominant over the EOD, resulting in a water flux from the anode towards the cathode. Nevertheless, when operating under dry anode and 100% relative humidity at cathode inlet, the water was transported from the cathode to the anode. The results obtained by Sohn et al. [78] are in accordance to the experimental study carried out by Isomura et al. [39]. Kui et al. [43] proposed an analytical model for an AEM fuel cell. Results showed a depletion of water at the CCL when operating under lower relative humidity, mainly associated to the electrochemical reaction and the EOD. Thus, an improvement on the current density produced was observed when the mixture supplied at the cathode inlet had its relative humidity increased. On the other hand, the overall performance was improved when no liquid water was supplied at the cathode side and the oxygen stoichiometry ratio was kept constant. This is associated to the increase of activation and Ohmic losses due to the higher operating pressure.

The effect of the CL thickness was also studied by Kui et al. [43]. When increasing the CL thickness, an increase of Ohmic loss and a decrease of species concentration was observed. Kui et al. [43] also reported that decreasing the membrane thickness resulted in a lower activation losses and Ohmic resistance, as the water transportation through the membrane is enhanced. A three-dimensional multi-phase numerical model for a representative AEM fuel cell was proposed by Machado et al. [59] in order to analyse the influence of flow direction, temperature and relative humidity on the overall performance of the fuel cell. Results showed that flow direction had no influence on the overall performance of the fuel cell. Nevertheless, a substantial impact on the overall performance was reported when varying the operating temperature and the relative humidity at the FC inlet. In addition to the facilitated ionic diffusion, the rise of the operating temperature also resulted in the enhancement of the electrochemical kinetics, thus improving the overall performance under higher operating temperature condition. The reduction of overall performance obtained for lower relative humidity cases in comparison to fully hydrated cases is mainly associated with the deterioration of the membrane hydration led by the reduction of water transported from

anode to cathode due to back-diffusion.

Recently, the effects of relative humidity, ionomer loading and IEC on the fuel cell overall performance were analysed by Dekel et al. [22] with their transient one-dimensional numerical model. In agreement with previous results, the relative humidity has been observed to be crucial to the optimisation of the overall performance of the fuel cell, having higher impact under higher current density (>1.0 A/cm^2). Whilst no significant impact is observed at the anode side, the cathode side hydration is drastically affected by the cathode relative humidity inlet condition, thus having direct impact on the Ohmic loss at the CCL. With respect to the ionomer loading, the authors observed that higher ionomer loading (i.e. ionomer wt 25 %) resulted in the pore clogging and the reduction of the electrons conductivity. On the other hand, excessively reducing the ionomer loading (i.e. ionomer wt 10 %) led to higher ionic resistance, and consequently, the detriment of the overall performance of the fuel cell. In addition to aforementioned results, Dekel et al. [22] reported that the IEC has no major effect on the hydration level of the ACL. Nevertheless, the hydration level at the CCL is affected by the IEC, thus resulting in the reduction of the Ohmic resistance at the CCL. Furthermore, Dekel et al. [22] also reported the higher utilisation of the ACL closer to the membrane interface, even though no change was observed for the production rate of OH^-, suggesting the benefits of a thinner CL at the anode side. On the other hand, the rate of production of OH^- at the cathode side shows a relatively homogeneous profile through the CL thickness for low current density (e.g. 0.5 A/cm^2) and significantly higher utilisation of the CL close to the membrane was observed when operating under higher current density (i.e. 2.0 A/cm^2). Therefore, Dekel et al. [22] have suggested the use of thinner and thicker CL for higher and lower current density, respectively.

Despite the significant improvement in the modelling of AEM fuel cells, the numerical models discussed in this section considered a macro-homogeneous approach, which neglects many of the losses and also does not take into consideration many of the subtle transport mechanisms taking place in the CL. As per the catalyst layer composition, the common approach of bulk properties does not allow the variation of parameters such as carbon and platinum loading, thus limiting the evaluation of important quantities such as activation potential and utilisa-

tion of the catalyst layer. In addition to that, the use of assumed physical and structural parameters of the CL (e.g. CL thickness, ionomer thickness, porosity, etc.) in the macro-homogeneous model can possible result in an overprediction of the overall performance of the fuel cell.

2.3 Summary

In this chapter, the existing literature was reviewed focusing on the different aspects of the main issues of AEM fuel cells. The most relevant and recent studies were summarised for experimental investigation and numerical modelling of AEM fuel cells. From one-dimensional to sophisticated three-dimensional numerical models, several models have been developed to not only provide better understanding of the transport phenomena inside the PEM fuel cell, but also a more realistic reproduction of phenomena such as phase change, back diffusion and electro-osmotic drag. Although substantial progress has been done over the past few years with respect of numerical modelling, there are still issues regarding the transport of ions and reactants within the CL. Therefore, further investigation must be carried out in order to provide a better understanding of the resistances imposed by the CL composition and physical characteristics to the diffusion of species and ions within the CL in an AEM fuel cell.

Experimental results have shown that water management is essential in order to maximise the power output of an AEM fuel cell. Therefore, an in-depth numerical analysis of these critical issues is necessary to elucidate the effects of water transportation, production and phase change on interrelated phenomena and the overall performance of the fuel cell.

In this thesis, an agglomerate model is developed in order to simulate with less restrictive assumptions the physico-chemical phenomena present in the CL of an AEM fuel cell.

Chapter 3

Model Formulation

As previously presented in Chapter 2, over the course of the past decade, in order to mathematically describe an AEM fuel cell, several macro-homogeneous models were developed. Nevertheless, the need for more accurate and realistic models has driven researchers to develop a more detailed model, capable of capturing the subtle transport phenomena usually neglected in the conventional macro-homogeneous models. Table 3.1 presents the main differences between interface, macro-homogeneous and agglomerate model as listed by Huang et al. [35]. As one can see from Figure 3.1, the agglomerate model has evolved from the macro-homogeneous model, and instead of a single macro length scale (catalyst layer thickness), a micro length scale (agglomerate scale) is also considered. Therefore, in the agglomerate scale, the subtle transportation phenomena such as mass and ion diffusion through the ionomer layer covering the platinum dispersed carbon are taken into account. Further details of the transport phenomena with respect to the agglomerate scale is presented later in this chapter.

In this chapter, the conservation equations for mass, momentum, membrane water content, liquid water, electronic and ionic charge and energy are presented for both macro-homogeneous and agglomerate models. Also, further discussion regarding the differences between macro-homogeneous and agglomerate models with respect to transportation phenomena are discussed. Later, the boundary conditions and the configuration used in this research are presented. Finally, this chapter is concluded with a summary of the governing equations for both macro-homogeneous and agglomerate numerical models.

Table 3.1: Summary of different models for the catalyst layer [35].

Interface model	Macro-homogeneous model	Agglomerate model
Zero dimensional	One length scale (i.e CL thickness)	Two length scales (i.e. CL and ionomer thickness)
Single equation as boundary condition for GDL and PEM	Porous electrode theory to describe distribution	Agglomerate as a representative element
Quick and simple	Effective properties averaging over a representative volume element	Agglomerates embedded into macro-homogeneous model
Limited use in fuel cell models	Applicable for homogeneous catalyst layer	Mainstream model

3.1 Assumptions

For the purpose of computational economy, a number of assumptions have been made in the analysis undertaken in this thesis. The assumptions, however, do not compromise the physical characteristics of the AEM fuel cell. The list of assumptions made in this thesis are:

- Body forces were neglected (e.g. gravity);
- steady-state regime is considered;
- Ideal gas law is considered for the gaseous phase;
- The flow in the channel is assumed to be laminar, as the Reynolds number in a typical case was found to be of the order of 100;
- The gas fed into the flow channel is pure, therefore no contamination is considered;

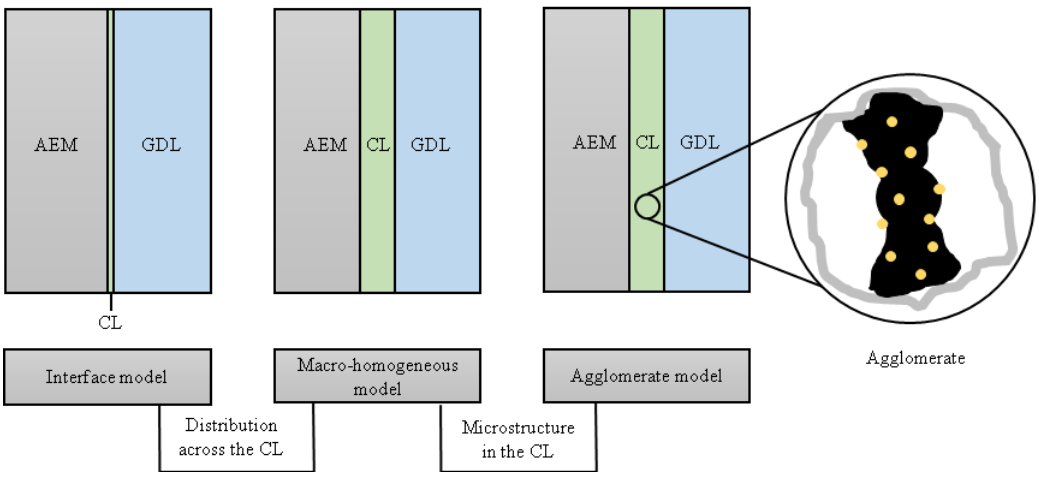

Figure 3.1: Two-dimensional scheme for the different types of catalyst layer model (adapted from [35]). The grey area in the agglomerate representation stands for the ionomer. The white area represents the porous within the agglomerate and the black and yellow regions represent the carbon and platinum, respectively.

- Membrane is considered impermeable to all the species but water in the dissolved phase;
- Due to the many complexities involving the consideration of liquid water in the flow channel, such as droplet adhesion on the walls and the fluid/particle interaction, in addition to a rapid increase of computational demand for such an analysis, it is assumed that there is no water in the liquid phase in the flow channel.

The specific assumptions of each transport equation are presented as convenient.

3.2 Transport of Gas Species

3.2.1 Conservation of Mass and Momentum

3.2.1.1 Macro-homogeneous model

Typically, humidified gas is supplied at the flow channel inlet of an AEM fuel cell. Different mixtures such as H_2/O_2 or H_2/Air are supplied at the anode and cathode inlets, respectively. Therefore, the conservation of mass and momentum

of species must be satisfied. Equations (3.1) and (3.2) describe the conservation of mass and momentum, respectively, for gases and are defined as

$$\frac{\partial}{\partial t}\left(\epsilon^{eff}\rho_g\right) + \nabla\cdot\left(\rho_g\vec{u}_g\right) = S_{mass} \tag{3.1}$$

$$\frac{\partial}{\partial t}\left(\frac{1}{\epsilon^{eff}}\rho_g\vec{u}_g\right) + \nabla\cdot\left(\frac{1}{(\epsilon^{eff})^2}\rho_g\vec{u}_g\vec{u}_g\right) = -\nabla P_g + \nabla\cdot\left(\bar{\bar{\tau}}\right) + \rho\vec{g} - \frac{k_g\vec{u}_g}{\mu_g} \tag{3.2}$$

where ρ, $\vec{u}_g$, P_g represent the density, the velocity vector and the pressure of the gas phase, respectively; K_0 is the intrinsic permeability of the medium; k_g is the permeability of the gas in the porous medium corrected by the fraction of liquid water, s, present at the porous as it follows

$$k_g = K_0\,(1-s)^n \tag{3.3}$$

and S_{mass} represents the source terms of mass and further explanation regarding this term is presented later in this chapter. Here, ϵ^{eff} stands for the effective porosity for gas transport, defined as a function of the bulk porosity, ϵ, and the liquid water fraction in the pore as shown in the Equation (3.4)

$$\epsilon^{eff} = \epsilon(1-s) \tag{3.4}$$

In addition to the gas velocity, the stress tensor, $\bar{\bar{\tau}}$, is also dependent on the dynamic viscosity (μ) and the unit tensor (I). The stress tensor is defined as

$$\bar{\bar{\tau}} = \mu_g\left[\left(\nabla\vec{u}_g + \nabla\vec{u}_g^T\right) - \frac{2}{3}\nabla\cdot\vec{u}_g I\right] \tag{3.5}$$

As previously mentioned in the assumptions section of this chapter, a steady-state is assumed, so the first term on the left hand side (LHS) of Equations ((3.1)-(3.2)) vanishes. In addition to that, the body force is also assumed to be negligible, therefore, the conservation equations of mass and species can be written, respectively, as follows:

$$\nabla\cdot\left(\rho_g\vec{u}_g\right) = S_{mass} \tag{3.6}$$

$$\nabla \cdot \left(\frac{1}{(\epsilon^{eff})^2} \rho_g \vec{u}_g \vec{u}_g \right) = -\nabla P_g + \nabla \cdot \left(\bar{\bar{\tau}} \right) - \frac{k_g \vec{u}_g}{\mu_g} \tag{3.7}$$

In order to represent the transport of different species in the macro-homogeneous model, the convective-diffusive equation is used as follows:

$$\frac{\partial}{\partial t} \left(\epsilon^{eff} C_i \right) + \nabla \cdot \left(-D_{i,m}^{eff} \nabla C_i \right) + \nabla \cdot \left(\vec{u}_g C_i \right) = S_i \tag{3.8}$$

where the molar concentration and the production/consumption of the ith species are represented by C_i and S_i, respectively, and D_i^{eff} is the effective species diffusivity for the ith species.

Once again, due to the steady-state assumption, the first term on the LHS of Equation (3.8) vanishes. Hence, the convective-diffusive equation becomes

$$\nabla \cdot \left(-D_i^{eff} \nabla C_i \right) + \nabla \cdot \left(\vec{u}_g C_i \right) = S_i \tag{3.9}$$

Since no contaminants are considered in the gas flow, the number of species is considered to be four, and these are hydrogen, oxygen, water vapour and nitrogen. The species molar fraction, X_i, whose sum must be equal to 1, is the link between the previous equations for the gas transport, and it is defined as

$$\sum_{i=1}^{N} X_i = 1 \tag{3.10}$$

where N is the number of species. The species molar fraction is evaluated as

$$X_i = \frac{C_i}{\sum\limits_{i=1}^{N} C_i} \tag{3.11}$$

The relation between the gas transport equation and the continuity equation can be correlated using the two following relations

$$\rho_g = \sum_{i=1}^{N} M_i C_i \tag{3.12}$$

$$S_{mass} = \sum_{i=1}^{N} S_i \tag{3.13}$$

where M_i stands for the molecular weight of the ith species.

The mass fraction, Y_i, stands for the mass of one component divided by the total mass of the mixture, as presented in the following equation:

$$Y_i = \frac{M_i C_i}{\sum_{i=1}^{N} M_i C_i} \tag{3.14}$$

Rearranging the Equations (3.9, 3.12 and 3.14), we obtain the gas species conservation equation in terms of mass fraction

$$\nabla \cdot \left(-\rho_g D_i^{eff} \nabla Y_i\right) + \nabla \cdot (\rho_g \vec{u_g} Y_i) = S_i \tag{3.15}$$

According to Reid et al. [72], the diffusion of mass is ruled by the gradient of temperature, concentration and pressure. Once pressure and temperature gradients are irrelevant when compared with the concentration gradient, both of them are neglected. Thus, the diffusion coefficient in the transport equation can be approximated by Fick's law. The effective diffusivity is obtained by using a Bruggemann correction [13] and also by the porosity and the liquid water fraction as follows

$$D_{i,m}^{eff} = D_i \epsilon^n (1-s)^n \tag{3.16}$$

where D_i is the mass diffusivity of the ith species. The mass diffusivity of different the ith species are defined as [42]

$$D_{H_2}^a = 1.055E-4 \left(\frac{T}{T_{ref}}\right)^{1.5} \left(\frac{P_{ref}}{P}\right) \tag{3.17}$$

$$D_{H_2O}^a = 1.055E-4 \left(\frac{T}{T_{ref}}\right)^{1.5} \left(\frac{P_{ref}}{P}\right) \tag{3.18}$$

$$D_{O_2}^c = 2.652E-4 \left(\frac{T}{T_{ref}}\right)^{1.5} \left(\frac{P_{ref}}{P}\right) \tag{3.19}$$

$$D_v^c = 2.982E-5 \left(\frac{T}{T_{ref}}\right)^{1.5} \left(\frac{P_{ref}}{P}\right) \tag{3.20}$$

where T and P represent temperature and pressure respectively; T_{ref} (=293.15 K)

and P_{ref} (=101325 Pa) represent reference temperature and reference pressure respectively; the superscripts a and c stand for the anode and cathode side, respectively.

3.2.1.2 Agglomerate model

In the proposed agglomerate model, a three-dimensional spherical agglomerate model is used in discretise domain of the catalyst layer. Therefore, the volume fractions of evenly distributed spheres composed of platinum dispersed carbon ($L_{Pt/C}$), ionomer (L_M), and the pores (ϵ_{CL}) are considered to describe the catalyst layer domain. A two-dimensional schematic representation of one such sphere is presented in Fig 3.2, where the platinum dispersed carbon of radius r_{agg} is covered by a layer of ionomer of δ_M thickness. As the reactants have to diffuse through the ionomer layer in order to reach the Pt/C sites, the concentration of the ith species is defined at the gas and ionomer interface and at the ionomer and particle interface, $C_{i,g/M}$ and $C_{i,M/s}$, respectively. Thus, the catalyst layer composition can be expressed in terms of the volume fraction as

$$L_{Pt/C} + L_M + \epsilon_{CL} = 1 \tag{3.21}$$

The volume fraction of Pt/C in the catalyst layer is given by [18, 20]

$$L_{Pt/C} = \left(\frac{m_{Pt}}{\rho_{Pt}} + \frac{m_C}{\rho_C}\right)\frac{1}{\delta_{CL}} = \left(\frac{1}{\rho_{Pt}} + \frac{1-f}{f\rho_C}\right)\frac{m_{Pt}}{\delta_{CL}} \tag{3.22}$$

$$f = \frac{m_{Pt}}{m_{Pt} + m_C} \tag{3.23}$$

where m_{Pt} and m_C are the mass of Pt and C per unit of geometric area, respectively; f stands for the platinum ratio.

In an intermediate step in the development of the latest version of the agglomerate model, the thickness of the ionomer was considered to be a fixed value from Sun et al. [80]. Hence, the results presented in Chapter 6 considered the ionomer thickness, δ_M, to have dimensions of 8×10^{-8} m. In a more sophisticated approach, the thickness of the ionomer covering the platinum dispersed carbon is calculated and it is assumed to evenly covers the agglomerate. Therefore, the

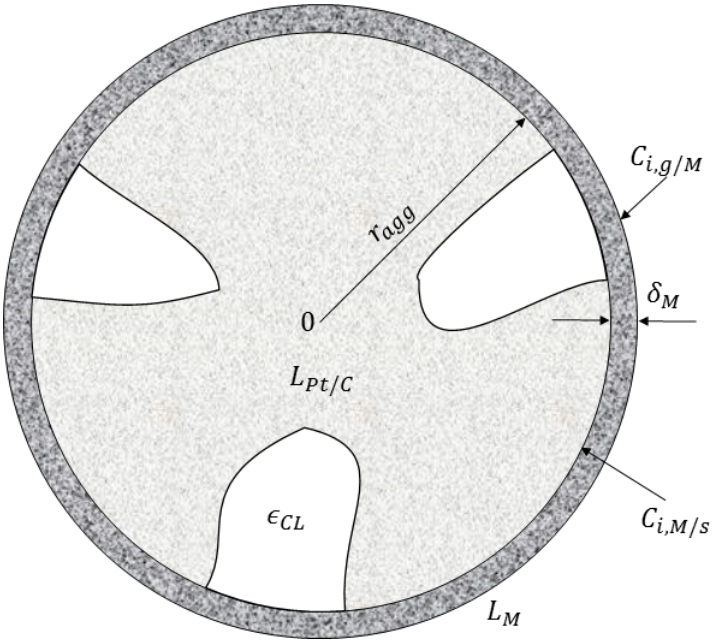

Figure 3.2: Schematic representation of the catalyst layer composition. The platinum dispersed carbon ($L_{Pt/C}$) of radius r_{agg} is covered by a layer of ionomer of thickness δ_M.

latest proposed model calculates the ionomer thickness as [95]:

$$\delta_M = r_{agg}\left(\sqrt[3]{\frac{(1-\epsilon_{CL})^2 + L_{Pt/C}\epsilon_{CL}\,(1-L_M)}{L_{Pt/C}}} - 1\right) \tag{3.24}$$

Here, instead of defining the catalyst layer with respect to the geometrical area, an effective specific area per unit catalyst layer volume is used. Thus, the effective specific platinum surface area per unit catalyst layer volume is defined as:

$$a^{eff}_{Pt,CL} = \frac{3 m_{Pt} L_{Pt/C}}{r_{Pt}\rho_{Pt}\delta_{CL}} \tag{3.25}$$

where the subscript CL corresponds to either anode (a) or cathode (c) side.

Nevertheless, further modification in the previous equations was necessary as the reaction rate occurs at the electrode-electrolyte interface [55]. Hence, the effective specific platinum surface area per unit catalyst layer volume used in

Chapter 7 is defined as

$$a_{Pt,CL}^{eff} = \frac{3m_{Pt}}{r_{Pt}\rho_{Pt}\delta_{CL}L_{Pt/C}} \tag{3.26}$$

Due to the proposed discrete domain in the CL and the inclusion of a new characteristic length (i.e. ionomer thickness), the use of bulk properties is no longer pertinent to characterise the fluid properties. Therefore, as one of the proposals of the agglomerate model, instead of the use of properties averaged over a volume (i.e. mass diffusivity), a more accurate way to account for species diffusion is considered. Some of the fluid properties such as the viscosity, thermal conductivity and the mass diffusion coefficients are computed using the kinetic theory for gases. Thus, instead of considering the diffusive term presented in Equation (3.9), the Maxwell-Stefan equation is used to describe the species diffusion phenomenon and it is presented as [26]:

$$\sum_{\substack{j=1 \\ j\neq i}}^{N} \frac{Y_i Y_j}{D_{ij}} \left(\frac{\vec{J}_j}{\rho_j} - \frac{\vec{J}_i}{\rho_i} \right) = \nabla Y_i \tag{3.27}$$

where D_{ij} is the binary mass diffusion coefficient; The diffusive mass flux vector, $\vec{J}_i$, is defined as [17]:

$$\vec{J}_i = -\sum_{j=1}^{N} \rho_i D_{ij} \nabla X_j \tag{3.28}$$

Hence, the convective-diffusive equation for species in the agglomerate model is expressed as [96]:

$$\nabla \cdot \left(-\rho_g D_{ij} \sum_{\substack{j=1 \\ j\neq i}}^{N} \frac{Y_i Y_j}{D_{ij}} \left(\frac{\vec{J}_j}{\rho_j} - \frac{\vec{J}_i}{\rho_i} \right) \right) + \nabla \cdot (\rho_g \vec{u_g} Y_i) = S_i \tag{3.29}$$

The Chapman-Enskog equation [11] is used to compute the diffusion coefficient using the kinetic theory as follows [11]:

$$D_{ij} = 1.8583 \times 10^{-7} \frac{\left[T^3 \left(\frac{1}{M_i} + \frac{1}{M_j} \right) \right]^{1/2}}{p_{abs} \sigma_{ij}^2 \Omega_D} \tag{3.30}$$

where σ_{ij}, p_{abs} and Ω_D are the arithmetic average of the individual molecular radii

Table 3.2: Lennard-Jones potential parameters [11].

Species i	$M_i(kg/kmol)$	$\sigma_i(\mathring{A})$	$(\epsilon/k_B)_i\ (K)$
H_2	2.016	2.915	38.0
O_2	32.000	3.433	113.0
H_2O	18.000	2.641	809.1
N_2	28.013	3.667	99.8

σ, the absolute pressure and the diffusion collision integral, respectively. The Lennard-Jones potential parameters necessary to compute the aforementioned variables are presented in Table 3.2 [11]. The empirical equation proposed by Neufeld et al. [63] to compute the diffusion collision integrals for the Lennard-Jones potential is written as:

$$\Omega_D = \frac{1.06036}{(T^*)^{0.15610}} + \frac{0.19300}{\exp(0.47635T^*)} + \frac{1.03587}{\exp(1.52996T^*)} + \frac{1.76474}{\exp(3.89411T^*)} \tag{3.31}$$

The equations to compute σ_{ij} and T^* are expressed, respectively, as [11]:

$$\sigma_{ij} = \frac{(\sigma_i + \sigma_j)}{2} \tag{3.32}$$

$$T^* = \frac{T}{(\epsilon/k_B)_{ij}} \tag{3.33}$$

where k_B is the Boltzmann constant. The Lennard-Jones energy parameter for the binary mixture, $(\epsilon/k_B)_{ij}$, is computed as the geometric average of the individual (ϵ/k_B), and it is expressed as [11]:

$$(\epsilon/k_B)_{ij} = \sqrt{(\epsilon/k_B)_i\,(\epsilon/k_B)_j} \tag{3.34}$$

The dynamic viscosity of the ith species, μ_i, is computed as function of the Lennard-Jones parameters and it is expressed as [11]

$$\mu_i = 2.67 \times 10^{-6} \frac{\sqrt{M_i T}}{\sigma_i^2 \Omega_i} \tag{3.35}$$

where Ω_i is empirically described by Neufeld et al. [63] as

$$\Omega_i = \frac{1.16145}{(T^*)^{0.14874}} + \frac{0.52487}{\exp(0.77320T^*)} + \frac{2.16178}{\exp(2.43787T^*)} \tag{3.36}$$

Even though the Equations (3.15) and (3.27) are sufficient to describe the transportation of species in the void region, there is another important transport phenomenon that has to be taken into account in the agglomerate model - the diffusion of species through the ionomer layer. This transportation has a potential impact on the concentration loss of the fuel cell, as the species diffusion through the ionomer is significantly slower in comparison to the species diffusion in the void region. Nevertheless, the measurements of hydrogen and oxygen diffusion coefficients for the commercial Tokuyama A201 membrane are still an unexplored area in the literature. Therefore, the hydrogen and oxygen diffusion coefficients for Nafion™ measured by Bernardi et al. [7] and Parthasarathy et al. [67], respectively, are used in this study. Thus, hydrogen and oxygen diffusivities are expressed as [80]:

$$D_{H_2-M} = 4.1 \times 10^{-7} \exp\left(-\frac{2602.0}{T}\right) \tag{3.37}$$

$$D_{O_2-M} = 4.38 \times 10^{-6} \exp\left(-\frac{25000.0}{\mathcal{R}T}\right) \tag{3.38}$$

3.2.2 Reaction Kinetics

The electrical energy extracted from the fuel cell is consequence of the electrochemical reaction taking place within the catalyst layer. As shown in Equations (1.4) and (1.5), the electrochemical reaction consists of the consumption of H_2, O_2 and H_2O, and consequently, the products of the reaction are H_2O, heat and electrical energy. Hence, the consumption and generation of species has to be taken into account in the species conservation equation (Equation (3.8)). In this thesis, it is assumed that, due to the operational conditions, there will be no phase change of any species except for water. In addition to that, it also assumed that no intermediate step in the electrochemical reaction occurs. A generalised

representation of the electrochemical reaction [55] is:

$$\sum_{i=1}^{N} v_i^{'} M_i \underset{k_b}{\overset{k_f}{\rightleftharpoons}} \sum_{i=1}^{N} v_i^{''} M_i \tag{3.39}$$

where M_i is the chemical formula for species i; $v_i^{'}$ and $v_i^{"}$ are the number of mole of the ith species for the reactant and product, respectively; N stands for the number of species reacting; k_f and k_b are the reaction rate constant for the forward and backward reaction, respectively. Considering the rate of reaction for the ith species, $\omega_i^{''}$, as [55]

$$\omega_i^{''} = \left(v_i^{''} - v_i^{'}\right) k \prod_{i=1}^{N} \left[M_i\right]^{v_i^{'}} \tag{3.40}$$

where k is the reaction rate constant. Now rearranging Equations (3.39) and (3.40) and replacing k by both forward and backward reaction rate constants, the net rate of reaction for the ith species can be defined as [55]:

$$\omega_i^{''} = \left(\omega_{i,f}^{''} + \omega_{i,b}^{''}\right) = \left(v_i^{''} - v_i^{'}\right) \left[k_f \prod_{i=1}^{N} \left[C_i\right]^{v_i^{'}} - k_b \prod_{i=1}^{N} \left[C_i\right]^{v_i^{''}}\right] \tag{3.41}$$

Due to the advantages of expressing the rate of reaction in current generated, Faraday's law is used to express the current generated over area unit, otherwise known as current density, as

$$J = J_f - J_b = -n\mathcal{F}\omega_i^{''} = k_f C_R - k_b C_P \tag{3.42}$$

where J_b and J_f are the current density for backward and forward reactions, respectively; n is the number of the mole electrons transferred per mole of fuel consumed; $\mathcal{F}$ is the Faraday constant; C_R and C_P are the concentration of reactant and product in the reaction, respectively. By the transition state theory, and considering a reversible condition, the reaction rate constant can be written as

$$k_f = B_f T \exp\left(\frac{\Delta g_f}{\mathcal{R}T}\right) \tag{3.43}$$

$$k_b = B_b T \exp\left(\frac{\Delta g_b}{\mathcal{R}T}\right) \tag{3.44}$$

where B's represent the pre-exponential factor, Δg_f and Δg_b are the molar Gibbs function of activation for oxidation (or ionisation) and activation for the reduction reaction (or discharge of ions), respectively; $\mathcal{R}$ is the universal gas constant. From its definition, the Gibbs function, Δg, corresponds to a potential difference. Thus, the Gibbs function of activation for forward and backward reactions can be expressed as [55]:

$$\Delta g_f = \Delta g_{f,r} - \alpha n \mathcal{F} \eta \tag{3.45}$$

$$\Delta g_b = \Delta g_{b,r} - (1-\alpha)\, n \mathcal{F} \eta \tag{3.46}$$

where α is the transfer coefficient (or symmetry factor) and has its value between 0 and 1; η is the overpotential, which represents the difference between electrode potential, ϕ, and the equilibrium value, ϕ_r, and can be written as

$$\eta = \phi - \phi_r \tag{3.47}$$

Substituting Equations (3.43-3.46) into Equation (3.42), the net current density, also known as Butler-Volmer equation, is obtained as follows [55, 80]:

$$J = J_f - J_b = J_0 \left\{ \exp\left(\frac{\alpha n \mathcal{F} \eta}{\mathcal{R} T}\right) - \exp\left(-\frac{(1-\alpha n)\, \mathcal{F} \eta}{\mathcal{R} T}\right) \right\} \tag{3.48}$$

where J_0 is the exchange current density and it is defined as:

$$J_0 = B_f C_R T \exp\left(\frac{-\Delta g_{f,r}}{\mathcal{R} T}\right) = B_b C_P T \exp\left(\frac{-\Delta g_{b,r}}{\mathcal{R} T}\right) \tag{3.49}$$

The exchange current density is a representation of how susceptible the reaction is to happen and it also measures, at the equilibrium electrode potential, the amount of electron transfer activity. Due to the dependence of the exchange current density on the reactants, the Equation (3.49) can be rewritten as:

$$J_0 = j_0^{ref} \left(\frac{C_R}{C_R^{ref}}\right)^{\varphi} \tag{3.50}$$

where φ is the reaction order with respect to the reactant R; j_0 is the exchange

current density at reference. The reactive surface area, A_v, defined as

$$A_v = \frac{Actual\ reactive\ surface\ area}{Volume\ of\ electrode} \tag{3.51}$$

combined with Equations (3.48) and (3.50) then results in the volumetric current density, R_i, in the following manner:

$$R_i = A_v J = A_v j_0^{ref} \left(\frac{C_R}{C_R^{ref}}\right)^{\varphi} \left\{\exp\left(\frac{\alpha n \mathcal{F}\eta}{\mathcal{R}T}\right) - \exp\left(\frac{(1-\alpha n)\,\mathcal{F}\eta}{\mathcal{R}T}\right)\right\} \tag{3.52}$$

3.2.2.1 Macro-homogeneous model

Hence, the volumetric reaction rate in the anode and cathode catalyst layer can be written, respectively, as [59]:

$$R_a = (1-s)\, A_v j_{0,a}^{ref} \left(\frac{C_{H_2}}{C_{H_2}^{ref}}\right)^{\varphi} \left\{\exp\left(\frac{(\alpha n)_a\, \mathcal{F}\eta}{\mathcal{R}T}\right) - \exp\left(-\frac{(1-(\alpha n)_a)\,\mathcal{F}\eta}{\mathcal{R}T}\right)\right\} \tag{3.53}$$

$$R_c = A_v j_{0,c}^{ref} \left(\frac{C_{O_2}}{C_{O_2}^{ref}}\right)^{\varphi} \left\{\exp\left(\frac{(\alpha n)_c\, \mathcal{F}\eta}{\mathcal{R}T}\right) - \exp\left(-\frac{(1-(\alpha n)_c)\,\mathcal{F}\eta}{\mathcal{R}T}\right)\right\} \tag{3.54}$$

where $(1-s)$ is used to subtract the parcel of the volume occupied by liquid water, as no reaction occurs in the liquid water phase. With respect of the overpotential presented in Equation 3.47, the approach used by Wu [91] is applied, thus the overpotential is calculated as follow

$$\eta = \phi_S - \phi_m \tag{3.55}$$

where ϕ_S and ϕ_m are the electronic and ionic potential.

The reaction rate of the species i can be determined by

$$S_i = \frac{v_i R_i}{n\mathcal{F}}, \tag{3.56}$$

where n is the number of electrons participating in the half-cell reaction and v_i

is the stoichiometric coefficient for the species involved in the reaction. From Equations (1.4- 1.6) we can obtain $n = 2$ for both half-cell anode and cathode side reaction. The stoichiometric coefficient for hydrogen and oxygen are $v_{H_2} = 1$ and $v_{O_2} = 1/2$, respectively. Hence, the reaction rate for hydrogen and oxygen can be expressed, in terms of mass sink, as:

$$S_{H_2} = -\frac{R_a M_{H_2}}{2\mathcal{F}} \tag{3.57}$$

$$S_{O_2} = -\frac{R_c M_{O_2}}{4\mathcal{F}} \tag{3.58}$$

In the macro-homogeneous model the water produced by the electrochemical reaction is assumed to be in the liquid phase, further discussion of the respective source term is presented later in this chapter. It is important to note that once the electrochemical reaction only takes place in the catalyst layer, no sink or source term is necessary in the other domains, and it is stated as follows:

$$S_i = 0.0 \tag{3.59}$$

With respect to the species consumption related to the electrochemical reaction, a summary of the source terms for the species and mass conservation equations for the macro-homogeneous model is presented in Table 3.3

3.2.2.2 Agglomerate model

The volumetric current density for the agglomerate model was originally proposed by Sun et al. [80] and it takes into account the effects of the different catalyst layer volume fractions and the transportation resistance due to the ionomer film covering the agglomerate particles. A more sophisticated model has been developed by Xing et al. [93] and it is used in this study to describe the current density on the anode and cathode sides, respectively, as:

$$R_a = 2\mathcal{F}\left(\frac{p_{H_2}}{H_{H_2}}\right)^{0.5}\left[\frac{1}{E_{r,a}k_a} + \frac{\left(r_{agg} + \delta_M\right)\delta_M}{a_{agg}r_{agg}D_{H_2-M}}\right]^{-1} \tag{3.60}$$

Table 3.3: Sink terms due to the electrochemical reaction on the macro-homogeneous model.

Conservation equation	Anode CL	Cathode CL
Hydrogen (S_{H_2})	$-\frac{R_a M_{H_2}}{2\mathcal{F}}$	0.0
Oxygen (S_{O_2})	0.0	$-\frac{R_c M_{O_2}}{4\mathcal{F}}$
Water (S_{H_2O})	0.0	$-\frac{R_c M_{H_2O}}{2\mathcal{F}}$
Mass (S_{mass})	$-\frac{R_a M_{H_2}}{2\mathcal{F}}$	$-\frac{R_c M_{O_2}}{4\mathcal{F}} - \frac{R_c M_{H_2O}}{2\mathcal{F}}$

$$R_c = 4\mathcal{F}\left(\frac{p_{O_2}}{H_{O_2}}\right)\left[\frac{1}{E_{r,c}k_c} + \frac{(r_{agg}+\delta_M)\,\delta_M}{a_{agg}r_{agg}D_{O_2-M}}\right]^{-1} \tag{3.61}$$

where H_{H_2} and H_{O_2} are the Henry's constant for hydrogen and oxygen, respectively; p_{H_2} and p_{O_2} are the partial pressures of hydrogen and oxygen, respectively; D_{H_2-M} and D_{O_2-M} are the hydrogen and oxygen diffusion coefficients through the ionomer. The effective specific agglomerate surface area, a_{agg}, is defined as [94, 97]:

$$a_{agg} = \frac{m_{Pt}A_s}{\delta_{CL}}\frac{(1-\epsilon_{CL})}{L_{Pt/C}} \tag{3.62}$$

where the surface area per unit of platinum mass, A_s, is written [47, 95]:

$$A_s = \left(227.79f^3 - 158.57f^2 - 201.53f + 159.5\right) \times 10^3 \tag{3.63}$$

In order to measure the utilisation of the catalyst layer, an effectiveness factor, E_r, is considered. The effective factor is given by [97]:

$$E_{r,cl} = \frac{1}{\phi_L}\left(\frac{1}{\tanh(3\phi_L)} - \frac{1}{3\phi_L}\right) \tag{3.64}$$

where ϕ_L is the dimensional group known as Thiele's modulus and it is given by [14, 80]:

$$\phi_L = \frac{r_{agg}}{3}\sqrt{\frac{k_{cl}}{D_{eff,cl}}} \tag{3.65}$$

Here, D_{eff} is the effective diffusion of hydrogen and oxygen in the ionomer medium, and they are expressed as [80]:

$$D_{eff,a} = D_{H_2-M} L_M^{1.5} \tag{3.66}$$

$$D_{eff,c} = D_{O_2-M} L_M^{1.5} \tag{3.67}$$

The species diffusion through the ionomer is explained later in this paper. The reaction rate coefficient, k_{cl}, is expressed as [93, 95]:

$$k_a = \left(\frac{a_{Pt,a}^{eff}}{2\mathcal{F}}\right)\left[\frac{j_{0,a}^{ref}}{\left(C_{H_2}^{ref}\right)^{0.5}}\right]\left[\exp\left(\frac{(\alpha n)_a \mathcal{F}\eta}{\mathcal{R}T}\right) - \exp\left(\frac{(1-(\alpha n)_a)\mathcal{F}\eta}{\mathcal{R}T}\right)\right] \tag{3.68}$$

$$k_c = \left(\frac{a_{Pt,c}^{eff}}{4\mathcal{F}}\right)\left[\frac{j_{0,c}^{ref}}{C_{O_2}^{ref}}\right]\left[\exp\left(\frac{(\alpha n)_c \mathcal{F}\eta}{\mathcal{R}T}\right) - \exp\left(\frac{(1-(\alpha n)_c)\mathcal{F}\eta}{\mathcal{R}T}\right)\right] \tag{3.69}$$

In the agglomerate model, the water generated as a product of the electrochemical reaction is assumed to be produced in the gaseous phase. This assumption is made as the liquid water should only be present at the anode catalyst layer and gas diffusion layer if the partial pressure of water vapour reaches the saturation pressure. Hence, the source term of water due to the electrochemical reaction is defined as [41]:

$$S_{H_2O} = \frac{R_a M_{H_2O}}{F}, \tag{3.70}$$

The source and sink terms related to the electrochemical reaction in the CL for mass and species conservation equations on the agglomerate are presented in Table 3.4.

Table 3.4: Source and sink terms due to the electrochemical reaction on the agglomerate model.

Conservation equation	Anode CL	Cathode CL
Hydrogen (S_{H_2})	$-\frac{R_a M_{H_2}}{2\mathcal{F}}$	0.0
Oxygen (S_{O_2})	$\frac{R_a M_{H_2O}}{\mathcal{F}}$	$-\frac{R_c M_{O_2}}{4\mathcal{F}}$
Water (S_{H_2O})	0.0	$-\frac{R_c M_{H_2O}}{2\mathcal{F}}$
Mass (S_{mass})	$-\frac{R_a M_{H_2}}{2\mathcal{F}} + \frac{R_a M_{H_2O}}{\mathcal{F}}$	$-\frac{R_c M_{O_2}}{4\mathcal{F}} - \frac{R_c M_{H_2O}}{2\mathcal{F}}$

3.3 Transport of Multi-Water Phases

Fuel cells can operate under different operating conditions in order to maximise their energy conversion efficiency. Nevertheless, the wide range of variables results in a mix of scenarios where important quantities, such as temperature and pressure, show a significant variation. Correspondingly, the species transport and consumption are directly affected by it. When focusing on the water inside the fuel cell, the water management has been proven to have a direct impact on the overall performance of an AEM fuel cell [23, 36, 42]. Hence, there are important phenomena such as the condensation/evaporation, the sorption/desorption and the electro-osmotic drag to be considered while modelling it. Figure 3.3 schematically represents the different phenomena and water phases present in an AEM fuel cell.

It is worthwhile to notice that the different water phases have specific domains where they are considered. A summary of the source terms for the macro-homogeneous and agglomerate model with respect to the interaction between the water phases is presented in Table 3.5 and Table 3.6, respectively. Further

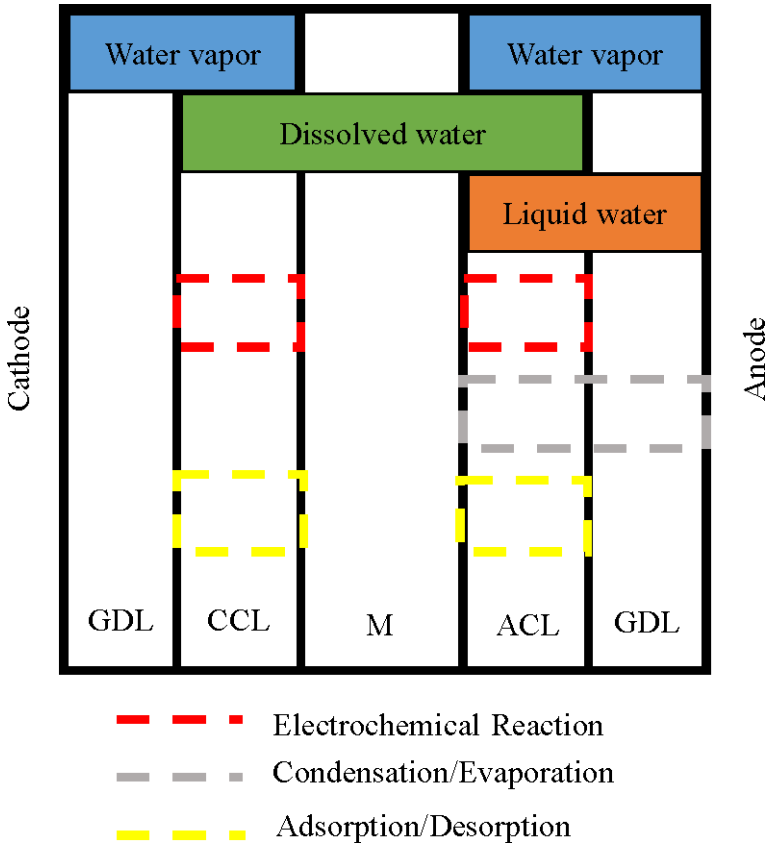

Figure 3.3: Schematic representation of the different water phases in an AEM fuel cell.

explanation of specific water phases is also provided in the following sections.

3.3.1 Transport of Water Vapour

The transport of the water vapour phase in the macro-homogeneous and agglomerate model is described by Equations (3.9) and (3.29), respectively. Despite the previous sink and source terms due to the electrochemical reaction, there are other important phenomena related to the water vapour and its interaction between other water phases. Due to the operating conditions, if the water vapour reaches the saturation pressure, the condensation phenomenon occurs and the liquid water is formed. Therefore, S_{vl} is the phase change between water vapour

Table 3.5: Summary of the source and sink terms due to the interaction between water phases in the macro-homogeneous model

Conservation equation	Anode CL	Anode GDL	Cathode CL
Vapour phase (S_{H_2O})	$-S_{vl}$	$-S_{vl}$	$+S_{sd}\left(M_{H_2O}\frac{\rho_m}{EW}\right)$
Liquid water phase (S_l)	$\frac{R_a M_{H_2O}}{\mathcal{F}} + S_{vl} + S_{sd}\left(M_{H_2O}\frac{\rho_m}{EW}\right)$	S_{vl}	0.0
Dissolved Phase (S_d)	$-S_{sd}$	0.0	$-S_{sd}$

and liquid water phase, and is described as [83]:

$$S_{vl} = \begin{cases} \gamma_{evap}\epsilon s\frac{\left(p_{H_2O}-p_{sat}\right)M_{H_2O}}{\mathcal{R}T} & if\ p_{H_2O} < p_{sat} \\ \gamma_{cond}\epsilon\left(1-s\right)\frac{\left(p_{H_2O}-p_{sat}\right)M_{H_2O}}{\mathcal{R}T} & if\ p_{H_2O} > p_{sat} \end{cases} \tag{3.71}$$

where γ_{evap} and γ_{cond} are the evaporation and condensation rate, respectively; p_{sat} is the saturated pressure and it is described by the following empirical equation [41]:

$$p_{sat} = 10^{-2.1794+0.02953(T-273.15)-9.1837\times10^{-5}(T-273.15)^2+1.445\times10^{-7}(T-273.15)^3} \tag{3.72}$$

From the assumptions listed before, only water vapour phase is present at the flow channel, thus no condensation or evaporation phenomena is considered at the flow channel.

Table 3.6: Summary of the source and sink terms due to the interaction between water phases in the agglomerate model.

Conservation equation	Anode CL	Anode GDL	Cathode CL
Vapour phase (S_{H_2O})	$-S_{vl} + S_{sd}\left(M_{H_2O}\frac{\rho_m}{EW}\right)$	$-S_{vl}$	$+S_{sd}\left(M_{H_2O}\frac{\rho_m}{EW}\right)$
Liquid water phase (S_l)	S_{vl}	S_{vl}	0.0
Dissolved Phase (S_d)	$-S_{sd}$	0.0	$-S_{sd}$

3.3.1.1 Macro-homogeneous model

With respect to the water phase change, the source term of the water conservation equation is defined as [59]:

$$S_{H_2O} = \begin{cases} -S_{vl} & at\ anode\ GDL \\ -S_{vl} & at\ anode\ CL \\ +S_{sd}\left(M_{H_2O}\frac{\rho_m}{EW}\right) & at\ cathode\ CL \end{cases} \tag{3.73}$$

where S_{dv} is the process of sorption and desorption in the electrolyte, that will be presented later in this chapter; EW and ρ_m are the equivalent molecular weight of the dry membrane and the dry membrane density, respectively.

3.3.1.2 Agglomerate model

The interaction between vapour and liquid water phase in the agglomerate model is also governed by Equation (3.71). Nevertheless, with respect to the interaction between vapour and dissolved water, the proposed agglomerate model considers the sorption and desorption phenomena in the anode catalyst layer to occur between the vapour and the dissolved water phase. Hence, the source term of

water species with respect to water phase change can be defined as [60]:

$$S_{H_2O} = \begin{cases} -S_{vl} & at\ anode\ GDL \\ -S_{vl} + S_{sd}\left(M_{H_2O}\frac{\rho_m}{EW}\right) & at\ anode\ CL \\ +S_{sd}\left(M_{H_2O}\frac{\rho_m}{EW}\right) & at\ cathode\ CL \end{cases} \tag{3.74}$$

3.3.2 Transport of Liquid Water

The steady-state continuity equation for a multiphase flow can be written with respect of each k phase as:

$$\nabla \cdot (\rho_k \vec{u}_k) = S_k \tag{3.75}$$

where ρ_k is the superficial phase density of the k phase in the entire volume. Due to the fact that the superficial phase density is a variable, it is necessary to realise an averaging procedure, which turns Equation (3.75) into:

$$\nabla \cdot (\epsilon_k \langle \rho_k \rangle \langle \vec{u}_k \rangle) = S_k \tag{3.76}$$

where $\langle\rangle$ and ϵ_k are the volume averaged property and the volume fraction of phase k inside the total volume. The volume fraction of phase k can be written as [91]:

$$\epsilon_k = \epsilon s \tag{3.77}$$

where ϵ is the porosity, accounted as the void space within the total volume, and s is the liquid saturation, defined as [83]:

$$s = \frac{volume\ of\ liquid}{volume\ of\ void} \tag{3.78}$$

The source term in Equation (3.76) stands for the interfacial mass transfer between different phases and, if appropriated, for the source term due to the chemical reaction, and it is defined as [91]:

$$\Gamma_{M,k} = S_k + \sum \Gamma_{s,k} \tag{3.79}$$

where $\Gamma_{s,k}$ is the gain or loss of phase k from adjacent phase s. Applying the

volume averaged continuity equation into the mass conservation equation, the liquid phase mass conservation equation becomes [91]:

$$\nabla \cdot (\epsilon \langle \rho_l \rangle \langle \vec{u}_l \rangle) = S_l \tag{3.80}$$

where S_l is the source term of liquid water phase; $\langle \rho_l \rangle$ is the volume averaged density, and for sake of convenience, it will be considered as a constant ($\rho_l = 970.0$ km/m^3) and brackets will be omitted.

In a porous media, the liquid velocity is dependent on the permeability of the medium and the pressure gradient of the liquid water phase. It can be approximated by Darcy's law as follows:

$$\epsilon s \langle \vec{u}_l \rangle = \vec{u}_l = -\frac{k_l}{\mu_l} \nabla P_l \tag{3.81}$$

where $\vec{u}_l$ is the superficial velocity of the liquid water, K_{rl} and K are the relative permeability of the liquid phase and the intrinsic permeability of the porous media, respectively. The correction of the permeability for liquid water used by Jiao and Li [41] is applied in this model:

$$k_l = K_0 s^n \tag{3.82}$$

where k_l is the effective permeability of the liquid phase and n is the Bruggemann correction [13]. Rearranging Equation (3.81) into Equation (3.80), we obtain the continuity equation for the water liquid phase:

$$\nabla \cdot (\rho_l \vec{u}_l) = S_l \tag{3.83}$$

The capillary pressure, P_c, which is related to the liquid water phase, is obtained by:

$$P_c = P_l - P_g \tag{3.84}$$

and now substituting Equation (3.81) into (3.84) we get:

$$\vec{u}_g = -\frac{k_l}{\mu_l} \nabla P_g - \frac{k_l}{\mu_l} \nabla P_c \tag{3.85}$$

Applying Darcy's law to the gas phase

$$\nabla P_g = -\frac{\mu_g}{k_g}\vec{u}_g \tag{3.86}$$

and combining with Equations (3.83), (3.85) and (3.86) we obtain [9]:

$$\nabla \cdot \left(-\frac{\rho_l k_l}{\mu_l}\nabla P_c + \frac{\rho_l \mu_g k_l}{\mu_l k_g}\vec{u}_g\right) = S_l \tag{3.87}$$

where μ_g is the dynamic viscosity of the gas phase. The capillary pressure can be expressed as function of the liquid saturation by[9]:

$$P_c = f(s) \Rightarrow \nabla P_c = \frac{dP_c}{ds}\nabla s \tag{3.88}$$

where P_c is then computed, due to the lack of experimental data regarding capillary pressure in PEM fuel cell, by the use of Laverett function [54]

$$P_c(s) = \sigma cos(\theta)\sqrt{\frac{\epsilon}{K_0}}\left(1.417s - 2.120s^2 + 1.263s^3\right) \tag{3.89}$$

where σ and θ stand for the surface tension and the contact angle of the porous material, respectively. Hence, by substituting Equation (3.88) into (3.87), we obtain the liquid water transport equation as it follows[9]:

$$\nabla \cdot \left(\left(-\frac{\rho_l k_l}{\mu_l}\frac{dP_c}{ds}\right)\nabla s + \frac{\rho_l \mu_g k_l}{\mu_l k_g}\vec{u}_g\right) = S_l \tag{3.90}$$

3.3.2.1 Macro-homogeneous model

The source term of liquid water in the macro-homogeneous model has the following form [59]:

$$S_l = \begin{cases} S_{vl} & at\ anode\ GDL \\ \frac{R_a M_{H_2O}}{\mathcal{F}} + S_{vl} + S_{sd}\left(M_{H_2O}\frac{\rho_m}{EW}\right) & at\ anode\ CL \end{cases} \tag{3.91}$$

With respect to the source term in the anode CL, the first term in the right hand side (RHS) stands for the water production from the electrochemical reaction in the liquid phase, the second term is responsible for the characterisation the condensation/evaporation phenomena defined in the Equation (3.71) and the

last term accounts for the sorption/desorption phenomena in the electrolyte.

3.3.2.2 Agglomerate model

The same approach for the water phase change phenomena is considered in the agglomerate model. Nevertheless, as previously mentioned, the assumption of water being produced in the liquid water and the interaction between dissolved and liquid water phase are no longer valid for the agglomerate model. Hence, the liquid water source term for the agglomerate model is defined as [59, 60]:

$$S_l = \begin{cases} S_{vl} & at\ anode\ GDL \\ S_{vl} & at\ anode\ CL \end{cases} \tag{3.92}$$

3.3.3 Dissolved water content

From our list of assumptions, one can see that the membrane is assumed to be impenetrable to all species but water in the dissolved phase. This phase is defined as the water allocated in the pores of the polymer electrolyte. As one can see in Figure 3.4, the dissolved water has two main mechanisms of transportation: the electro-osmotic drag and the concentration gradient. The first is described as the water transportation due to the anions diffusion from cathode to anode side. The latter is characterised by the diffusion driven by the water activity gradient between catalyst layers.

The governing equation of dissolved water, proposed by Springer et al. [79], describes the transport of dissolved water due to diffusion and also the electro-osmotic drag and it is presented as:

$$-\nabla \cdot (D_d \nabla C_d) + \nabla \cdot \left(\frac{n_d}{\mathcal{F}} \vec{J}_m \right) = S_d \tag{3.93}$$

where D_d is the dissolved water diffusivity; C_d is the dissolved water concentration; n_d is the electro-osmotic drag coefficient; $\vec{J}_m$ is the, later defined, membrane phase current density; S_d is the source term of dissolved water. Another widely used approach is to present the previous relation in term of the membrane water

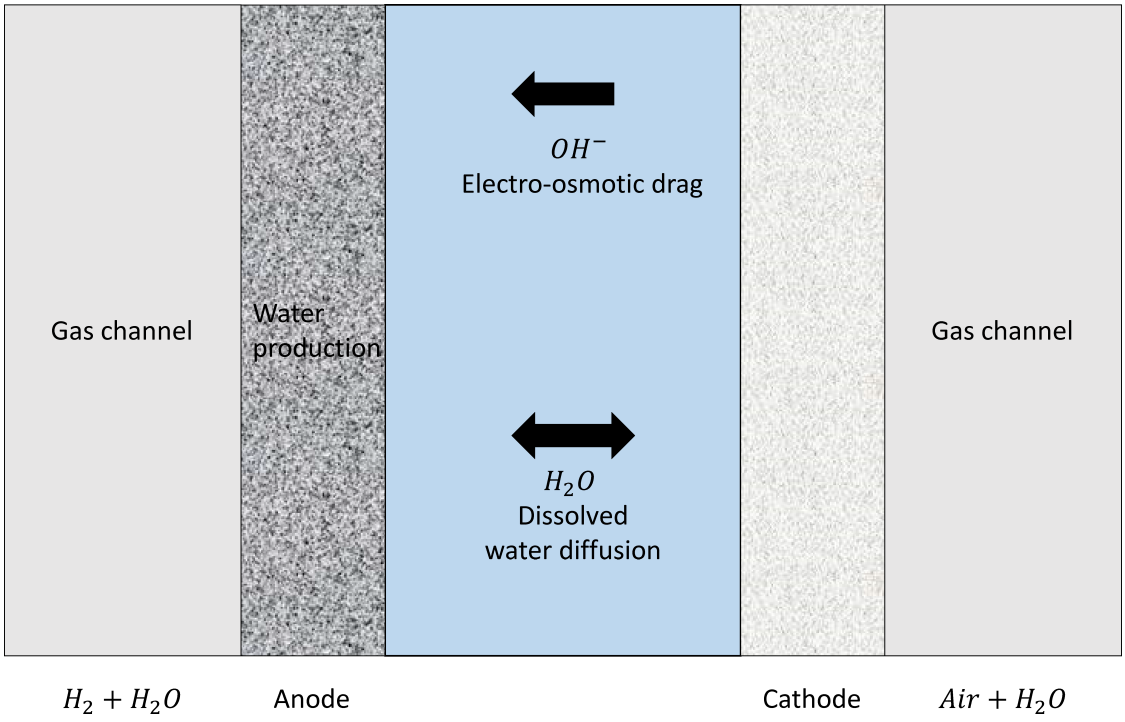

Figure 3.4: Schematic representation of the electro-osmotic drag and dissolved water diffusion phenomena.

content, λ, which can be defined as [83]:

$$\lambda = \frac{EW}{\rho_M} C_d \tag{3.94}$$

Equation (3.94) describes the membrane water content as the ratio of the wet and dry membrane, or in other words, the number of water molecules per sulfonic acid group. The dissolved water diffusivity is also corrected by the ionomer volume fraction present in the catalyst layer. Thus, one can describe the effective dissolved water diffusion coefficient as [42]:

$$D_d^{eff} = L_M^{1.5} D_d \tag{3.95}$$

Substituting the Equations (3.94) and (3.96) into (3.93) we obtain [92]:

$$-\nabla \cdot \left(D_d^{eff} \nabla \lambda \right) + \nabla \cdot \left(\frac{EW}{\rho_M} \frac{n_d}{\mathcal{F}} \vec{J}_m \right) = S_d. \tag{3.96}$$

3.3.3.1 Macro-homogeneous model

The dissolved water content diffusivity has a dependence not only on the membrane water content, but also on temperature. The following correlation is used to express the behaviour of the dissolved water diffusivity [23, 36]

$$D_d = \begin{cases} (0.0051\lambda T_0 - 1.44\lambda) \times 10^{-10} & 0.0 \leq \lambda \leq 14.0 \\ \left[\left(-23.2404 + 4.513\lambda - 0.28926\lambda^2 + 0.006131\lambda^3\right)(T_0 - 303.15)\right. & \\ \left. -79.826 + 17.928\lambda - 1.3329\lambda^2 + 0.03337\lambda^3\right] \times 10^{-10} & 14.0 < \lambda \leq 19.0 \\ \left[\left(-41.916 + 0.00613\lambda^3\right)(T_0 - 303.15) + 8.5139\right] \times 10^{-10} & \lambda > 19.0 \end{cases} \tag{3.97}$$

The electro-osmotic drag coefficient, n_d, which is described as the amount of water dragged by each anion, has been experimentally correlated in literature [27, 56, 58], but in the macro-homogeneous model, the Springer et al.[79] approach is used and thus n_d is given by:

$$n_d = \frac{2.5}{22}\lambda \tag{3.98}$$

Berg et al.[6] proposed a non-equilibrium approach for the water sorption in the electrolyte. The proposed model considers the difference between the equilibrium sorption value and the local membrane water content to be proportional to the flux into and out of the electrolyte in the catalyst layer. The equilibrium sorption value (λ_e), also denominates equilibrium water content, which was proposed by Springer et al.[79] in the following manner:

$$\lambda_e = \begin{cases} \left(-0.605a^3 + 0.85a^2 - 0.205a + 0.153\right)(T_0 - 313.15) & \\ +39.0a^3 - 47.7a^2 + 23.4a + 0.117 & 0 \leq a \leq 1.0 \\ \left(-0.00265a + 0.05795\right)(T_0 - 313.15) & \\ +1.5915\,(a-1) + 14.817 & 1.0 < a \leq 3.0 \end{cases} \tag{3.99}$$

where a is the water activity. In the macro-homogeneous model, the water activity is function of the relativity humidity and liquid water. Hence, one can determine

the water activity by the following equation [43]:

$$a = \frac{\mathcal{R}T}{p_{sat}} C_{H_2O} + 2s, \tag{3.100}$$

where C_{H_2O} is the water molar concentration in the vapour phase.
The sorption and desorption phenomena are described as [42, 97]:

$$S_{sd} = \gamma_d(\lambda - \lambda_e) \tag{3.101}$$

Thus, the source term of Equation (3.96), can be defined as [59]:

$$S_d = -S_{sd} \tag{3.102}$$

where γ_d is the water transfer rate.

3.3.3.2 Agglomerate model

It is worth mentioning that the results present in Chapter 6 still considers the electro-osmotic drag coefficient presented in Equation (3.98). Therefore, with respect to the dissolved water phase, the first agglomerate model proposed has not been modified. Nevertheless, even though the transport of dissolved water in the latest proposed agglomerate model remains the same as the previous models, some of the properties were adjusted and switched to better translate the appropriated physics in the AEM dissolved water phase. Hence, the electro-osmotic drag coefficient in the agglomerate model is described as [42, 56]

$$n_d = 0.183\lambda + 1.3 \tag{3.103}$$

In addition to the aforementioned change in the electro-osmotic drag coefficient, the equilibrium water content is also modified in the latest agglomerate model. The membrane water content in an equilibrium hydration state was extrapolated from Bharath et al. [10] and it is evaluated as:

$$\lambda_e = \left(18.385\sqrt{a} + 5.8955a + 0.8161\right)\gamma_e \tag{3.104}$$

where γ_e is the ionomer water content factor. Zeng et al. [100]presented an alkaline ionomer with adjustable water uptake based on hydrophobic and hydro-

philic properties.

The water activity, a, is now defined as a function of vapour and saturated water pressures only, and it is presented as [83]:

$$a = \frac{X_{H_2O} p_g}{p_{sat}} \tag{3.105}$$

3.4 Transport of Electric Charge

3.4.1 Conservation of Electronic Charge

The transport of electronic charge is defined by Fourier's law and the conservation equation of electrical charge is given as [18]:

$$\nabla \cdot \left(\vec{J}_S\right) = S_S \tag{3.106}$$

where $\vec{J}_S$ is defined as the electronic current density through the solid phase, and the source term of the equation, S_S, is the consumption or generation of electrons. Although $\vec{J}_S$ is a 3D vector quantity, the only direction that is favourable to the increment of the output power is the one normal to the GDL surface. Once the remaining components of the vector do not work to improve the output power, they should be minimised by a different design proposal. The electronic potential is related to the current density by Ohm's law, and it its described as follows

$$\vec{J}_S = -\kappa_S^{eff} \nabla \phi_S \tag{3.107}$$

where κ_S^{eff} and ϕ_S are the effective electric conductivity and the electronic potential in the solid phase respectively.

3.4.1.1 Macro-homogeneous model

The electric conductivity, κ_S, is corrected by the porosity (ϵ) and ionomer volume fraction in the CL (L_M), and by using the Bruggemann correction [13] with an exponent of 1.5, it is defined as follows [42]:

$$\kappa_S^{eff} = (1 - \epsilon - L_M)^{1.5} \kappa_S \tag{3.108}$$

Rearranging Equations (3.106) and (3.107) we have:

$$\nabla \cdot \left(-\kappa_S^{eff} \nabla \phi_S\right) = S_S \tag{3.109}$$

According to the reactions inside the fuel cell, electrons are generated at the ACL and consumed at the CCL. Thus, the source term of the conservation equation of electronic charge is defined as [42, 59]:

$$S_S = \begin{cases} R_a & at\ anode\ CL \\ -R_c & at\ cathode\ CL \end{cases} \tag{3.110}$$

3.4.1.2 Agglomerate model

The conservation equation of electronic charge does not differ from Equation (3.108). Nevertheless, the electronic conductivity is corrected with respect to the volume fraction of platinum dispersed carbon ($L_{Pt/C}$) as follows [97]:

$$\kappa_S^{eff} = \left(L_{Pt/C}\right)^{1.5} \kappa_S \tag{3.111}$$

The source term for the conservation equation of electronic charge remains the same as the source term presented in Equation (3.109).

3.4.2 Conservation of Ionic Charge

The governing equation of ions is also expressed by Fourier's law and can be written as [18]:

$$\nabla \cdot \left(\vec{J}_m\right) = S_m \tag{3.112}$$

where $\vec{J}_m$ and S_m stands for the ionic current density and source term for proton generation or depletion respectively. The ionic conservation equation is solved only at the membrane and catalyst layer domain. Similar to the electronic current density, the ionic current density is related by Ohm's law and can be defined as:

$$\vec{J}_m = -\kappa_m^{eff} \nabla \phi_m \tag{3.113}$$

where κ_m is the ionic conductivity and ϕ_m is the ionic potential in the membrane

and catalyst layer.

3.4.2.1 Macro-homogeneous model

Similar to the electronic conductivity, the ionic conductivity κ_m is corrected by the porosity (ϵ) and also by the Bruggemann correction [13] as

$$\kappa_m^{eff} = (1-\epsilon)^{1.5}\,\kappa_m. \tag{3.114}$$

Duan et al. [24] measured the ionic conductivity at 50^oC and 80^oC accounting for different water activity and water content. The correlation proposed has a dependence of the local water activity, a_w, and is presented as [42]:

$$\begin{aligned}\kappa_m = 0.1334 - 3.882\times10^{-4}T_0 + (0.01148T_0 - 3.909)\,a_w \\ - (0.06690T_0 - 23.01)\,a_w^2 + (0.1227T_0 - 42.61)\,a_w^3 \\ - (0.06021T_0 - 21.80)\,a_w^4\end{aligned} \tag{3.115}$$

where

$$\begin{aligned}a_w = 0.8118 - 2.296\times10^{-3}T_0 + \left(5.815\times10^{-3} - 2.005\right)\lambda \\ - \left(2.977\times10^{-3}T_0 - 1.046\right)\lambda^2 + \left(4.825\times10^{-4}T_0 - 0.1676\right)\lambda^3 \\ - \left(3.179\times10^{-5}T_0 - 0.01094\right)\lambda^4 + \left(7.427\times10^{-7} - 2.539\times10^{-4}\right)\lambda^5\end{aligned} \tag{3.116}$$

Substituting Equation (3.113) into Equation (3.112), we have [18]:

$$\nabla\cdot\left(-\kappa_m^{eff}\nabla\phi_m\right) = S_m. \tag{3.117}$$

Equation (3.118) presents the source and sink term of ions in the ACL and CCL, respectively [42, 59]:

$$S_m = \begin{cases} -R_a & at\ anode\ CL \\ R_c & at\ cathode\ CL \end{cases} \tag{3.118}$$

3.4.2.2 Agglomerate model

In the agglomerate model, the ionic conductivity is corrected in the following manner[80]:

$$\kappa_m^{eff} = L_M^{1.5} \kappa_m. \tag{3.119}$$

Similarly to the ionic conductivity in the macro-homogeneous model, the ionic conductivity in the agglomerate model is dependent on the dissolved water phase present at the catalyst layer and membrane. Thus, based on the ionic conductivity measured by Duan et al. [24], the ionic conductivity is extrapolated as a function of the membrane water content as:

$$\kappa_m = (8 \times 10^{-8}\lambda^5 + 1 \times 10^{-5}\lambda^4 - 4 \times 10^{-4}\lambda^3 + 7.4 \times 10^{-3}\lambda^2 + 0.024\lambda - 0.035) \times 4.4 \tag{3.120}$$

As the ion mobility of OH^- is higher than the HCO_3^-, the ionic conductivity has to be corrected accordingly. In this thesis, the ionic mobility is corrected by a factor of 4.4 [99].

3.5 Energy Conservation Equation

Despite the fact that the temperature does not show a large variation in AEM fuel cells, it is a parameter to be considered in the numerical simulation due its strong relation with the different water phases inside the domain. One important simplification considered in this model is that the vapour and solid phase are at thermal equilibrium state. So, the energy transport equation can be defined as [26]:

$$\nabla \cdot (\vec{u}_g (\rho_g E_g + P_g)) = \nabla \cdot \left[k^{eff} \nabla T - \left(\sum_i h_i \vec{N}_i \right) + \left(\bar{\bar{\tau}} \cdot \vec{u}_g \right) \right] + S_E \tag{3.121}$$

where k^{eff} is the effective thermal conductivity; $\vec{N}_i$ is the diffusion flux of the ith

species; h is the enthalpy, E is the total energy of a respective phase; S_E is the heat source term.

The effective thermal conductivity in porous medium is defined as [26]:

$$k^{eff} = \epsilon k_g + (1 - \epsilon)\, k_s \tag{3.122}$$

where k_g and k_s stand for the thermal conductivity of the gas and solid phase, respectively. The solid thermal conductivity is directly defined, whereas in the gaseous phase thermal conductivity is calculated based on the kinetic theory as [26, 95]:

$$k_g = \sum_i \frac{X_i k_i}{\sum_j X_j \phi_{ij}} \tag{3.123}$$

where

$$\phi_{i,j} = \frac{\left[1 + \left(\frac{\mu_i}{\mu_j}\right)^{1/2} \left(\frac{M_i}{M_j}\right)^{1/4}\right]^2}{\left[8\left(1 + \frac{M_i}{M_j}\right)\right]^{1/2}}. \tag{3.124}$$

The total energy term presented in Equation (3.121) can be defined as

$$E = h - \frac{p}{\rho} + \frac{v^2}{2}. \tag{3.125}$$

In order to define the sensible enthalpy for ideal gas, Equation 3.126 is used as follows

$$h = \sum_i Y_i h_i, \tag{3.126}$$

and

$$h_i = \int_{T^{ref}}^{T} C_{p,i} dT, \tag{3.127}$$

where $C_{p,i}$ is the specific heat for the i^{th} species. For the solid phase, the sensible enthalpy is defined as

$$h = \int_{T^{ref}}^{T} C_p dT, \tag{3.128}$$

Table 3.7: Thermal conductivity and specific heat of the solid components [92].

Parameter	Value	Unity
Thermal conductivity of CL, k_{CL}	1.0	$W/m \cdot K$
Thermal conductivity of GDL, k_{GDL}	1.0	$W/m \cdot K$
Thermal conductivity of Membrane, k_m	0.95	$W/m \cdot K$
Thermal conductivity of BP, k_{BP}	20.0	$W/m \cdot K$
Specific heat of CL, $C_{p,CL}$	3300.0	$J/kg \cdot K$
Specific heat of GDL, $C_{p,GDL}$	568.0	$J/kg \cdot K$
Specific heat of membrane, $C_{p,m}$	833.0	$J/kg \cdot K$
Specific heat of BP, $C_{p,BP}$	1580.0	$J/kg \cdot K$

where C_p is the heat capacity of the solid material. The thermal conductivity and heat capacity values of the solid components of the representative AEM fuel cell are presented in Table 3.7.

3.5.0.1 Macro-homogeneous model

With respect to the gaseous thermal conductivity, the macro-homogeneous model considers the use of bulk properties in order to compute the effective thermal conductivity, as presented in Table 3.8.

The heat generation term, S_E, accounts for the different heat generation inside the fuel cell, including the reversible heat generation, irreversible heat generation, the ohmic heat produced, latent heat regarding the phase change and also the sorption/desorption process. These five types of heat generation are presented in the ACL as it follows [42]:

Table 3.8: Thermal conductivity of fluids [92].

Parameter	Value	Unity
Thermal conductivity of hydrogen, k_{H2}	0.204	$W/m \cdot K$
Thermal conductivity of air, k_{Air}	0.03	$W/m \cdot K$
Thermal conductivity of water vapour, $k_{H_2O,v}$	0.023	$W/m \cdot K$
Thermal conductivity of liquid water, $k_{H_2O,l}$	0.67	$W/m \cdot K$

$$S_E = \frac{R_a T \Delta S}{2\mathcal{F}} + |R_a \eta_a| + \|\nabla \phi_S\|^2 \kappa_S^{eff} + \|\nabla \phi_m\|^2 \kappa_m^{eff} + \left(S_l + S_d M_{H_2O} \frac{\rho_{mem}}{EW}\right) h_{lat} \tag{3.129}$$

where ΔS (=163303.5 $J/kmol.K$) is the entropy change of the HOR, h_{lat} is the latent heat due to phase change. The heat generation in the CCL is similar to the ACL, thus, can be written as [42]:

$$S_E = |R_c \eta_c| + \|\nabla \phi_S\|^2 \kappa_S^{eff} + \|\nabla \phi_m\|^2 \kappa_m^{eff} + S_d M_{H_2O} \frac{\rho_{mem}}{EW} h_{lat} \tag{3.130}$$

The heat generation in the anode GDL has to take into account the evaporation/condensation process. Thus, the source term of heat for the GDL can be written as [42]:

$$S_E = \|\nabla \phi_S\|^2 \kappa_S^{eff} + S_l h_{fg} \tag{3.131}$$

The heat generation in the bipolar plate is exclusive due to the Ohmic heating, and its source term is specified as [42]:

$$S_E = \|\nabla \phi_S\|^2 \kappa_S^{eff} \tag{3.132}$$

Similarly to the heat in the bipolar plate, the heat generation in the membrane

is due to the ohmic heating and is defined as [42]:

$$S_E = \|\nabla\phi_m\|^2 \kappa_m^{eff} \tag{3.133}$$

In the flow channel, no heat source is applied. Hence, the energy source term in the flow channel is specified as follows [42]:

$$S_E = 0.0 \tag{3.134}$$

3.5.0.2 Agglomerate model

As previously mentioned in this chapter, the thermal conductivity of the gaseous phase, in the agglomerate model, is obtained by the kinetic theory. Therefore, the individual thermal conductivity of the species i, k_i, is defined as [26]

$$k_i = \frac{15}{4}\frac{\mathcal{R}}{M_i}\mu_i\left(\frac{4}{15}\frac{C_{p,i}M_i}{\mathcal{R}} + \frac{1}{3}\right) \tag{3.135}$$

With respect to the source term of the conservation equation of energy, no modification was necessary and the same source terms for the macro-homogeneous model were considered.

3.6 Boundary and Initial Conditions

3.6.1 Boundary Conditions

A completed set of governing equations has already been presented in previous sections of this chapter and, to complete the formulation, it is necessary to define boundary conditions for them. These boundary conditions represent operational parameters such as mass flow rate of the reactants, relative humidity and concentration of the reactants, inlet temperature, operating pressure and voltage output. These boundaries are applied in the external surfaces of the single computational domain according to Figure 3.5, where A, B, C, D and E represent the surfaces of the domain where a specific boundary condition is required.

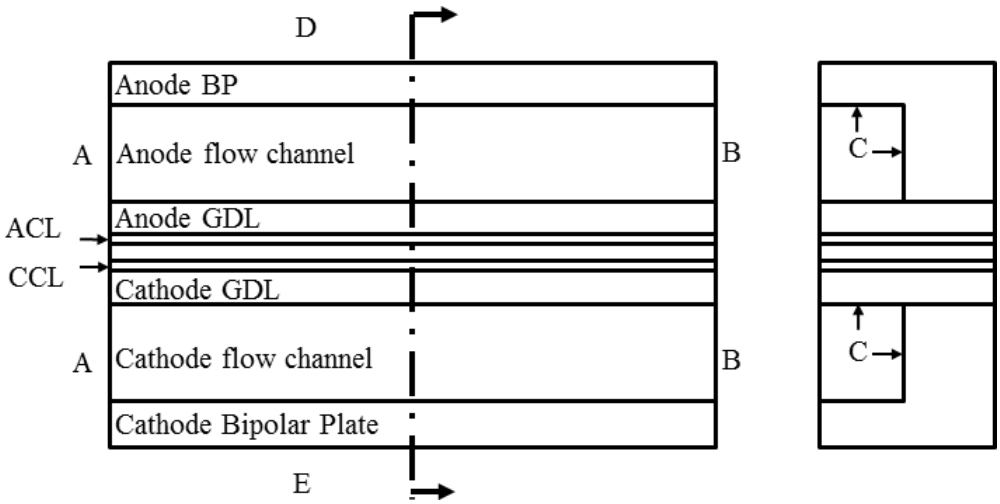

Figure 3.5: Boundary condition scheme for a single channel domain.

3.6.1.1 Macro-homogeneous model

At the inlet of both cathode and anode gas flow channel, temperature of the fluid flow, concentration and mass flux are specified. For variables not explicitly defined, zero flux condition is applied.

$$\left\{ \begin{array}{c} \dot{m} \cdot \vec{n} = Constant \\ C_i = Constant \\ T = T_0 \\ \frac{\partial \theta}{\partial \vec{n}} = 0 \end{array} \right\} at\ A \tag{3.136}$$

To compute the mass flux, additional parameters such as the stoichiometric ratio, ξ, reference current density, J^{ref}, and the active reaction area A are necessary. The mass flux for anode and cathode, respectively, are defined as [36]:

$$\dot{m}_a = \frac{\rho_g \xi_a J^{ref} A}{2\mathcal{F} C_{H_2}} \tag{3.137}$$

$$\dot{m}_c = \frac{\rho_g \xi_c J^{ref} A}{4\mathcal{F} C_{O_2}} \tag{3.138}$$

The relativity humidity of the inlet flows is an important parameter, hydrogen and oxygen relations as a function of the relative humidity are presented,

respectively, as [36]:

$$C_{H_2} = \frac{(p_a - RH_a p_{sat})}{\mathcal{R}T_0} \tag{3.139}$$

$$C_{O_2} = \frac{0.21\,(p_c - RH_c p_{sat})}{\mathcal{R}T_0} \tag{3.140}$$

where p_a and p_c are the inlet pressure at anode and cathode, respectively; T_0 is the inlet temperature; RH_a and RH_c are the relative humidity of the gas flow at the anode and cathode inlet, respectively. The coefficient 0.21 in Equation (3.140) stands for the molar fraction of oxygen in air composition. At the flow channel outlet, the pressure is specified as [36, 42]:

$$\left\{ \begin{array}{c} P = Constant \\ \frac{\partial \theta}{\partial \vec{n}} = 0 \end{array} \right\} at\ B \tag{3.141}$$

At the walls of the flow channel, no-slip boundary conditions are applied. Other variables boundary conditions are set as zero flux boundary condition.

$$\left\{ \begin{array}{c} \vec{u} = Constant \\ \frac{\partial \theta}{\partial \vec{n}} = 0 \end{array} \right\} at\ C \tag{3.142}$$

On the top and bottom surface of the anode and cathode bipolar plate, respectively, where the electronic potential is defined.

$$\left\{ \begin{array}{c} \phi_{ele} = \eta_{total} \\ T = T_0 \\ \frac{\partial \theta}{\partial \vec{n}} = 0 \end{array} \right\} at\ D \tag{3.143}$$

$$\left\{ \begin{array}{c} \phi_{ele} = 0.0 \\ T = T_0 \\ \frac{\partial \theta}{\partial \vec{n}} = 0 \end{array} \right\} at\ E \tag{3.144}$$

where η_{total} is the total overpotential. The theoretical reversible energy can be

written in a modified version of the Nernst equation as [45]

$$\phi_{rev} = \frac{\Delta G_{ref}}{2\mathcal{F}} + \frac{\Delta S_{ref}}{2\mathcal{F}}\left(T - T_{ref}\right) + \frac{\mathcal{R}T}{2\mathcal{F}} \ln\left[\left(\frac{p_{H_2}}{p_{ref}}\right)\left(\frac{p_{O_2}}{p_{ref}}\right)^{1/2}\right] \tag{3.145}$$

Thus, rearranging the Equation (1.8) we obtain

$$\eta_{total} = \phi_{rev} - \phi_{cel} \tag{3.146}$$

For variables not mentioned before, a zero flux or symmetry boundary condition is applied.

$$\left\{ \frac{\partial\theta}{\partial\vec{n}} = 0 \right\} \tag{3.147}$$

3.6.1.2 Agglomerate model

The boundary conditions of the first developed agglomerate model are consistent with the macro-homogeneous model. Nevertheless, it has been observed that the cooling of the fuel cell is partially a consequence of the free stream in contact with the top and bottom surface of the bipolar plate [55, 89]. Hence, the boundary condition at surfaces D and E has been modified as shown

$$\left\{ \begin{array}{c} \phi_{ele} = \eta_{total} \\ \dot{q} = h\left(T - T_{\infty}\right) \\ \frac{\partial\theta}{\partial\vec{n}} = 0 \end{array} \right\} at\ D \tag{3.148}$$

$$\left\{ \begin{array}{c} \phi_{ele} = 0.0 \\ \dot{q} = h\left(T - T_{\infty}\right) \\ \frac{\partial\theta}{\partial\vec{n}} = 0 \end{array} \right\} at\ E \tag{3.149}$$

where $\dot{q}$ is the heat flux; T_{∞} is the ambient temperature; h is the heat transfer coefficient and it is assumed to be 100 $W/m^2 \cdot K$.

3.6.2 Initial Conditions

The initial conditions to all variables except for temperature and species concentration are defined as zero. The temperature and concentration initial conditions are specified to be the same as in Equation (3.136).

3.7 Parameters

The solution of the model depends on the initial and boundary conditions and also on the structural parameters that characterise the fuel cell. The structural parameters used to describe the physical domain of a representative fuel cell are presented in Table 3.9. It is worth mentioning that the parameters presented in Table 3.9 are the same for both the macro-homogeneous and agglomerate model, unless stated otherwise.

3.8 Summary

In this chapter an overview of both the macro-homogeneous and agglomerate models used in this thesis is presented. A complete set of 12 conservation equations composed of two equations for the conservation of the electric charge, one equation for energy conservation, one equation for the conservation of liquid water phase, one equation for the dissolved water phase and also equations for mass, momentum and species conservation for the gas phase are presented and their respective boundary conditions.

The aforementioned equations are coupled either by the electrochemical reaction or by their source terms in the RHS, which account for different phenomena such as the interfacial mass transfer amongst different phases. With the increase of the complexities of the agglomerate model, it is expected that the results from the numerical simulation are as close as possible to those from real experiments. Nevertheless, it is worthwhile to notice that, due to the lack of information in the existing literature regarding some of the parameters of an AEM fuel cell, some of the parameters (i.e. sorption and desorption coefficient rates, Henry's constant) necessary to carry out the simulations have to be fitted or to utilise corresponding values from PEM studies.

Table 3.9: Structural parameters[42, 77].

Parameter	Value	Unity
Thickness of the CL, δ_{CL}	10.0	μm
Thickness of the GDL, δ_{GDL}	200.0	μm
Thickness of the membrane, δ_m	28.0	μm
Gas channel length	100.0	mm
Gas channel depth	0.5	mm
Gas channel width	1.0	mm
Porosity of the CL, ϵ_{CL}	0.3	-
Porosity of the GDL, ϵ_{GDL}	0.6	-
Intrinsic permeability of CL, $K_{0,CL}$	6.2×10^{-13}	$1/m^2$
Intrinsic permeability of GDL, $K_{0,GDL}$	6.2×10^{-12}	$1/m^2$
Ionomer volume fraction, L_M	0.22	-

Finally, even though the agglomerate model has been implemented on PEMFC, it is yet to be implemented on AEM fuel cell. On the agglomerate model, key transport phenomena such as the diffusion of species and ions through the ionomer layer covering the platinum dispersed carbon, earlier neglected on the macro-homogeneous model, are now taken into account. Additionally to that, due to the implementation of the agglomerate model, a more realistic representation of the catalyst layers and their composition (e.g. carbon and platinum loading, ionomer content, ionomer thickness layer) is now possible. Consequently, it is feasible to analyse the effect of catalyst layer parameters on the different quant-

ities transport and its effect on the overall performance of the fuel cell.

Chapter 4

Numerical Implementation

The numerical model of heat, mass and momentum transport in an AEM fuel cell presented in Chapter 3 consists of 12 governing equations. In addition to that, several variables and coefficients are necessary to describe important phenomena such as phase change, sorption and adsorption, back diffusion, electrochemical reaction and many others. Therefore, the high complexity of the physics that govern the different phenomena inside the fuel cell results in a highly non-linear set of equations. In order to compute the aforementioned model, it is necessary to discretise the domain and employ the methodologies of Computational Fluid Dynamics.

4.1 Numerical modelling

According to Patankar [68], in order to obtain the numerical solution of a problem, its governing laws needs to be expressed mathematically. As an extension of the previous statement, Versteeg and Malalasekera [85] divided in three the stages needed by a CFD software to solve a numerical problem: pre-processing, processing and post-processing.

At the pre-processing stage, the geometry of interest, in other words, the computational domain is defined. This task is proceeded by the spatial discretisation, on which the domain is replaced by a grid sized in a way the cell dimensions do no significantly affect the simulation results (further explanation of grid independence is presented later in this chapter). At this stage the boundary conditions

necessary to solve the system of equations are specified.

The processing stage is the one where the flux of each variable is expressed through simple expressions. These equations are substituted in the governing equations. In order to solve this collection of equations, different methods can be used, such as the Finite Element Method (FEM), Finite Volume Method (FVM) and, Finite Difference Method (FDM). Due to its easier comprehension and also by the fact that the terms used in the equations present a physical meaning, the FVM is used in this thesis. In this approach, the integral form of the conservation equation is applied to all the finite control volumes (CV) in the domain.

The last stage of the procedure is to post process the data obtained from the numerical simulation. In this step, the analysis of the variables is carried out and the scalars and vector fields are integrated based on the focus of this analysis.

4.2 Numerical procedure

In order to solve the system of governing equations presented in Chapter 3, the finite volume based software FLUENT is used. The standard conservation equations of mass, momentum and energy are already present in discretised form in FLUENT. Nevertheless, it is necessary to implement the electronic charge, ionic charge, liquid water and, membrane water content conservation equations. To achieve this task, user defined functions (UDF) were used. As the transport equation of a generic scalar is a standard one, the implementation of the four additional equations consists of define the specific properties and constants necessary to solve them and to integrate it to the software. This stage also includes the specification of initial conditions, boundary conditions and source terms.

A pressure-based solver is used for all the simulations carried out in this thesis. Figure 4.1 presents the solution procedure for the solver. To satisfy the continuity equation, the velocity field has to be corrected by the pressure correction. This correction is done by using the well-known SIMPLE algorithm [68].

As to the governing equations, they have to be discretised so they can be solved. The following equation presents the steady state conservation equation

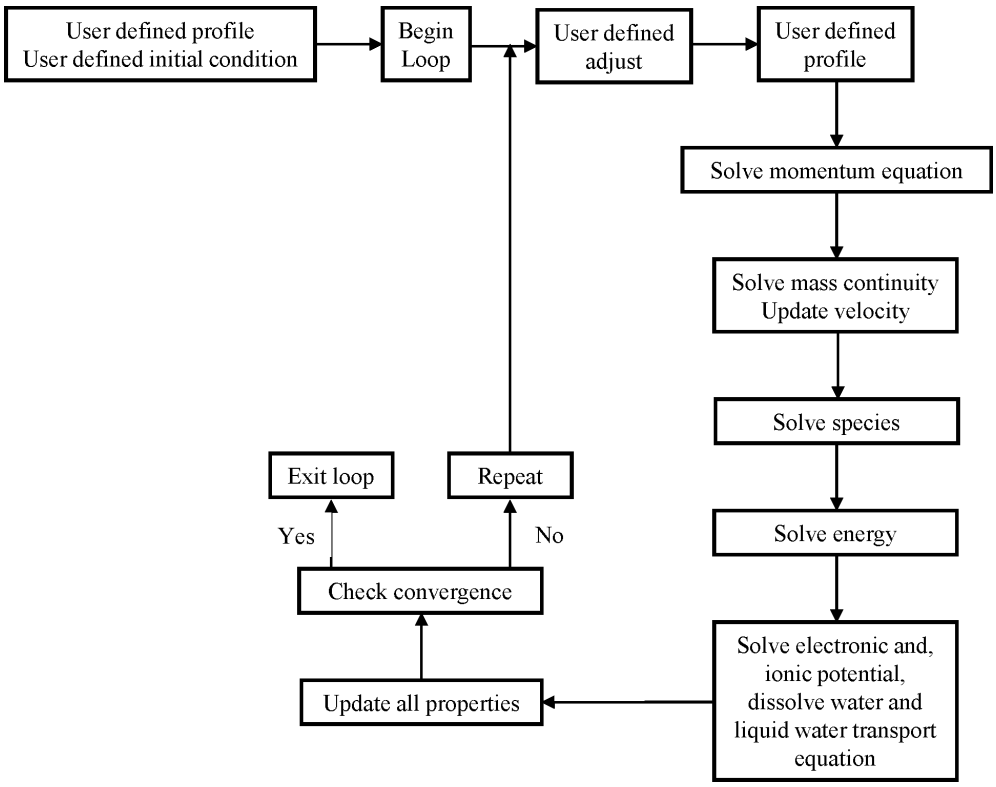

Figure 4.1: Overview of the solver.

for a general primitive variable scalar Ψ [68]

$$\nabla\cdot(\rho\Psi\vec{u}) = \nabla\cdot(D\nabla\Psi) + S_\Psi. \tag{4.1}$$

By integrating it over the CV and applying the Gauss divergence theorem, we obtain

$$\int_A \vec{n}\cdot(\rho\Psi\vec{u})\,dA = \int_A \vec{n}\cdot(D\nabla\Psi)\,dA + \int_{CV} S_\Psi dV, \tag{4.2}$$

where $\vec{n}$ is the unity vector normal to the volume control surface. The Figure 4.2 shows a bi-dimensional representation of the CV. At the centre of each CV one node is located and this node is used to compute the variables through the Equation (4.2). The Equation (4.2) can be rewritten as:

$$\sum_f^{N_f} \vec{n_f}\cdot(\rho_f\Psi_f\vec{u}_f A_f) = \sum_f^{N_f} \vec{n_f}\cdot(D\nabla\Psi_f A_f) + S_\Psi V, \tag{4.3}$$

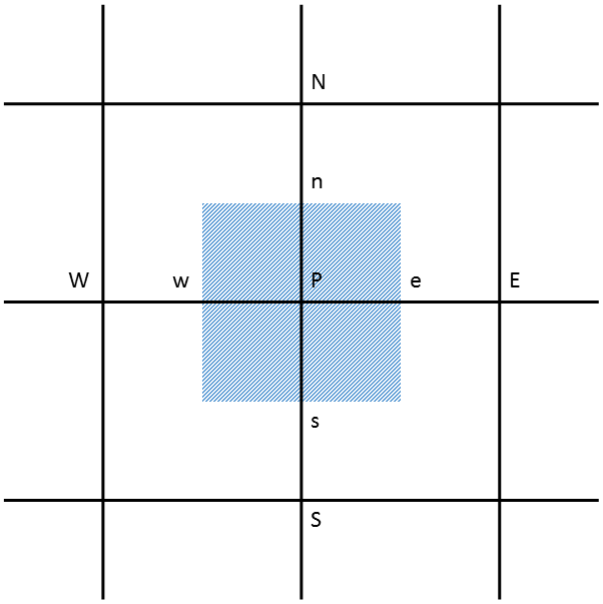

Figure 4.2: Bi dimensional control volume representation (hatch region).

where N_f is the number of faces of the CV, Ψ_f is the value of the scalar obtained at the face f, $\vec{u}_f$ is the velocity vector field at the face f, A_f is the area of the face f and $\vec{n}_f$ is the unity vector normal to the face f. The Equation (4.3) presents the value of Ψ for the node located in the central region of the CV and also of the nodes in the surroundings of the central node. One linear form of representation of the central node value is [68]

$$a_p \Psi_p = \sum_{nb} a_{nb} \Psi_{nb} + b \tag{4.4}$$

where a_p is the coefficient located at the centre of the CV, a_{nb} is the coefficient of the neighbour cells and b is the source term.

In order to solve the algebraic system of equations, several iterative methods can be used, including, but not limited to, TDMA (TriDiagonal-Matrix Algorithm), Jacobi method and, Gauss-Seidel. In this thesis, the implicit Gauss-Seidel method was utilised.

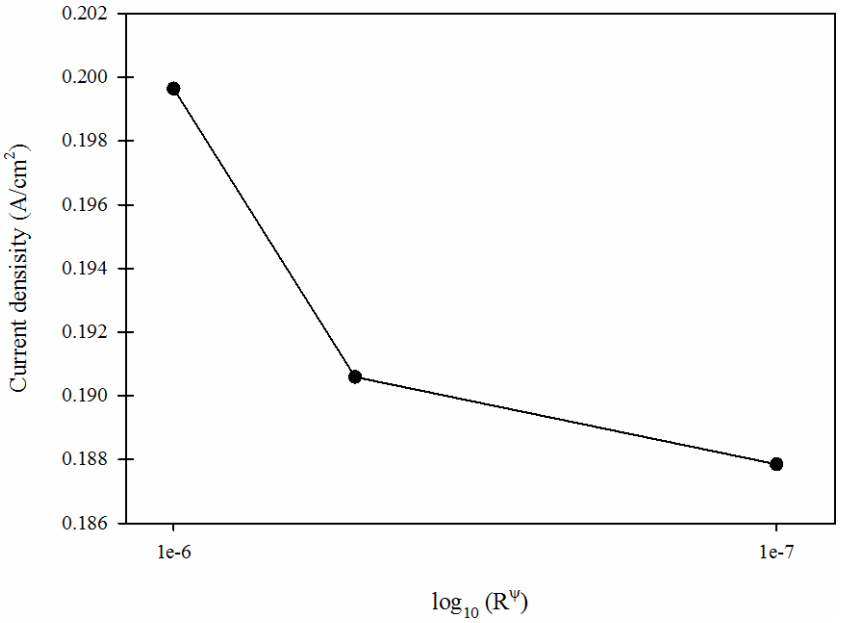

Figure 4.3: Effect of convergence criteria on the average current density.

4.3 Convergence Criteria

The last step of the solution procedure is to assess whether the convergence criteria is achieved or not (see Figure 4.2). To do so, the residual of all conservation equations must be compared to the established convergence criterion until it reaches value bellow. The Equation 4.5 defines the residual as

$$R^{\Psi} = \frac{\sum_{cells} \left| \sum_{nb} a_{nb} \Psi_{nb} + b - a_p \Psi_p \right|}{\sum_{cells} \left| a_p \Psi_p \right|} \tag{4.5}$$

where Ψ is the analysed variable. In the present analysis, $\log_{10}\left(R^{\Psi}\right) = 5 \times 10^{-7}$ is taken as the convergence criterion, which may lead to a maximum uncertainty of 1.5% in terms of current density, as shown in Figure 4.3.

4.4 Grid Independence

The quality of the discretisation of the computational domain into cells has significant influence on the numerical results. Even though a coarse mesh generally decreases the computational expense in comparison to a finer mesh, it is necessary

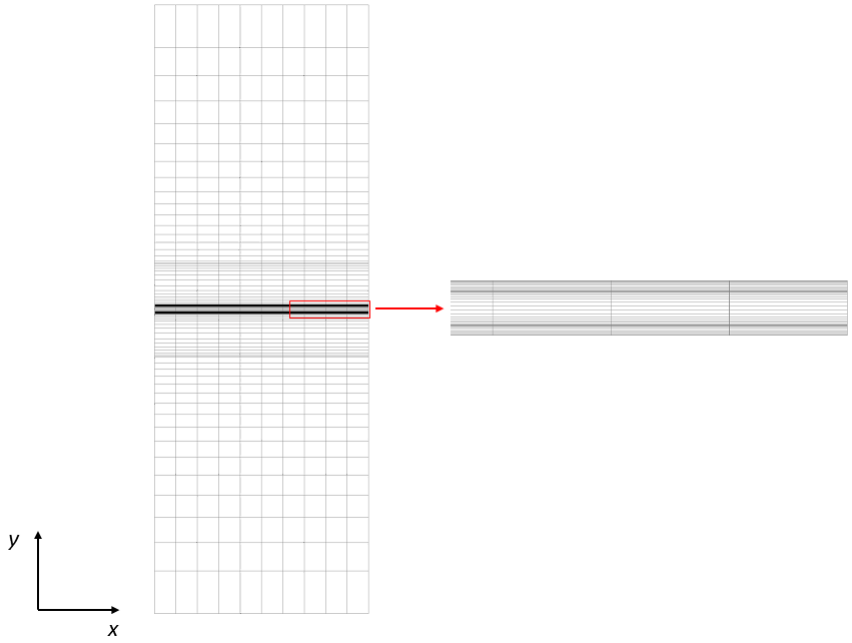

Figure 4.4: Grid scheme for a single channel.

to ensure that the computational discretisation does not affect the final solution. Nevertheless, it is worth mentioning that even though a finer mesh generally results in a more accurate solution, it does significantly increase the computational cost and time. Hence, a desirable mesh consists of a mesh with a minimum number of volumes whose influence on the final result is within a desirable error. Thus, in order to obtain a mesh with such characteristics, a grid independence analysis is performed. To do so, the number of grid points in each direction is specified and then varied in order to compute the uncertainty associated with the grid size. As initial guess, the number of volumes of each component of the fuel cell (i.e. BP, CL, GDL, membrane) in the x, y and z directions are $N^x = 8$, $N^y = 10$ and, $N^z = 80$, respectively. Nevertheless, one single layer of cells is added to the top and bottom of the bipolar plate, in order to cover the flow channel. Even though this layer of cells present variation in the number of cells in the y direction ($N^y = 1$), the number of cells in the x and z direction are varied as necessary. Figure 4.4 shows the grid scheme used to construct this mesh with the respective domains.

In order to evaluate the uncertainty associated with the discretisation of the computational domain, the following equation was used to compute the error in

the direction of interest:

$$Err = \left| \frac{\Psi_{N^{max}} - \Psi_N}{\Psi_{N^{max}}} \right| \times 100\% \tag{4.6}$$

where $\Psi_{N^{max}}$ and Ψ_N stand for the variable of comparison for the maximum number of cell and the current one, respectively. The maximum number of cells, N^{max}, for x, y and z direction is 15, 25 and 140, respectively.

In order to obtain the total error associated with the mesh, the following equation was used:

$$Total\ Error = \sqrt{(Err^x)^2 + (Err^y)^2 + (Err^z)^2} \tag{4.7}$$

Table 4.1 and Table 4.2 present the outcomes of grid convergence analysis for the macro-homogeneous and agglomerate models, respectively, where N^x , N^y and N^z are the number of grid points in the x, y and z directions and Err^x, Err^y and Err^z are the associated errors with respect of the variation of the number of grid points in x, y and z directions, respectively.

As one can see from Table 4.1 and Table 4.2, the mesh density in x and z directions do not significantly affect the computational results, whereas the error associated with number of volumes in the y direction is sensitive to the mesh density in this direction. With a total uncertainty of 4.49% and 2.82% for the macro-homogeneous and agglomerate model, respectively, M5 has been considered for both numerical models for the purpose of computational economy. The non-dimensional minimum cell distance (i.e. $\Phi = \Delta_{min,cell}/L$ where L is the largest dimension in the direction in question) and the grid expansion ratio (r) values of the M5 mesh is presented in Table 4.3.

Table 4.1: Mesh independence e Effect of N_x, N_y and N_z on the error of the average current density.

	N^x	N^y	N^z		N^x	N^y	N^z		N^x	N^y	N^z
M1	8			M4		10		M7			80
M2	10	10	100	M5	10	15	100	M8	10	10	100
M3	12			M6		20		M9			120
	$Err^x(\%)$				$Err^y(\%)$				$Err^z(\%)$		
M1	2.37			M4	6.85			M7	3.79		
M2	1.29			M5	3.94			M8	1.74		
M3	1.13			M6	1.24			M9	0.93		

Table 4.2: Mesh independence e Effect of N_x, N_y and N_z on the error of the average current density.

	N^x	N^y	N^z		N^x	N^y	N^z		N^x	N^y	N^z
M1	8			M4		10		M7			80
M2	10	10	100	M5	10	15	100	M8	10	10	100
M3	12			M6		20		M9			120
	$Err^x(\%)$				$Err^y(\%)$				$Err^z(\%)$		
M1	2.12			M4	5.11			M7	3.21		
M2	1.39			M5	2.14			M8	1.22		
M3	1.24			M6	1.74			M9	0.97		

Table 4.3: Non-dimensional minimum cell distance (Φ_x) and grid expansion ratio (r_x) values for the M5 mesh.

	Φ_x	Φ_y	Φ_z	r_x	r_y	r_z
Bipolar plate		2.643×10^{-5}				
Flow channel		2.643×10^{-5}				
Gas diffusion layer	0.1	5.286×10^{-6}	0.01	1.0	1.211	1
Catalyst layer		2.643×10^{-7}				
Membrane		7.400×10^{-7}				

4.5 Summary

The discretised computational domain plays an extremely important role in the process of solving numerical models. Misleading results and divergence are examples of the problems caused by an inadequate low quality mesh. It is also useful to verify the convergence criteria due the fact it can also affect the simulation outcome.

The optimisation of the grid and the convergence criteria were necessary to avoid the waste of computational power. To do so, different cases were analysed and compared to obtain the mesh with less volumes and ensure that results were not significantly affected. In addition to that, a convergence criterion sufficiently strict was used to reach steady-state solutions.

Chapter 5

Results and Discussion - Macro-homogeneous model

In this chapter, the macro-homogeneous model presented in Chapter 3 is used to assess the influence of the flow direction in the flow channels on the overall fuel cell performance. Here, the co-flow configuration refers to the condition when the flows in the channels on both anode and cathode sides are in the same direction. By contrast, the flow direction in the channel on the cathode side is opposite to the channel on the anode side in the counter-flow configuration. A schematic representation of the different configurations is presented in Figure 5.1. Moreover, the effects of the inlet temperature and the humidification of the gaseous mixture at the channel inlets for AEM fuel cells have also been analysed. The operating parameters and the electrochemical kinetics parameters used in this study were taken from published literature and are presented in the Table 5.1 [42] and Table 5.2 [57], respectively.

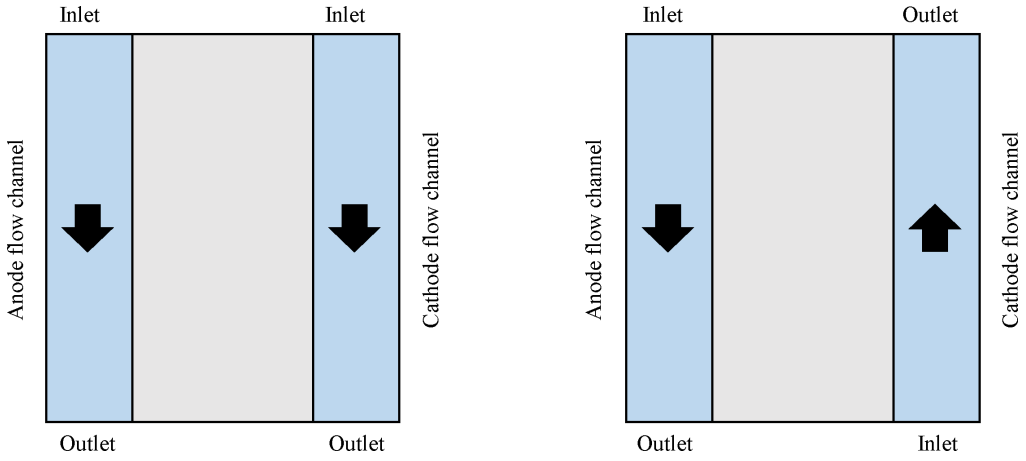

Figure 5.1: Flow configuration: co-flow and counter-flow.

Table 5.1: List of operating parameters. Bold values represent the base case and were used for the numerical validation purpose.

Parameter	Value
Cell voltage, $\phi_{cell}(V)$	0.3, 0.4, **0.5**, 0.6, 0.7, 0.8, 0.9, 1.0
Inlet temperature, $T_0\,(K)$	313.15, 318.15, **323.15**, 328.15, 333.15
Relativity humidity at anode, $RH_a\,(\%)$	**100**, 90, 80, 70, 50
Relativity humidity at cathode, $RH_c\,(\%)$	**100**, 90, 80, 70, 50
Stoichiometry ratio at anode, ξ_a	2.0
Stoichiometry ratio at cathode, ξ_c	3.0

Table 5.2: Electrochemical kinetic parameters.

Parameter	Anode	Cathode	Unity
Reference exchange current density, j_0^{ref}	162	2×10^8	A/m^3
Reference hydrogen concentration, C_{H2}^{ref}	0.0564	-	$kmol/m^3$
Reference oxygen concentration, C_{O2}^{ref}	-	0.00339	$kmol/m^3$
Transfer coefficient, α	0.5	0.5	-
Reaction order, β	0.5	1.0	-

5.1 Model validation

The numerical macro-homogeneous model is validated by comparing the polarisation curve (i.e. variation of voltage with current density) obtained from numerical simulations with experimental findings [51], as shown in the Figure 5.2, which reveals that a good agreement has been achieved between numerical and experimental findings. However, some parameters (e.g. kinetic parameters, porosity, and intrinsic permeability) were not specified in Kruusenberg et al. [51] and typical values for these quantities (see Table 3.9) are chosen for numerical simulations and no special attempt is made to tune the values of these quantities to match the polarisation curve with experimental findings. The level of qualitative agreement between numerical and experimental results is consistent with several previous analyses [52, 91]. Nevertheless, in order to investigate the capacity of the numerical model to fit the experimental data, additional simulations were carried out considering all parameters the same except the porosity of the GDL, which was considered as $\epsilon_{GDL} = 0.4$ [69] in comparison to $\epsilon_{GDL} = 0.6$ listed in Table 3.9. It can be seen from Figure 5.2 that by only changing the porosity of the GDL, the polarisation curve approaches the experimental results, demonstrating that the numerical results can fit the experimental data by tuning the parameters, which

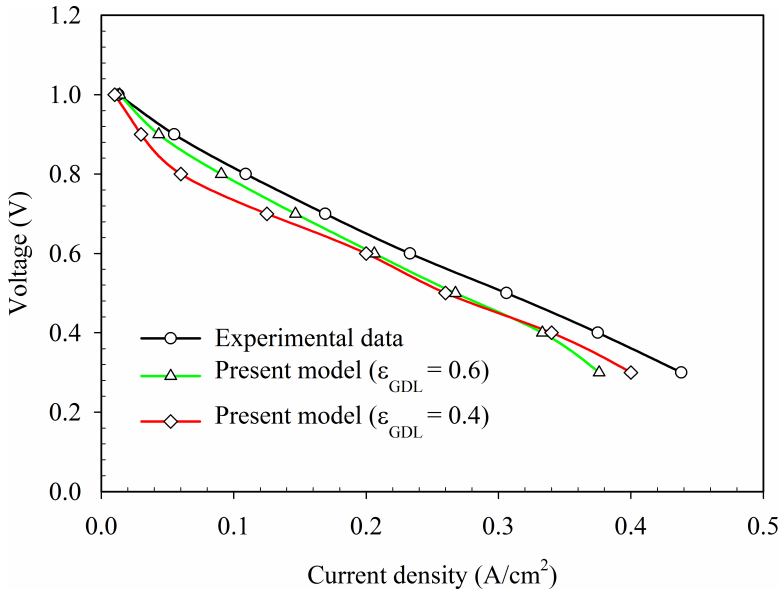

Figure 5.2: Model validation: polarisation curves comparison. The experimental values were obtained from Kruusenberg et al. [51].

are not specified in Kruusenberg et al. [51]. The results shown in the current chapter corresponds to the physical properties and parameters listed in Table 3.9 because the qualitative nature of the results do not change as a result of changing ϵ_{GDL} from 0.6 to 0.4.

5.2 Effect of flow direction

In order to investigate the effect of the flow direction on the fuel cell performance, three different temperature values have been considered for both co-flow and counter-flow configurations. The variation of voltage with current density for both co-flow and counter-flow configurations are shown in Figure 5.3, which shows that for the set of parameters used, the flow direction in the channels does not has a major influence on the overall performance of the fuel cell because the supply of reactant species to the catalyst layer for these conditions operating conditions not affected by the flow direction. Results have demonstrated no more than 4% variation on the current density produced as consequence of different flow configuration. In addition to the simulations carried out considering

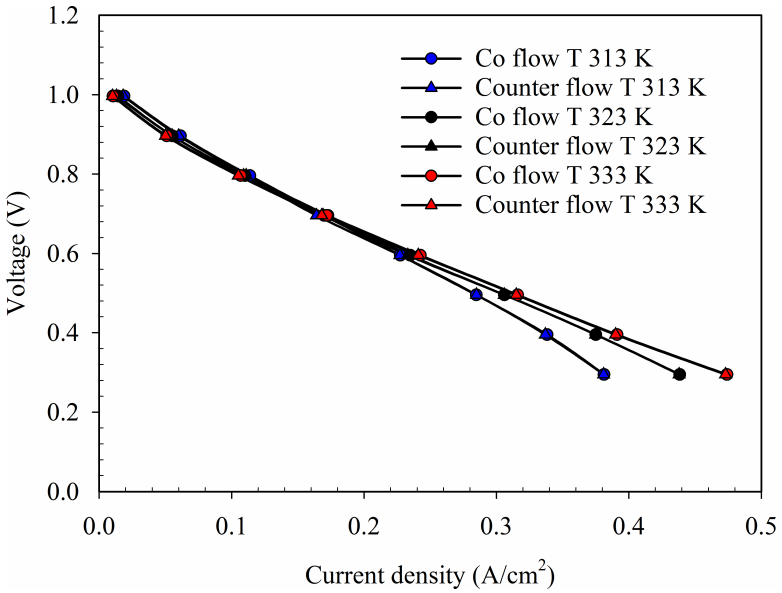

Figure 5.3: Co flow and counter flow polarisation curve comparison. Operating parameters: $\phi_{cell} = 0.3 - 1.0V$, $RH_a = 100\%$, $RH_c = 100\%$, $\xi_a = 2.0$, $\xi_c = 3.0$.

the base case inlet temperature (323.15 K), numerical simulation has been performed considering two different inlet temperature, as shown in Table 5.1. As one can see in Figure 5.3, irrespective of the variation of the inlet temperature, no significant variation of the current density is observed when comparing the overall performance of the AEM fuel cell for a co-flow and counter-flow configuration.Nevertheless, it has been found that the gradient of water vapour molar concentration is slightly higher in the counter-flow configuration at the cathode side, mainly due to the slightly higher drag of liquid water from the anode side, which is consistent with previous findings [62].

In order to emphasise the species gradient due to the electrochemical reaction, a three-dimensional contours of the species concentration for the co-flow configuration for a 0.3 V cell voltage are presented in Figure 5.4. The hydrogen and oxygen consumption due to the HOR and ORR, respectively, causes a depletion of their molar concentration towards the outlet. Due to the larger molecular size and slower diffusion of the oxygen in comparison to the hydrogen, a more clear gradient of the oxygen molar concentration is observed, specially when comparing the region under the flow channel and bipolar plate. With respect of the water species, the augmentation of the concentration at the anode side is result of the

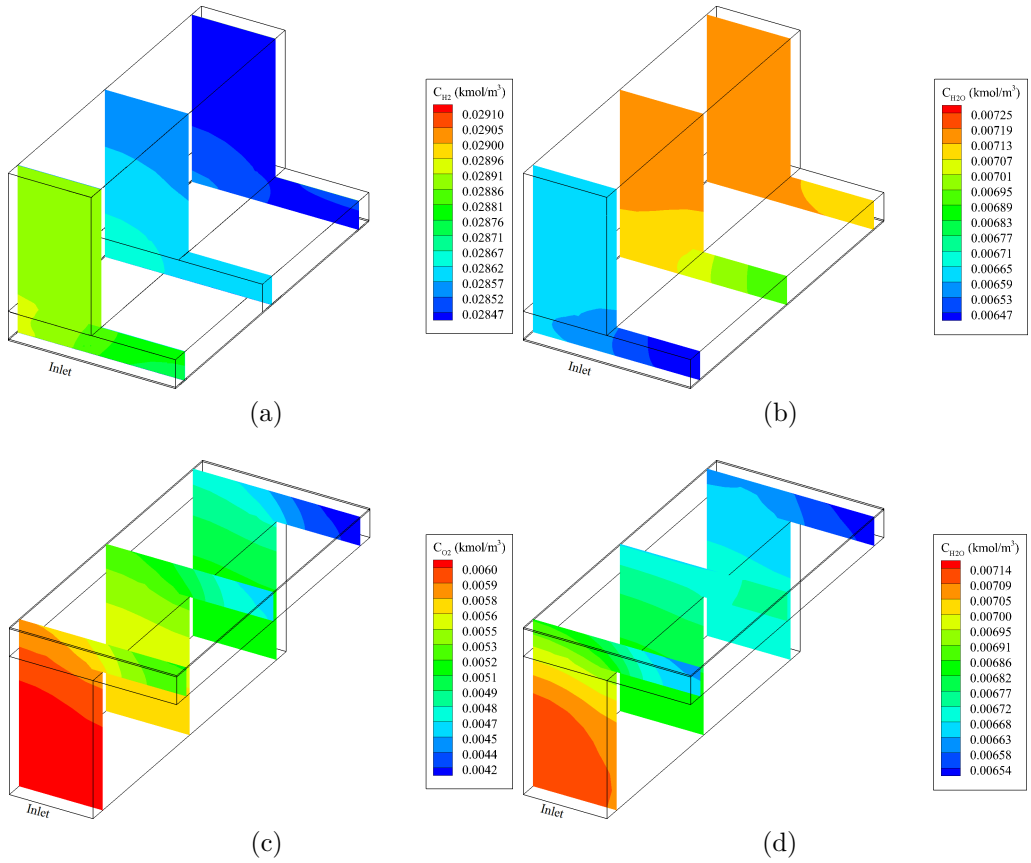

Figure 5.4: Molar concentration: a) H_2, b) H_2O (anode), c) O_2, d) H_2O (cathode). Operating parameters: $\phi_{cell} = 0.3V$, $T_0 = 333.15K$, $RH_a = 100\%$, $RH_c = 100\%$, $\xi_a = 2.0$, $\xi_c = 3.0$.

electrochemical reaction taking place at the catalyst layer. On the other side, the depletion of the water concentration is consequence of the consumption necessary to the formation of the hydroxyl ion.

5.3 Effect of inlet temperature

As the flow direction does not have a major influence on the overall fuel cell performance, the influence of inlet temperature (which is the temperature the mixture is supplied) on the fuel cell performance has been analysed for the counter-flow configuration. Figure 5.5 shows that an increase in the inlet temperature

increases the mean current density for a given output voltage. For instance, for the 0.4 V cell voltage case, the overall performance of the fuel cell has increase from 0.375 A/cm^2 to 0.390 A/cm^2 for the 323.15 K and 333.15 K inlet temperature cases, respectfully. An increase in temperature improves the electrochemical kinetics according to Equations (3.53) and (3.54).

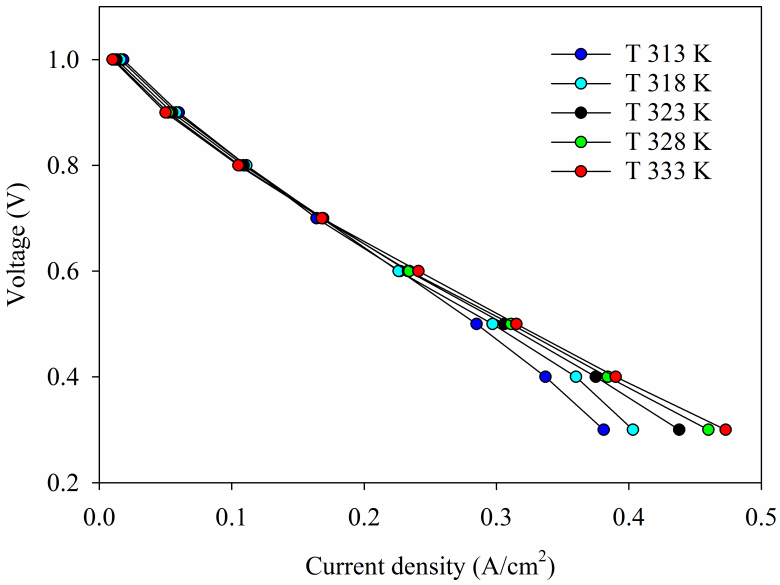

Figure 5.5: Effect of inlet temperature on the fuel cell performance. Operating parameters: $\phi_{cell} = 0.3 - 1.0V$, $RH_a = 100\%$, $RH_c = 100\%$, $\xi_a = 2.0$, $\xi_c = 3.0$.

The hydration of the membrane play an important role in the fuel cell performance. Figure 5.6 demonstrates that the membrane water content increases with increasing temperature, which is in accordance with previous experimental findings [56]. Thus, the enhanced ion conductivity due to high water content in the membrane gives rise to a smaller Ohmic loss in the membrane. The product of the electrochemical reaction is water in the liquid phase in the anode catalyst layer. Figure 5.6 shows that the volume fraction of liquid water decreases as the temperature increases. Although the liquid water production increases for higher temperatures, this production is superseded by high evaporation rate at high temperature values due to the fact that the saturation pressure in the catalyst and gas diffusion layers are higher than the water vapour pressure. Furthermore, the combination of high relative humidity at the anode side and the water production in the liquid phase are responsible for the back diffusion process which drags

liquid water from the anode to the cathode side in the dissolved phase. This, in turn, contributes to the decrease of the liquid water fraction in the anode side and also enhances the hydration of the membrane and catalyst layer in the cathode side.

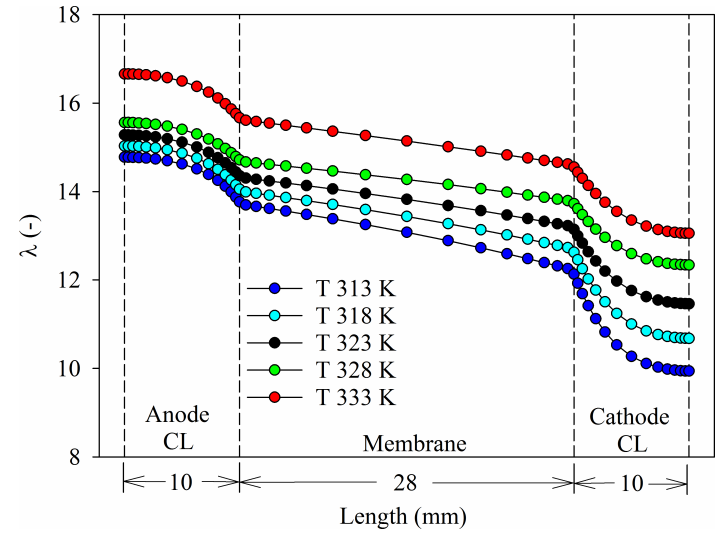

(a)

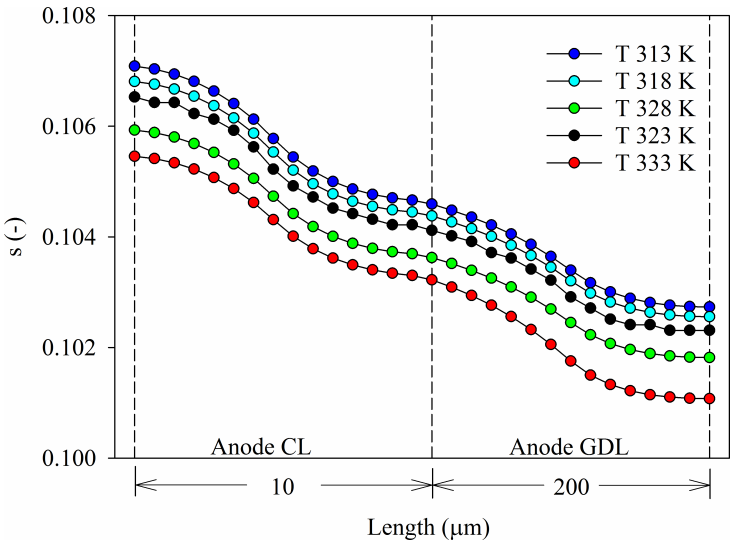

(b)

Figure 5.6: Effect of inlet temperature on: a) membrane water content b) liquid water fraction. Operating parameters: $\phi_{cell} = 0.5V$, $T_0 = 323.15K$, $RH_a = 100\%$, $RH_c = 100\%$, $\xi_a = 2.0$, $\xi_c = 3.0$.

5.4 Effect of inlet humidification

Figure 5.7 shows that the relative humidity of the supplied mixture at the inlets has a significant influence on the fuel cell performance. The water demand for OH^- formation is directly related to the elevation of the Butler-Volmer reaction rate (Equations (3.53) and (3.54)). Thus, the relative humidity has a higher impact in the lower output voltages where the current density values are high. A decrease in relative humidity from 90% to 80% shows a more drastic loss of performance that is observed when the relative humidity is decreased from 100% to 90%. When comparing the overall performance of the 100% and 90% inlet relative humidity conditions, the performance dropped by up to 22% for the 0.3 V cell voltage case. The extent of dehydration of membrane is much greater when the relative humidity drops from 90% to 80% than the corresponding effect as a result of the relative humidity drop from 100% to 90%.

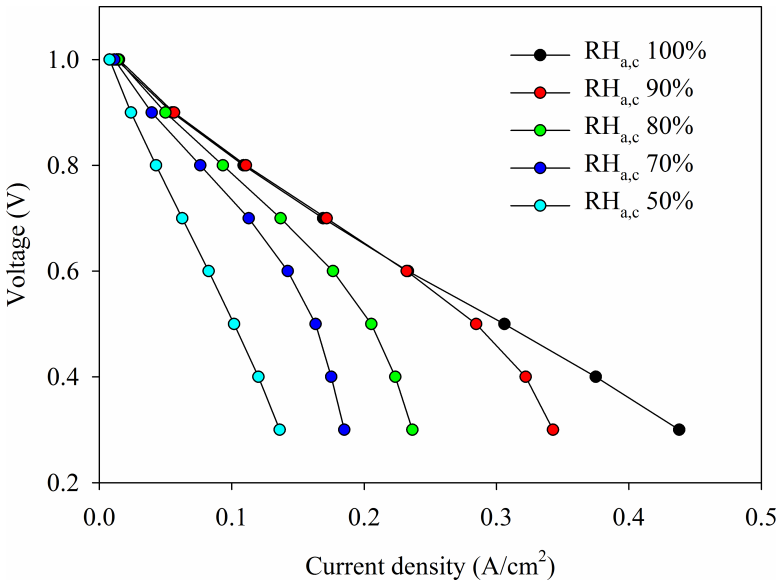

Figure 5.7: Effect of inlet relative humidity on the fuel cell performance. Operating parameters: $\phi_{cell} = 0.3 - 1.0V$, $T_0 = 323.15K$, $\xi_a = 2.0$, $\xi_c = 3.0$.

Since the sorption and desorption processes are governed by the gradient of water activity between the anode and cathode side, the hydration of the membrane is negatively affected by a reduction of relative humidity at the channel inlets, which gives rise to higher ionic resistivity (i.e. higher Ohmic loss) leading

to a smaller value of current density than better hydrated cases. Therefore, the membrane water content reduces with the weakening of water transfer within the membrane, which can be substantiated from Figure 5.8. Regarding the liquid water phase, as presented in Figure 5.8, the liquid water fraction is higher for the better humidified case. The main reason for the reduction of the liquid water fraction within the catalyst and gas diffusion layers is the fact that the lower relative humidity enhances the evaporation processes (i.e. water vapour partial pressure lower than the saturated pressure). In addition to that, as the overall performance of the fuel cell is compromised by a less hydrated membrane state, the water produced due to the electrochemical reaction is partially dragged from the anode catalyst layer to the membrane in order to compensate the dehydrated condition caused by the decrease in the relative humidity at the flow channel inlet. Moreover, the relative humidity has also an impact in the thermal transport within the layers. A larger gradient of molar water concentration across the layers (vertical mid-plane) is observed for the values of smaller relative humidity, resulting in the extraction of more latent heat from the surface. Heat generation within the fuel cell due to the HOR, which in turn affects the local current density due to its temperature dependence. Therefore, the equilibrium between temperature and reaction rate is altered and a negative feedback between temperature and current density is obtained as shown in Figure 5.9. Thus, when combining the smaller heat generation due to the smaller current density and the extraction of latent heat from the surface, the temperature for lower relative humidity is observed to be smaller than the higher relative humidity cases, as shown in Figure 5.9.

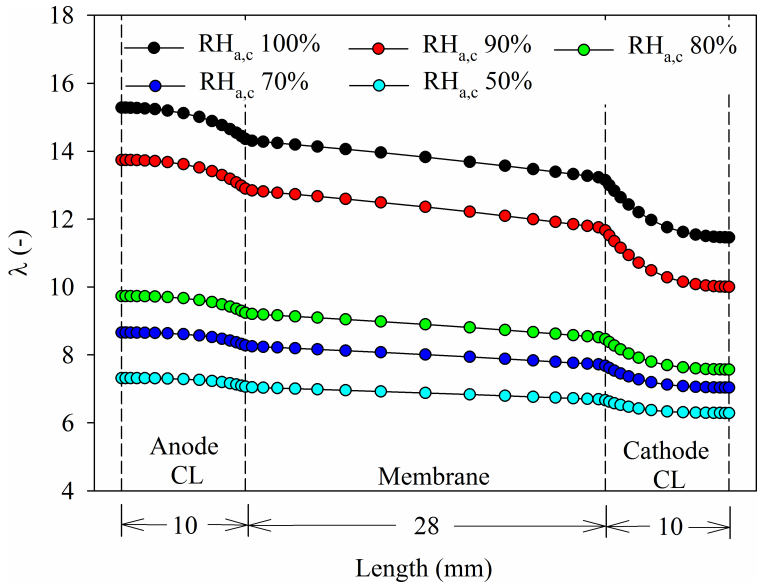

(a)

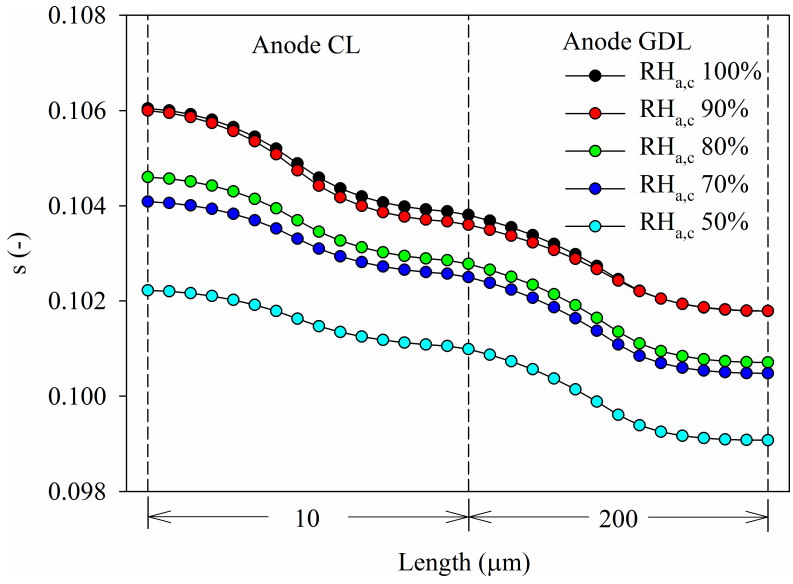

(b)

Figure 5.8: Effect of inlet relative humidity on: a) membrane water content b) liquid water fraction. Operating parameters: $\phi_{cell} = 0.5V$, $T_0 = 323.15K$, $\xi_a = 2.0$, $\xi_c = 3.0$.

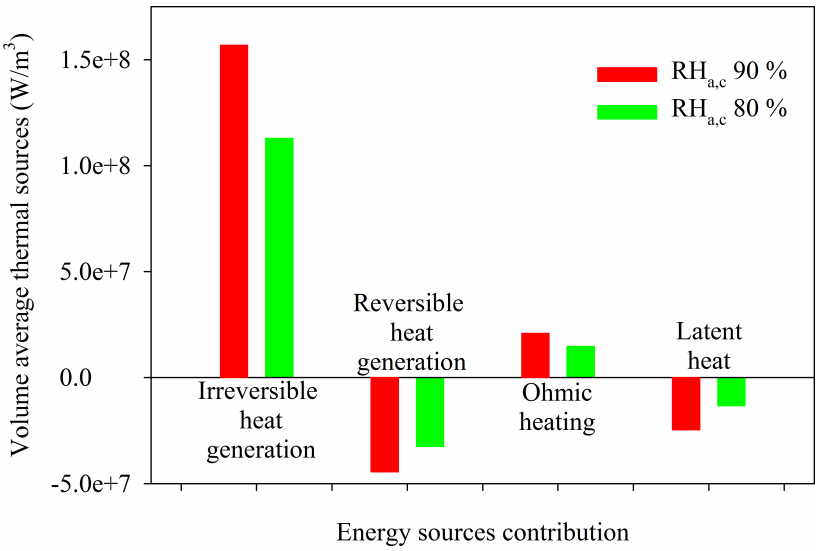

(a)

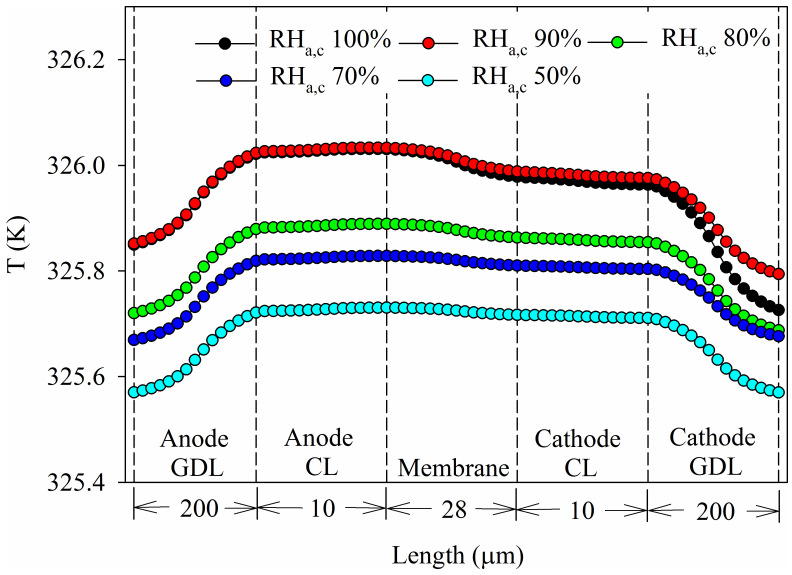

(b)

Figure 5.9: a) Energy source term contribution for different relative humidity cases b) Effect of relative humidity on the temperature. Operating parameters: $\phi_{cell} = 0.5V$, $T_0 = 323.15K$, $RH_a = 100\%$, $RH_c = 100\%$, $\xi_a = 2.0$, $\xi_c = 3.0$.

5.5 Summary

In this chapter, a three-dimensional macro-homogeneous numerical model has been used to analyse the influences of the flow mode, inlet temperature and relative humidity on a single channel anion exchange membrane fuel cell performance.

It has been observed that the overall performance of the AEM fuel cell has not been significantly affected by the flow direction in the channels, having a variance of the overall performance of the fuel cell within a 4% range for the base case. Similar results have been observed by Ge et al. [28] when performing similar analyses in PEMFC. Both flow modes were compared for different inlet temperatures and no major effect on the overall performance of the fuel cell was observed.

However, the overall performance of the AEM fuel cell has been found to be significantly affected by the inlet temperature and relative humidity. An increase in inlet temperature has a positive influence on the overall performance of the fuel cell due to the enhancement of the electrochemical kinetics and also because of the better hydration condition of the membrane. An augmentation (between 3 and 8%) of the overall performance of the fuel cell has been observed when comparing the current densities at 323.15 K and 333.15 K inlet temperatures for the range of operation of an ordinary AEM fuel cell (0.3 to 0.6 V cell voltage). The deterioration of the overall performance when comparing the base case to lower temperatures (i.e. 313.15 K) can be as high as 13%.

With respect of the relative humidity, when decreased, adversely affects the performance of the fuel cell, mainly due to the high resistance offered to the ions to diffuse in a poor hydration membrane environment. The effect of the increase of ions diffusion resistance (i.e increase of Ohmic loss) can be observed on the polarisation curve for the $RH_{a,c} = 50\%$ case, where passed the activation loss region, reflects in a sharp drop of the overall performance of the AEM fuel cell. Moreover, the lower relative humidity cases exhibit lower local temperatures, which also contribute to the reduction of the average current density produced in the fuel cell. On the other side of the spectrum, for the operating conditions analysed in this thesis, the fuel cell operation under higher relative humidity conditions (90 - 100%) provided a better hydration of the membrane, resulting in lower Ohmic resistance. Nevertheless, it is worth mentioning that the even though

the higher relative humidity at the anode side is beneficial to the membrane hydration due to back diffusion, the formation of liquid water has to be balanced in a way such that clogging of the pores in the ACL and anode GDL does not give rise to the concentration loss.

Chapter 6

Results and Discussion - Part I: Agglomerate model

In the previous chapter numerical simulations have been performed in other to address the influence of the flow mode and the operating conditions of a generic AEM fuel cell. Despite the good qualitative agreement with experimental results, the macro-homogeneous model is limited to a single length scale (i.e. CL thickness), lacking of capacity to accurately account for the transportation of species and charge in the CL. Hence, a three-dimensional agglomerate model for a multiphase flow for a typical AEM fuel cell has been developed to describe the different length scales present in the CL and it has been used to analyse the effect of species transport within the CLs. The operating parameters used to perform these simulations are presented in Table 6.1. A detailed analysis of the influences of species transport on the overall fuel cell performance is provided in the next subsections.

6.1 Model validation

Due to the wide range of operating parameters, structural composition of the fuel cell components and the lack of information regarding some of the transportation characteristics related to the membrane Tokuyama A201, a direct comparison with a single experimental dataset might not be sufficient. Therefore, the present

Table 6.1: List of operating parameters. Bold values represent the base case and were used for the numerical validation purpose.

Parameter	Value
Cell voltage, $\phi_{cell}(V)$	0.3-1.0
Inlet temperature, $T_0\,(K)$	323.15
Relativity humidity at anode, $RH_a\,(\%)$	100
Relativity humidity at cathode, $RH_c\,(\%)$	100
Stoichiometry ratio at anode, ξ_a	2.0
Stoichiometry ratio at cathode, ξ_c	3.0

numerical model is validated by comparing the polarisation curve produced with the experimental results from different authors [51, 53, 73]. As one can see in Figure 6.1, the proposed agglomerate model shows a good qualitative agreement with the different experimental results using the Tokuyama A201 membrane.

6.2 Overall performance

Generally, the performance of fuel cells is assessed by comparing polarisation curves. Thus, the overall performance of the AEM fuel cell for the current agglomerate model data is compared with the several experimental data as well as with the previously developed macro-homogeneous model [59], as shown in Figure 6.1. In order to compare between macro-homogeneous and agglomerate models, all the parameters are kept the same for both models (see Table 3.7 and Table 3.9). It can be seen from Figure 6.1 that both macro-homogeneous and agglomerate numerical models are capable of capturing the trend of the experimental results. As the macro-homogeneous model does not account for subtle

Table 6.2: Electrochemical kinetic parameters.

Parameter	Anode	Cathode	Unity
Reference exchange current density, j_0^{ref} [57, 59]	11.916	1×10^{-4}	A/m^2_{Pt}
Reference hydrogen concentration, C_{H2}^{ref} [57, 59]	0.0564	-	$kmol/m^3$
Reference oxygen concentration, C_{O2}^{ref} [57, 59]	-	0.00339	$kmol/m^3$
Platinum loading, m_{Pt} [80]	0.004	0.004	kg/m^2
Platinum mass ratio, f [80]	0.4	0.4	-
Radius of agglomerate, r_{agg} [80]	1×10^{-6}	1×10^{-6}	m
Effective specific agglomerate surface area, a_{agg}[80]	3.6×10^5	3.6×10^5	m^2/m^3
Thickness of ionomer coating, δ_M [80]	8×10^{-8}	8×10^{-8}	m
Transfer coefficient, α [74, 75]	0.5	0.5	-
Reaction order, β	0.5	1.0	-

transport characteristics and dependencies on catalyst layer composition, it overestimates the fuel cell performance in comparison to the agglomerate model. An overview of the losses of both agglomerate and macro-homogeneous model for 0.5 V output voltage is shown in Figure 6.2. It can be seen from Equation (3.55) that the overpotential is defined as the difference between electronic and ionic potential. No significant difference is observed in the values of electronic potentials between the agglomerate and macro-homogeneous models. Nevertheless, the ionic potential for the agglomerate model is observed to be smaller than the ionic potential for the macro-homogeneous model. This is directly associated with the hydration state of the membrane. As the reaction rate for the agglomerate is

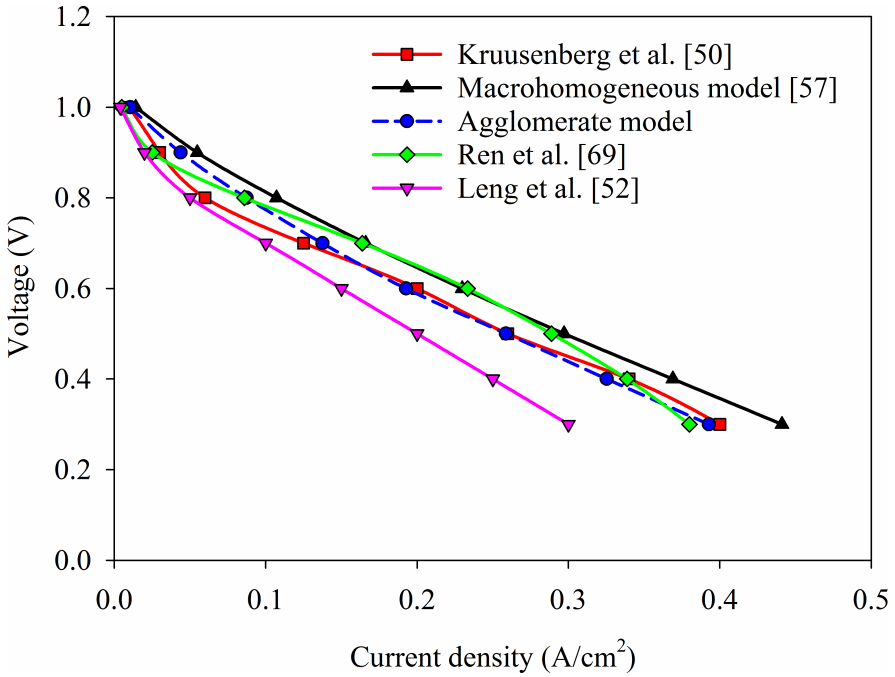

Figure 6.1: Polarisation curve for both agglomerate and macro-homogeneous [59] CL numerical models along with experimental data [51, 53, 73]. The parameters used for the agglomerate model were: $T_0 = 323.15K$, $RH_a = 100\%$, $RH_c = 100\%$, $\xi_a = 2.0$, $\xi_c = 3.0$.

smaller than the macro-homogeneous model, less water is produced as a product of the electrochemical reaction, which decreases the amount of water sorption in the interface of anode catalyst layer and membrane. Moreover, as the flux of ions from the anode to cathode side decreases, less water is dragged due to the ions transport, which supports the less hydrated state in the agglomerate model in comparison to the macro-homogeneous model. For the current analysis, about 70% of the losses are related to Ohmic losses as the ionic conductivity of the current membrane is over one order of magnitude lower in comparison with an ordinary Nafion membrane. The activation and concentration losses in the agglomerate model are responsible for the remaining 30%. Further explanation regarding the impact of the extra resistances due to the agglomerate model in the activation and concentration losses are provided in the following sub-sections.

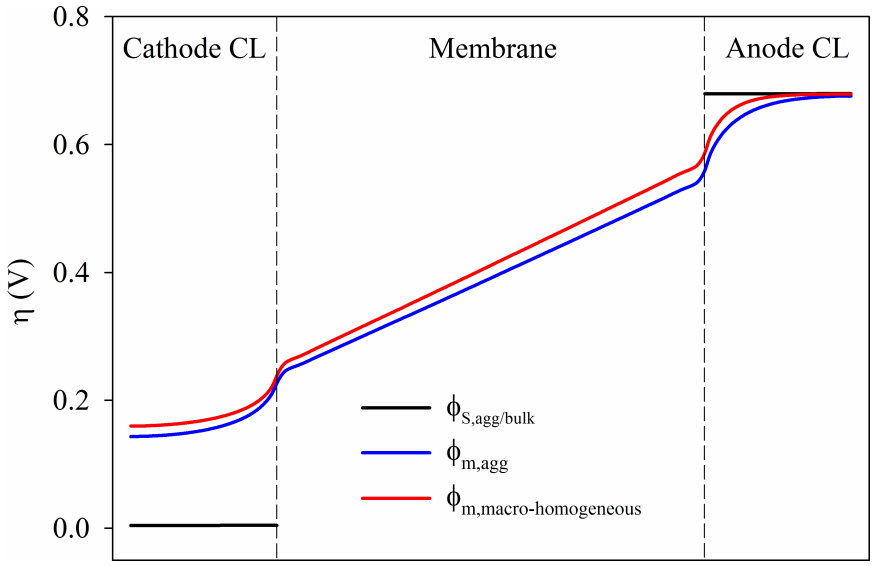

Figure 6.2: Total overpotential for both agglomerate and macro-homogeneous models. Operating parameters: $\phi_{cell} = 0.5V$, $T_0 = 323.15K$, $RH_a = 100\%$, $RH_c = 100\%$, $\xi_a = 2.0$, $\xi_c = 3.0$.

6.3 Concentration potential

Both macro-homogeneous and agglomerate models considered the momentum and mass conservation equations ((3.6) and (3.7), respectively) to partially govern the motion of species within the computational domain. In addition to the aforementioned equations, the macro-homogeneous model used the convective-diffusive, Equation(3.15), is used to describe the gas species conservation equation. Although the use of the Equation (3.15) in the macro-homogeneous model provides a qualitatively correct representation of the main species transportation in the fuel cell, further detailing of the species transportation and gaseous properties calculation were implemented in the agglomerate model. Hence, in the agglomerate model, the Equation (3.15) is replaced by the Maxwell-Stefan Equation (3.29) and the kinetic theory is used to compute species properties such as binary diffusion, dynamic viscosity and thermal conductivity. Furthermore, corrections were added to the electrochemical kinetics in order to account for all the different transport coefficients and dependencies on the catalyst layer composition.

As shown in Figure 3.2, the cathode and anode catalyst layers are considered

to be made up of spherical Pt/C agglomerate with void regions covered by the ionomer according to the agglomerate model. As the ionomer layer of 8×10^{-8} m thickness covers the spherical agglomerate, an extra resistance is added to the transport and thus the concentration loss is expected to increase. It can be seen from Figure 6.3 that the concentration loss profiles at the middle plane section at the cathode CL for the macro-homogeneous and agglomerate models are significantly different. As the partial pressure of oxygen diminishes near the catalyst/membrane interface, especially under the bipolar plate region, the rate of oxygen crossing the ionomer cover around the particle sphere decreases in the context of the agglomerate model. The starvation of oxygen in contact with the Pt/C agglomerate is responsible for the mass transfer associated losses, which reduces the overall performance of the fuel cell. From the combination of Equations (3.61) and (3.69), one can see that the ratio of reference and current molar concentration is impacting on the concentration loss. Nevertheless, the reference values of the catalyst layer used in this study were measured at higher pressure, thus, under the current operating conditions, the overpotential benefits from the ratio of reference and current molar concentration. Regarding the concentration loss on the anode side, the faster diffusion of the hydrogen in the ionomer compared to the oxygen results in a marginal change in the concentration loss between agglomerate and macro-homogeneous models and, thus will not be presented here for the sake of conciseness.

6.4 Activation potential

As the effect of the activation potential is pronounced higher cell voltage conditions, this aspect will be discussed for the 0.9 V output case. The contours of the activation loss in the cathode catalyst layer for both agglomerate and macro-homogeneous models are presented in Figure 6.4. It can be seen from Figure 6.4 that the contribution of the activation loss to the total overpotential in the cathode catalyst layer is bigger in the agglomerate model than in the macro-homogeneous model, which leads to an overestimation of the fuel cell performance by the macro-homogeneous model. This loss in the agglomerate model arises due

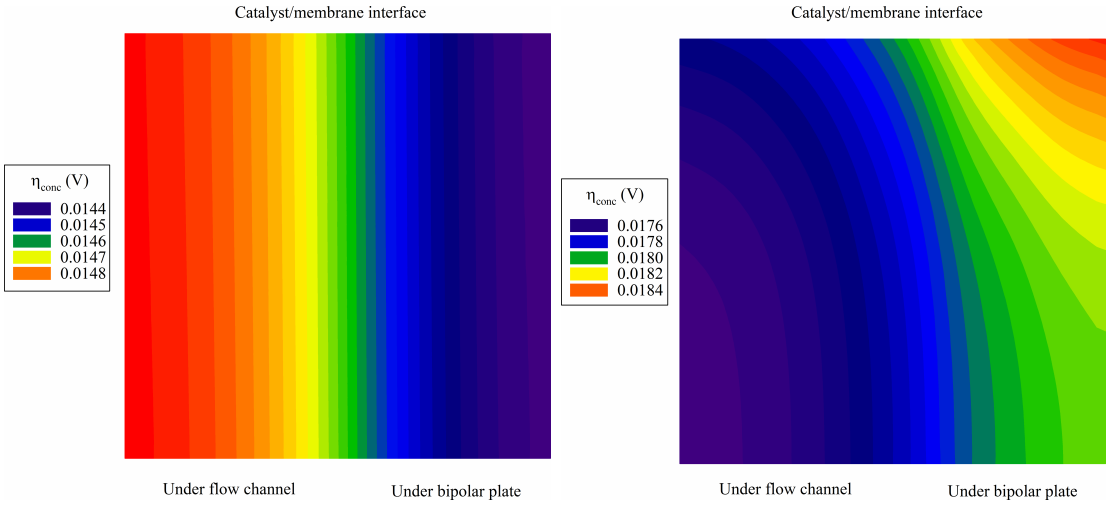

Figure 6.3: Concentration loss in the cathode CL: (a) macro-homogeneous model and (b) agglomerate model. Operating parameters: $\phi_{cell} = 0.5V$, $T_0 = 323.15K$, $RH_a = 100\%$, $RH_c = 100\%$, $\xi_a = 2.0$, $\xi_c = 3.0$.

to the usage of an effective specific platinum surface area per unit catalyst layer volume because the composition and physical dimensions of the catalyst layer have direct impact on the activation potential. From Equation (3.22) and (3.25), one can see that increasing the amount of Pt/C in the catalyst layer is beneficial to the activation potential. Nevertheless, the void volume fraction in the catalyst layer is directly affected by the increase of Pt/C, which also contributes to the starvation of the species in the reactive sites.

6.5 Effectiveness factor

The implementation of the agglomerate model introduces the effectiveness factor for the catalyst layer, which is expressed by Equation (3.64), and it quantifies the utilisation of the catalyst layer through the ratio of species diffusion in the ionomer and electrochemical reaction rate constant. Nevertheless, it is worth mentioning that the unity effectiveness factor does not mean a high reaction rate, but a more uniform reaction through the catalyst layer site. The effectiveness

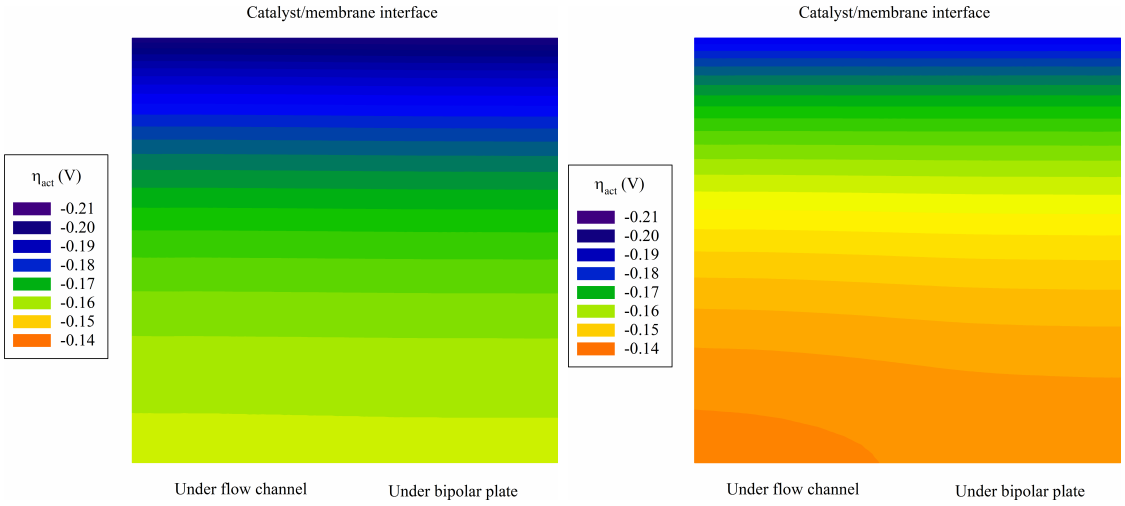

Figure 6.4: Activation loss in the cathode CL: (a) macro-homogeneous model and (b) agglomerate model. Operating parameters: $\phi_{cell} = 0.9V$, $T_0 = 323.15K$, $RH_a = 100\%$, $RH_c = 100\%$, $\xi_a = 2.0$, $\xi_c = 3.0$.

factor for the anode and cathode catalyst layers is presented in Figure 6.5. The effectiveness factor in the anode side does not vary significantly through the length of the catalyst layer, which implies that the utilisation of the catalyst layer at the anode side is mostly even. Nevertheless, despite the faster hydrogen diffusion, one can observe a drop, although not significantly, in the region closer to the membrane and catalyst layer interface. As seen in the previous section, the higher overpotential is located at the interface of membrane and catalyst layer. Thus, the higher demand for hydrogen and the slightly short supply of it causes the drop in the effectiveness factor. Nonetheless, on the cathode side, the effectiveness factor shows a significant drop as the membrane interface is approached. Here several factors need to be taken into consideration for explaining this drop. The diffusion of oxygen is slower than hydrogen diffusion. As the air is supplied with humidified state, oxygen has to compete with water molecules to diffuse through the pores of the catalyst layer. This resistance causes the lack of oxygen near the interface of the catalyst layer with the membrane, which further reduces the utilisation of the catalyst in that area. Another important aspect is that the reaction rate variation through the length of the catalyst layer. For the case analysed here, a

wide range of overpotential is observed, which results in a considerable variation of the reaction rate. Therefore, the utilisation of the catalyst layer on the cathode side is compromised.

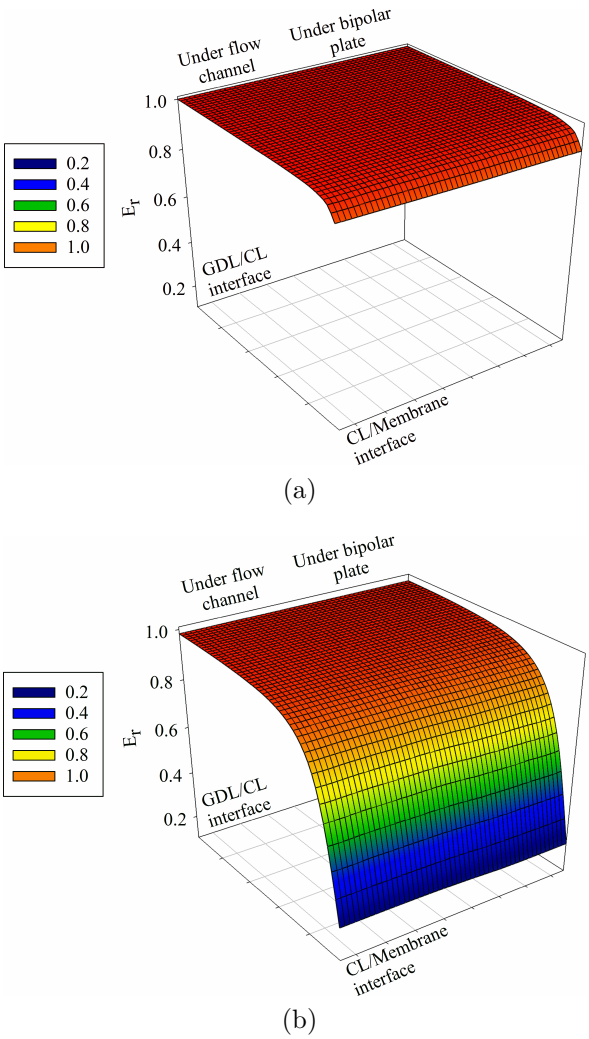

Figure 6.5: Effectiveness factor: (a) anode CL and (b) cathode CL. Operating parameters: $\phi_{cell} = 0.5V$, $T_0 = 323.15K$, $RH_a = 100\%$, $RH_c = 100\%$, $\xi_a = 2.0$, $\xi_c = 3.0$.

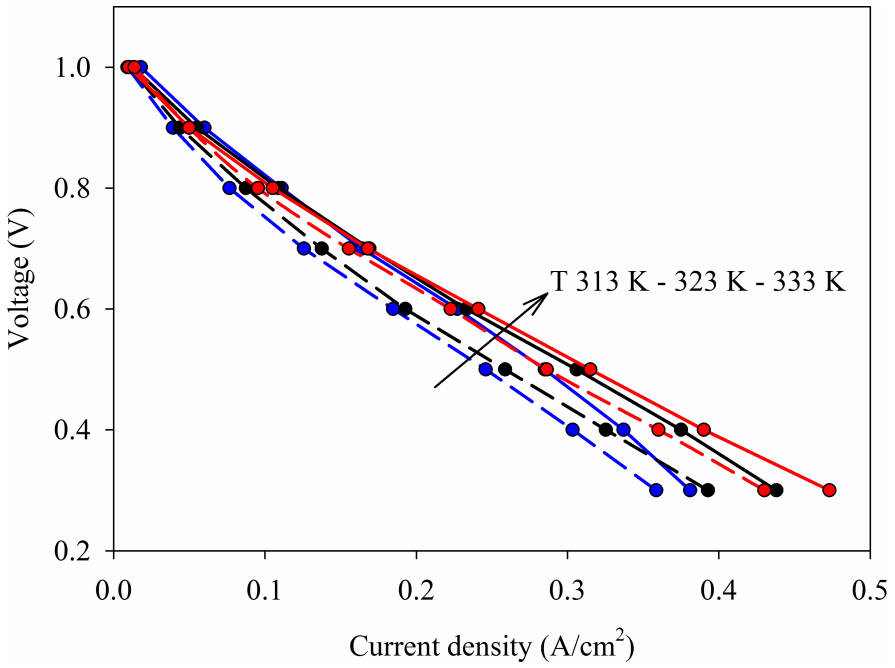

Figure 6.6: Effect of inlet temperature on the overall fuel cell performance. Solid lines are for a macro-homogeneous model and dashed lines are for an agglomerate model. Operating parameters: $\phi_{cell} = 0.3 - 1.0V$, $RH_a = 100\%$, $RH_c = 100\%$, $\xi_a = 2.0$, $\xi_c = 3.0$.

6.6 Effect of inlet temperature and relative humidity

In addition to the comparison between macro-homogeneous and agglomerate models from the overpotential and loss perspective, the effects of inlet temperature and relative humidity at the inlet channels on the overall performance are also analysed. The effect of the inlet temperature can be seen in Figure 6.6. As previously observed in our macro-homogeneous model, the rise in the inlet temperature of the fuel cell also resulted in an enhancement of the overall performance of the agglomerate model. This is mainly associated with the enhancement of the electrochemical kinetics and ionic diffusion facilitated at high temperatures. With the respect of the effect of the relative humidity, as presented in Figure 6.7, when operating under lower relative humidity the overall fuel cell performance is negatively affected in comparison to the fully humidified operation condition. As the presence of water vapour in the catalyst layer is scarce, the humidification of

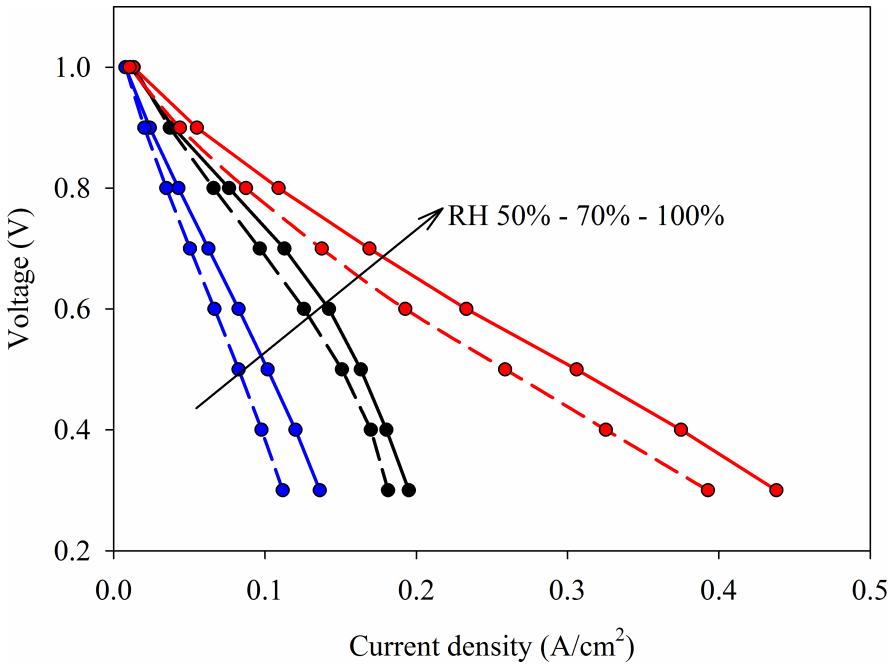

Figure 6.7: Effect of relative humidity on the overall fuel cell performance. Solid lines are for a macro-homogeneous model, and dashed lines are for an agglomerate model. Operating parameters: $\phi_{cell} = 0.3 - 1.0V$, $T_0 = 323.15K$, $\xi_a = 2.0$, $\xi_c = 3.0$.

the membrane is compromised for small values of relative humidity. Therefore, the ions transportation reduces and the Ohmic loss increases for small values of relative humidity, resulting in a deteriorated overall performance of the fuel cell.

6.7 Summary

In this chapter, the results from a three-dimensional agglomerate model of a generic AEM fuel cell are presented. Here, a detailed comparison between the proposed agglomerate model and a previously developed macro-homogeneous model was presented and the main differences between both models were discussed.

On the aspect of overall performance, the macro-homogeneous model overestimates the performance of the fuel cell when compared to the agglomerate model. This is mainly attributed to the subtle transport phenomena, which is not considered in the macro-homogeneous model. The lower reaction rate also

affects the membrane hydration as less water is produced and dragged due to ions transportation through the membrane. Thus, the Ohmic resistance is partially responsible for the deterioration of the overall performance obtained with the use of the agglomerate model.

The activation and concentration overpotentials obtained from the agglomerate and macro-homogeneous models are compared. The concentration overpotential profile in the cathode catalyst layer differs significantly between the macro-homogeneous and agglomerate models because the agglomerate model introduces resistances due to the transportation through the ionomer. Nevertheless, the faster diffusion of hydrogen in the ionomer did not affect significantly the concentration overpotential on the anode side. With respect of the activation overpotential, the agglomerate model is overpredicted by the macro-homogeneous model, resulting in an overestimation of the activation overpotential of the macro-homogeneous model. This is directly associated with the consideration of the effective specific platinum surface area per unit catalyst layer volume because the amount of Pt/C volume fraction and platinum loading have a direct impact on the reaction rate. The distribution of effectiveness factor of the catalyst layer has been analysed in detail in the context of the agglomerate model. The anode effectiveness factor does not show any significant variation, which implies uniform utilisation of the catalyst layer. Nevertheless, the utilisation of the cathode catalyst layer is compromised by the slower diffusion rate of oxygen and also a wide variation of the reaction rate through the catalyst layer length.

The influences of the inlet relative humidity and inlet temperature on the overall performance of the fuel cell in the context of the agglomerate model have been found to be qualitatively similar to those obtained from the macro-homogeneous model. An increase in the temperature positively affects the overall performance mainly due to the enhancement of the electrochemical kinetics. By contrast, the supply of less humidified gas in at the inlet results in a less favourable environment for the anion transportation, which in turn deteriorates the overall performance of the fuel cell.

Chapter 7

Results and Discussion - Part II: Agglomerate model

The results shown in Chapter 6 highlighted the main differences between the macro-homogeneous and the agglomerate model. It was observed that the differences in the concentration loss due to the additional resistances related to the species transportation within the catalyst layer domain. In addition to that, the Ohmic loss has been observed to increase due to the corrections imposed to the ions transport in both catalyst layer and membrane. It is worth noting that, in order to provide a quantitative comparison between macro-homogeneous and agglomerate model, the equations used to describe different phenomena such as electro-osmotic drag and equilibrium water content were kept constant. Nonetheless, the three-dimensional agglomerate model for an AEM fuel cell has been improved and utilised to analyse the effects of the operating conditions and key material parameters on the overall performance of the fuel cell. Hence, in order to better describe the physics of an AEM fuel cell, changes in the first agglomerate model were proposed and listed as follows:

- The thickness of the ionomer covering the agglomerate computed using the Equation (3.24) instead of the fixed value shown in Table 6.2;
- The electro-osmotic drag coefficient proposed by Springer et al. [79] is replaced by the electro-osmotic drag values measured by Li et al. [56] and correlated by Jiao et al. [42];

- As the reaction rate occurs at the electrode-electrolyte interface [55], the effective specific platinum surface area per unit catalyst layer volume has been modified from Equation (3.25) to Equation (3.26) in order to account for the surface area of the platinum spheres only;

- In the numerical model used in Chapter 6, the effective specific agglomerate surface area, a_{agg}, is defined as a constant ($= 3.6 \times 10^5\ m^2/m^3$) [80]. Nonetheless, as one of the proposals of the current agglomerate model, the numerical model has to be flexible in order to adequate the physical dimensions accordingly to the catalyst layer composition. Hence, the effective specific agglomerate surface area is obtained by using the Equation (3.62) [94, 96].

- The ambient temperature, T_∞, considered for all cases in this chapter is kept constant at 333.15 K.

Here, with the latest developed agglomerate model, the relative humidity at the inlets, the water content and the physical properties of the catalyst layer such as platinum and carbon loading and ionomer volume fraction are varied in order to find an optimum trade-off between various fuel cell losses arising from the variation of these parameters (i.e. mass transport, ionic resistance and kinetic losses). In this chapter, a co-flow regime is considered, therefore, the flow at the anode and cathode flow channel inlet is supplied at the same direction. The different cases and the values used in this detailed parametric analysis are presented in Table 7.1.

In addition to that, the electrochemical parameters used to perform the numerical simulation in this chapter were modified in comparison to Chapter 6 and are presented in Table 7.2.

Table 7.1: Simulation cases. Case 1 is the base case. Grey cells represent the different values used in this parametric analysis.

	RH_a (%)	RH_a (%)	γ_e	m_{Pt} (kg/m^2)	m_C (kg/m^2)	L_M	δ_{CL}
Case 1	95	50	1.0	0.004	0.006	0.22	1.00×10^{-5}
Case 2	50	50	1.0	0.004	0.006	0.22	1.00×10^{-5}
Case 3	50	95	1.0	0.004	0.006	0.22	1.00×10^{-5}
Case 4	70	70	1.0	0.004	0.006	0.22	1.00×10^{-5}
Case 5	95	50	1.5	0.004	0.006	0.22	1.00×10^{-5}
Case 6	95	50	2.0	0.004	0.006	0.22	1.00×10^{-5}
Case 7	95	50	1.0	0.006	0.006	0.22	1.00×10^{-5}
Case 8	95	50	1.0	0.01	0.006	0.22	1.00×10^{-5}
Case 9	95	50	1.0	0.004	0.016	0.22	2.39×10^{-5}
Case 10	95	50	1.0	0.004	0.0026	0.22	4.29×10^{-6}
Case 11	95	50	1.0	0.004	0.006	0.15	1.00×10^{-5}
Case 12	95	50	1.0	0.004	0.006	0.30	1.00×10^{-5}
Case 13	95	50	1.0	0.004	0.006	0.15	7.82×10^{-6}
Case 14	95	50	1.0	0.004	0.006	0.30	1.17×10^{-5}

Table 7.2: Electrochemical kinetic parameters

Parameter	Anode	Cathode	Unity
Reference exchange current density, j_0^{ref} [23, 57]	6.815	5.72×10^{-5}	A/m^2_{Pt}
Transfer coefficient, αn [74, 75]	0.5	1.0	-

7.1 Species transportation

A three-dimensional representation of the concentration contours for Case 1 at cell voltage of 0.4 V are presented in Figure 7.1. As one can see, a depletion of hydrogen and oxygen molar concentration towards the flow channel outlet is observed. With respect of water molar concentration at the anode, a rise of the molar concentration is observed as result of the water formation due to the electrochemical reaction. Even though water molecules are consumed at the cathode side, an augmentation of the water molar concentration is observed. This is mainly associated with the water molecules back diffusing from the anode catalyst layer to the cathode catalyst layer due to the water species gradient between both sides. A more detailed explanation about the aforementioned phenomenon is presented in the next section.

7.2 Relative Humidity (Case 1-4)

As presented in the Equations (3.139) and (3.140), the operating relative humidity is considered to define the boundary condition of anode and cathode flow channel inlets, respectively. In agreement with previous results [78], as can be seen from Figure 7.2, supplying higher relative humidity mixture at the anode flow channel inlet in comparison to the cathode flow channel inlet is proving to be beneficial to the overall performance of the fuel cell. For the cell voltage of 0.4 V, the highest current density (0.762 A/cm^2) is obtained for the Case 1 ($RH_a = 95\%$, $RH_c = 50\%$). In this case, due to the higher relative humidity at the anode catalyst layer in comparison to the cathode catalyst layer, the back diffusion phenomenon is observed and water diffuses from the anode to the cathode, as can be seen from Figure 7.2 where the spatial distribution of RH on both anode and cathode sides of the catalyst and gas diffusion layers are shown at different axial locations.

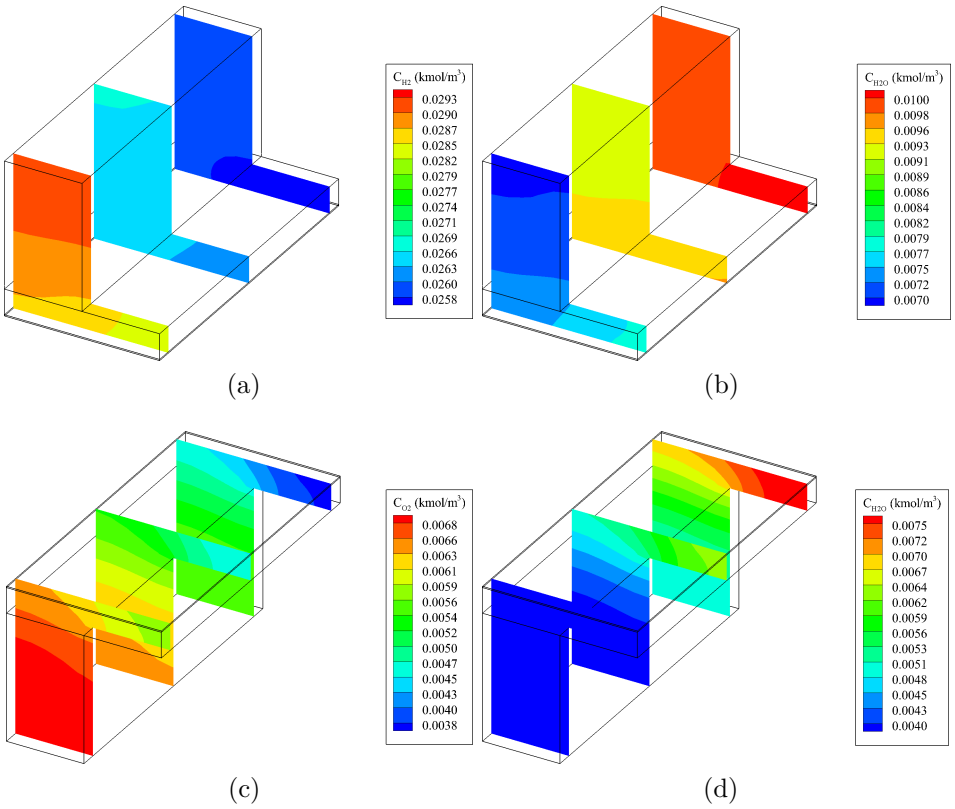

Figure 7.1: Molar concentration for the Case1: a) H_2, b) H_2O (anode), c) O_2, d) H_2O (cathode). Operating parameters: $\phi_{cell} = 0.3V$, $T_0 = 333.15K$, $\xi_a = 1.1$, $\xi_c = 2.0$.

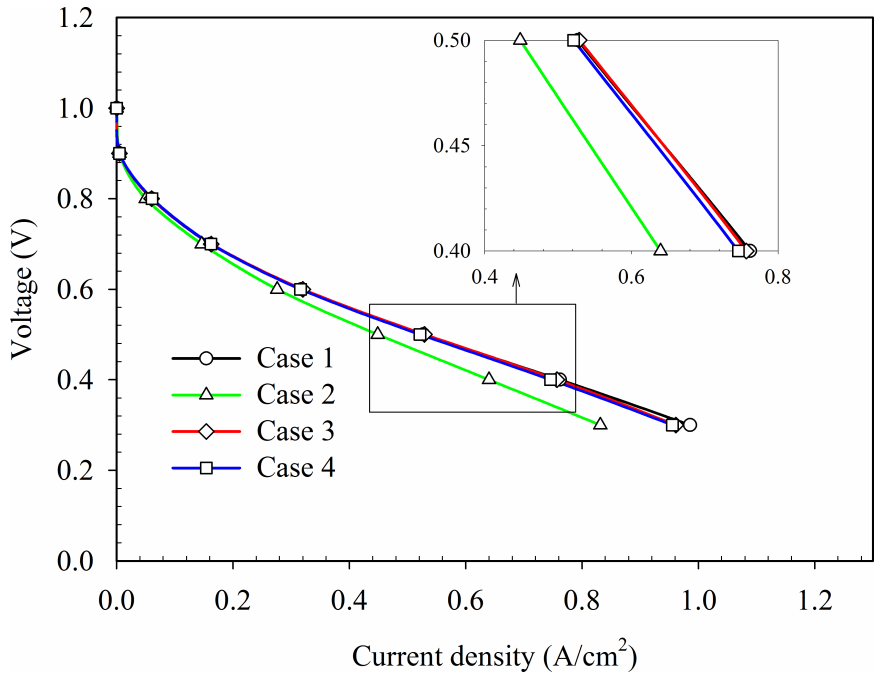

Figure 7.2: Polarisation curve for different relative humidity for anode and cathode inlet channel. Case 1 ($RH_a = 95\%$, $RH_c = 50\%$), Case 2 ($RH_a = 50\%$, $RH_c = 50\%$), Case 3 ($RH_a = 50\%$, $RH_c = 95\%$), Case 4 ($RH_a = 70\%$, $RH_c = 70\%$).

Water transport from the anode to the cathode catalyst layer as a result of a water back diffusion increases the average membrane water content. This, in turn, has a positive impact on the ionic conductivity through Equation (3.120). The increase in RH on the cathode side in the axial direction in Figure 7.3 indicates a net positive water flow rate (=53.49 kg/m^3s) in the cathode catalyst layer, which suggests that the back diffusion phenomenon overcomes the water consumption due to the electrochemical reaction. In addition to that, an average oxygen partial pressure at the cathode catalyst layer was observed to be 11.1 Pa. This water eventually gets transported to the anode catalyst layer due to the osmotic drag. On the anode side, condensation of water vapour is observed in Case 1 from halfway to the end of the fuel cell length and an average liquid water volume fraction of 0.081 is formed inside the CL and GDL pores. The current density in Case 2 ($RH_a = 50\%$, $RH_c = 50\%$) is approximately 17% smaller than in Case 1 (current density in Cases 1 and 2 are 0.762 A/cm^2 and 0.640 A/cm^2, respectively). It can be seen from Figure 7.3 that the magnitudes of RH are smaller in Case 2 than in Cases 1, 3 and 4, with an average oxygen partial pressure of 11.99 Pa. This reduction in relative humidity has a direct impact on the membrane water content, consequently lowering the ionic diffusion coefficient and increasing the Ohmic loss (0.27 V) of Case 2 in comparison to Case 1 (0.23 V). In addition to that, due to the lower humidification at both anode and cathode inlets, no liquid water has been formed in the anode catalyst and gas diffusion layer. Furthermore, the average back diffusion of the present case is lower (=69.21 kg/m^3s) in comparison to the base case (124.38 kg/m^3s). For Case 3 ($RH_a = 50\%$, $RH_c = 95\%$), as the relative humidity at anode and cathode inlet are set to be 50% and 95%, respectively, water diffuses from the cathode to the anode side close to the inlet region, as can be seen from Figure 7.3. Nevertheless, as water is consumed in the cathode catalyst layer for the anion formation and the water produced by the electrochemical reaction at the anode side, a higher relative humidity is observed at the anode catalyst layer in comparison to the cathode catalyst layer, which in turn gives rise to back diffusion water from the anode to the cathode side. The aforementioned phenomena can be seen in Figure 7.4, as higher values of membrane water content are observed closed to the inlet regions at the cathode side in comparison to the anode side especially under the land re-

gion. Hence, due to the gradient of the membrane water content between anode and cathode sides, membrane water diffuses from the cathode catalyst layer to the anode catalyst layer in that region. Nevertheless, as one can see in Figure 5b, the membrane water content at the anode side increases in the flow direction due to water diffusion from cathode and also owing to the water being product of the electrochemical reaction. Thus, the net water flux of membrane water content eventually changes direction and diffuses from the anode catalyst layer to the cathode catalyst layer. Additionally, the local back diffusion contours at both the anode catalyst layer and membrane interface, and at the cathode catalyst layer and membrane interface are presented in Figure 7.4c and 7.4d, respectively. When comparing the back diffusivity between Case 1 and Case 3, the average back diffusion value of the former was 37% higher in comparison to the latter (=77.90 kg/m^3s). Consequently, a higher ionic conductivity at the membrane has been observed on Case 1 (=5.04 S/m) in comparison to Case 3 (=4.38 S/m) as the average membrane water content has decreased from 17.83 to 16.62, respectively. As the back diffusion is lower in Case 3 than in Case 1, an average liquid water volume fraction of 0.100 (i.e. 10% flooding) is formed within the anode catalyst and gas diffusion layers and thereby slightly reduces the hydrogen diffusion into the anode catalyst layer. Moreover, the water molecules necessary for the reaction rate are partially supplied by the back diffusion and sorption, and thus the higher relative humidity at the cathode side (95 %) results in a lower average oxygen partial pressure (p_{O_2}= 9.98 Pa), reducing the oxygen diffusion to the reactive sites. Therefore, for a fixed 0.4 V output, a slightly reduction of the current density (from 0.762 A/cm^2 in Case 1 to 0.757 A/cm^2 in Case 3) is observed. In Case 4 (RH_a = 70%, RH_c = 70%), the desorption phenomenon at the cathode catalyst layer is weaker than in Case 1 due to the higher relative humidity at the domain. Therefore, when comparing Case 1 and 4 back diffusion, the former case transports more water from the anode to the cathode due to back diffusion (=124.38 kg/m^3s) in comparison to the latter (=98.97 kg/m^3s), as one can observed when comparing Figures 7.3a and 7.4d. Moreover, higher average oxygen partial pressure has been observed at the cathode catalyst layer (=11.22 Pa) than in Case 1. Similar to Cases 1 and 4, condensation of water also takes place at the anode catalyst and gas diffusion layers in Case 4 and a liquid water

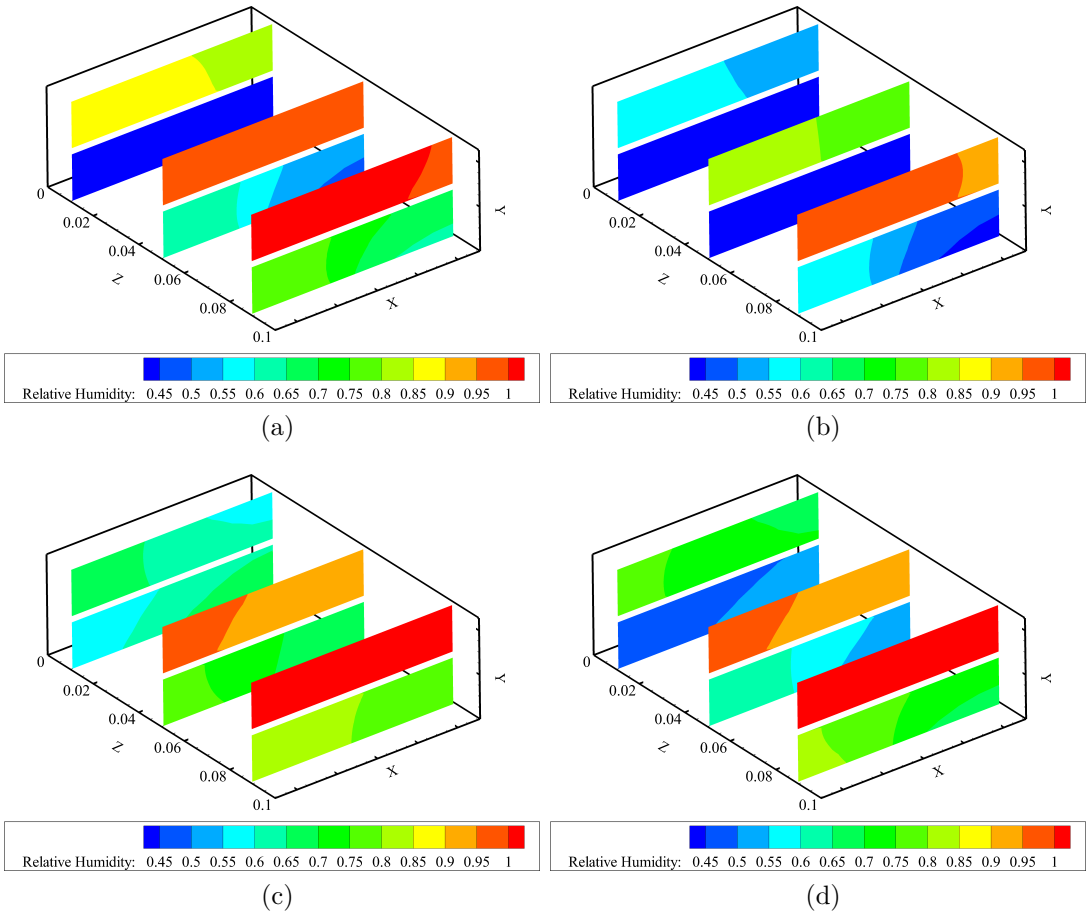

Figure 7.3: Relative humidity of anode (top) and cathode (bottom) catalyst layer and gas diffusion layer for: a) Case 1 ($RH_a = 95\%$, $RH_c = 50\%$), b) Case 2 ($RH_a = 50\%$, $RH_c = 50\%$), c) Case 3 ($RH_a = 50\%$, $RH_c = 95\%$) and d) Case 4 ($RH_a = 70\%$, $RH_c = 70\%$).

volume fraction of 0.07 has been observed.

It can be seen from Figure 7.5a that the temperature of the fuel cell reaches 340 K for the 0.4 V cell voltage. The main source of heat is the reaction rate at the anode side, thus temperature assumes higher values on the anode side than on the cathode side. The average reversible and irreversible source of heat have been observed to be 2.16×10^8 and 1.00×10^8 W/m^3, respectively. The higher temperature observed at the anode flow channel is consequence of the higher average thermal conductivity of the mixture at the anode side (=0.177 W/mK) in comparison to the cathode side (= 0.028 W/mK), thus extracting more heat from the

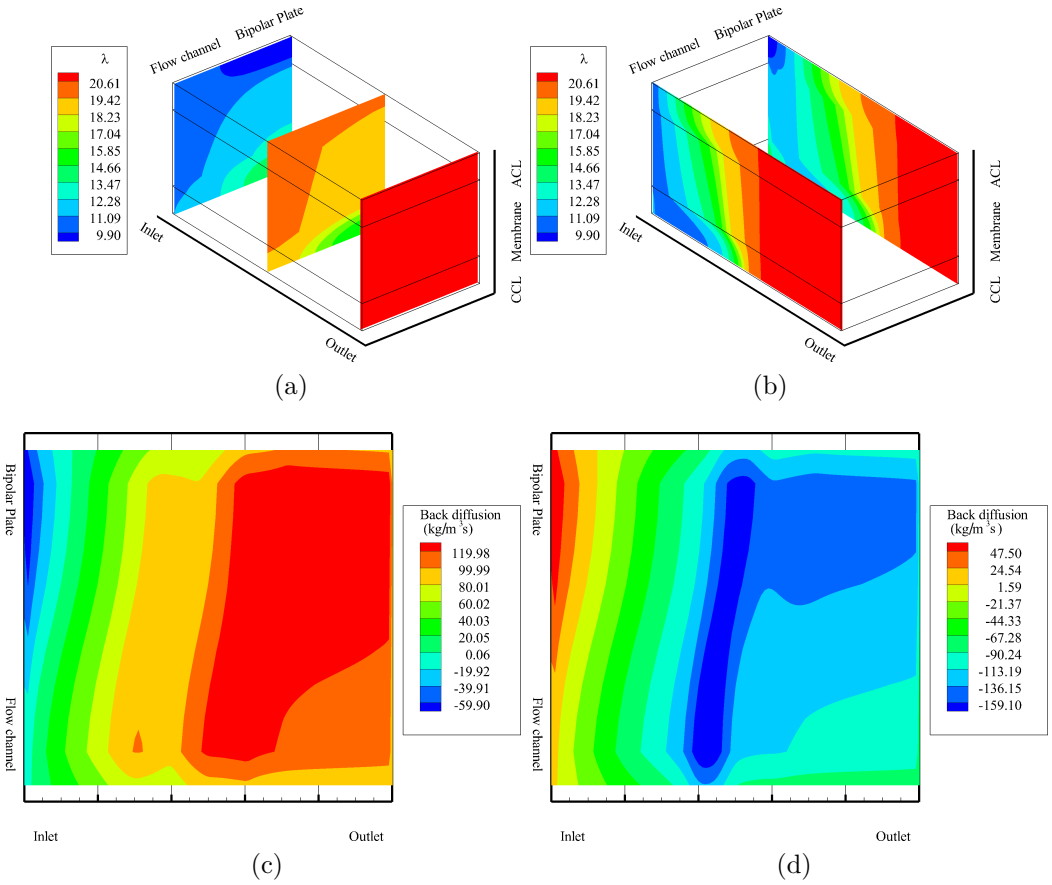

Figure 7.4: Local membrane water content contours of Case 3 (RH_a = 50%, RH_c = 95%) at 0.4 V: a) through-plane (z= 0.001; 0.05; 0.099 m) b) in-plane (x= 0.0001; 0.0009 m) c) local back diffusion at the anode catalyst layer/membrane interface d) local back diffusion at the cathode catalyst layer/membrane interface .

catalyst layers and the membrane stack. The contribution of the average Ohmic and latent heat source terms are 6.55×10^5 and 6.64×10^4 W/m^3, respectively, and have minor impacts in comparison to the average reversible and irreversible heat sources. As shown in Figure 7.5b, a same qualitative behaviour in terms of temperature distribution (i.e. high values on the anode side) is observed for the cell voltage of 0.6 V. For the cell voltage of 0.6 V, Case 2 exhibits the lowest current density (0.276 A/cm^2) for the reasons discussed above in the context of the 0.4 V cell voltage case. The activation loss is the main source of the loss for the cell voltage of 0.8 V, and thus relative humidity effects have not been presented for

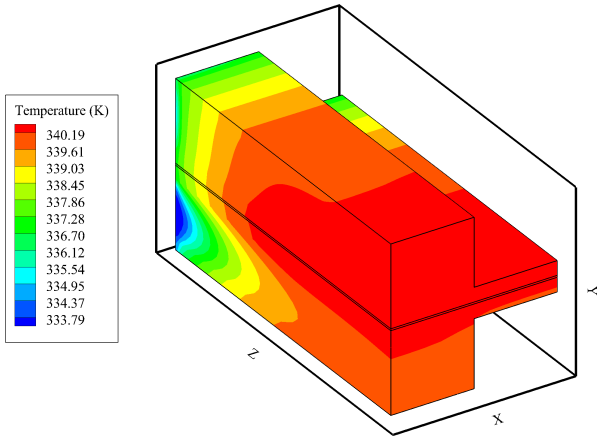

(a)

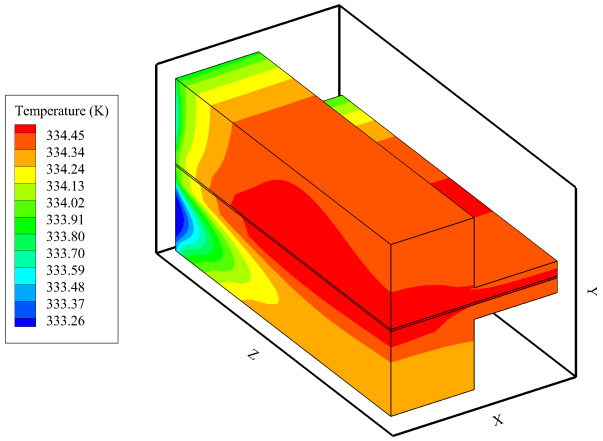

(b)

Figure 7.5: Temperature contours of Case 1 ($RH_a = 95\%$, $RH_c = 50\%$): a) 0.4 V and b) 0.6 V cell voltage.

this case.

7.3 Ionomer water uptake (Cases 1, 5-6)

humidity in the present work ($\lambda_e = 25.09$ at 100% relative humidity). Nevertheless, the ionomer water uptake is expected to reach higher values provided the material development allows for it. Therefore, in order to evaluate the catalyst layer performance under different water uptake properties, the membrane water

content is multiplied by the membrane water content factor γ_e (see Equation (3.104)). It is worth mentioning that, although the enhancement of the membrane water content is beneficial to the ionic diffusion, increasing the membrane water content weakens the mechanical properties of the membrane due to the swelling. It can be seen from Figure 7a that the current density of the fuel cell improves approximately by 8% (where current density =0.828 A cm-2) and 10% (where current density =0.848 A/cm^2), for Case 5 (γ_e=1.5) and Case 6 (γ_e=2.0), respectively in comparison to Case 1 (γ_e=1.0) for the cell voltage of 0.4 V. Equation (3.120) indicates that an increase in ionomer water content leads to a higher value of ionic conductivity in the catalyst layer and membrane, thus acts to reduce the Ohmic loss and increase the current density.

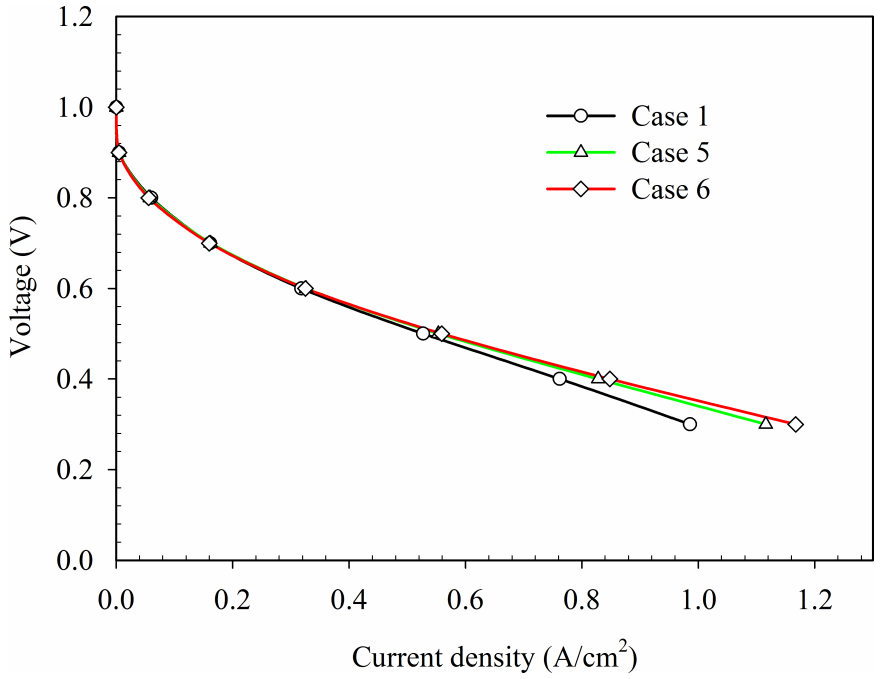

Figure 7.6: Overall performance for Case 1 (base case - γ_e=1.0, m_{Pt}=0.004 kg/m^2, m_C=0.006 k/gm^2, L_M=0.22, δ_{CL}=1.00 $\times$ 10^{-5} m) and different ionomer water content factor: Case 5 (γ_e=1.5) and Case 6 (γ_e=2.0).

The ionic conductivity of the membrane for Cases 5 and 6 are higher than in Case 1 (where ionic conductivity is 5.04 S m-1) by 25% (where ionic conductivity is 6.73 S/m) and 35% (where ionic conductivity is 7.70 S/m), respectively. As shown in Figure 7.7, the ionic potential at the cathode side for Case 6 (=0.479 V)

is higher than in Case 1 (=0.450 V) and 5 (=0.471 V), due to the enhancement of the ions conductivity as a result of a higher membrane water content. An augmentation of reaction rate is obtained due to the higher quantity of ions reaching the anode as a result of an enhanced ions conductivity, and this subsequently leads to an increase of the current density. In addition to that, as one can see from Equation (3.97), the membrane water diffusion coefficient is dependent on the local membrane water content. Moreover, using low RH at the cathode inlet results in higher O_2 partial pressure and consequently lower oxygen concentration loss. The water required for the reaction at the cathode is then instead supplied by water back diffusion from the anode. Therefore, as shown in Figure 7.7d, a more even distribution of the membrane water content has been obtained in the catalyst layer in Case 5 and 6 in comparison to the base case (i.e. Case 1). This results in a more even water vapour distribution at the catalyst layers in Cases 5 and 6 than in Case 1.

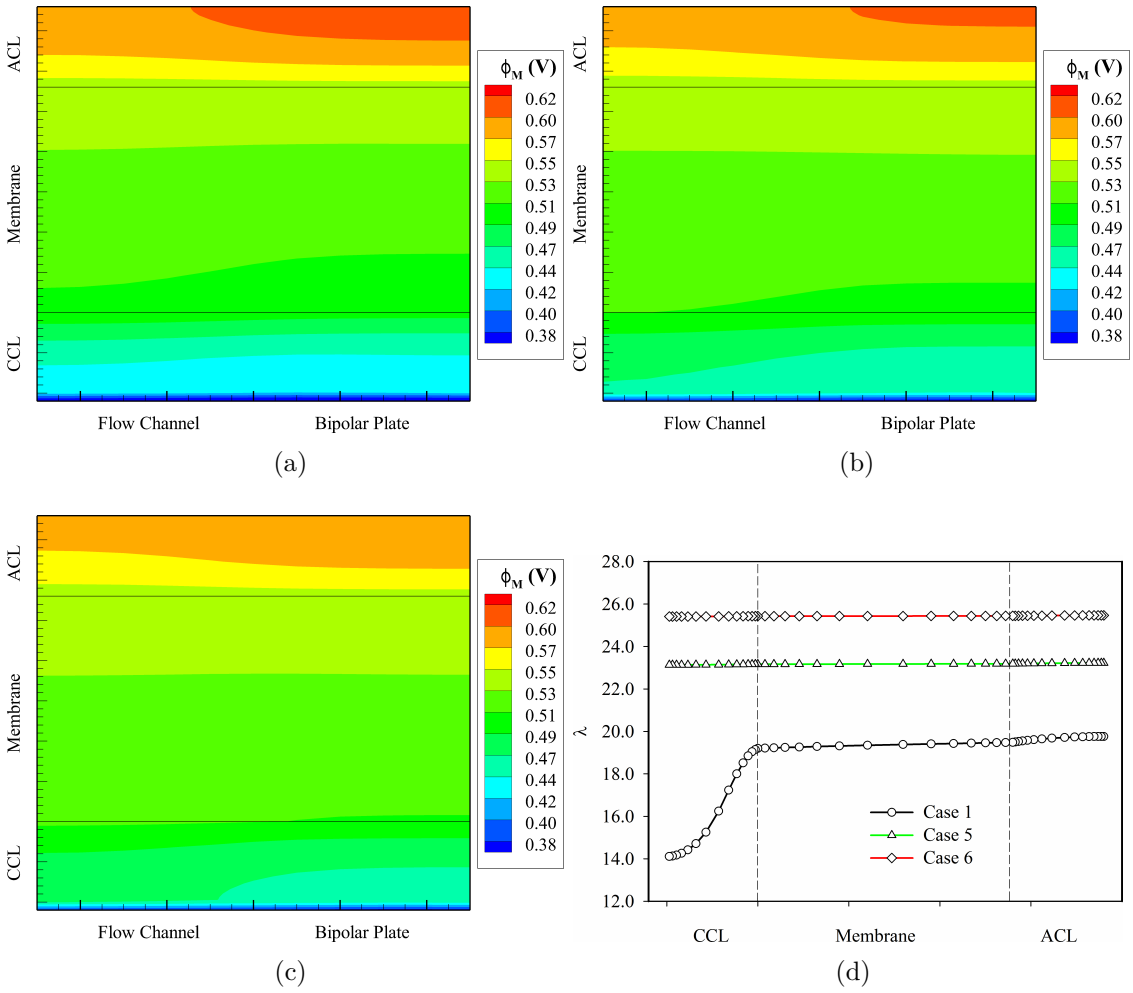

Figure 7.7: Ionic potential contour for: a) Case 1 (γ_e=1.0), b) Case 5 (γ_e=1.5), c) Case 6 (γ_e=2.0) and d) Local membrane water content for Case 1, 5 and 6 at z=0.5 m and x=0.0025 m.

7.4 Catalyst layer parameters

In order to analyse the influences of the catalyst layer composition on the fuel cell overall performance, the platinum loading, carbon loading and ionomer volume fraction were varied. Here, two different approaches have been adopted in order to perform a comprehensive analysis of the effects of the aforementioned parameters on the overall fuel cell performance. The first approach considers a fixed catalyst layer thickness and thus the volume fractions given by Equation (3.21)

are adjusted accordingly, as a consequence of the variation of the parameters. In the second approach, the catalyst layer porosity is kept constant and the catalyst layer thickness is adjusted in other to accommodate the platinum, carbon and ionomer loadings within the catalyst layer volume.

7.4.1 Platinum loading (Cases 1, 7-8)

Figure 7.8 shows significant improvement in terms of the overall performance can be obtained by increasing the platinum and carbon loading. For example, both Cases 7 (m_{Pt}=0.006 kg/m^2) and 8 (m_{Pt}=0.01 kg/m^2) show better performance in comparison to Case 1 (m_{Pt}=0.004 kg/m^2). For the cell voltage of 0.4 V, the current densities for Cases 7 and 8 have been found to improve by 12% (the current density is 0.865 A/cm^2 for Case 7) and 25% (the current density is 1.0 A/cm^2), respectively. This is directly associated with an increase of the effective surface area per unit volume of the catalyst layer (e.g. a_{Pt}^{eff} values are 1.21×10^7 $1/m$ and 2.13×10^7 $1/m$ for Case 7 and 8 respectively in comparison to 7.88×10^6 $1/m$ in Case 1). As a consequence of this augmentation of the effective specific area per unit catalyst layer volume, the activation loss decreases because an increased area of platinum is exposed to the ions. The activation losses at the anode catalyst layer for Case 7 and 8 have been found to be 0.102 V and 0.077 V, respectively, whereas it was observed to be 0.120 V for Case 1. Nevertheless, a modest reduction of the activation loss in the cathode side is observed, reducing the activation loss from -0.4 V to -0.38 V for Case 1 and 8, respectively. It can be seen from Table 7.3 that the catalyst layer porosity decreases with an increase in the platinum load. Thus, despite of the augmentation of the overall performance, the mass transportation loss has increased from 0.048 to 0.052 V at the cathode catalyst layer when comparing the Cases 8 for 0.4 and 0.3 V output voltage, respectively. It is worth mentioning that an increase in the platinum loading has a direct impact on the fuel cell cost. Therefore, a balance between the cost and performance has to be considered for large scale applications. Due to the smaller size of the platinum particles than the carbon particles, the variation of the catalyst layer thickness in response to the change in platinum loading is marginal, and thus, no analyses has been performed in this aspect.

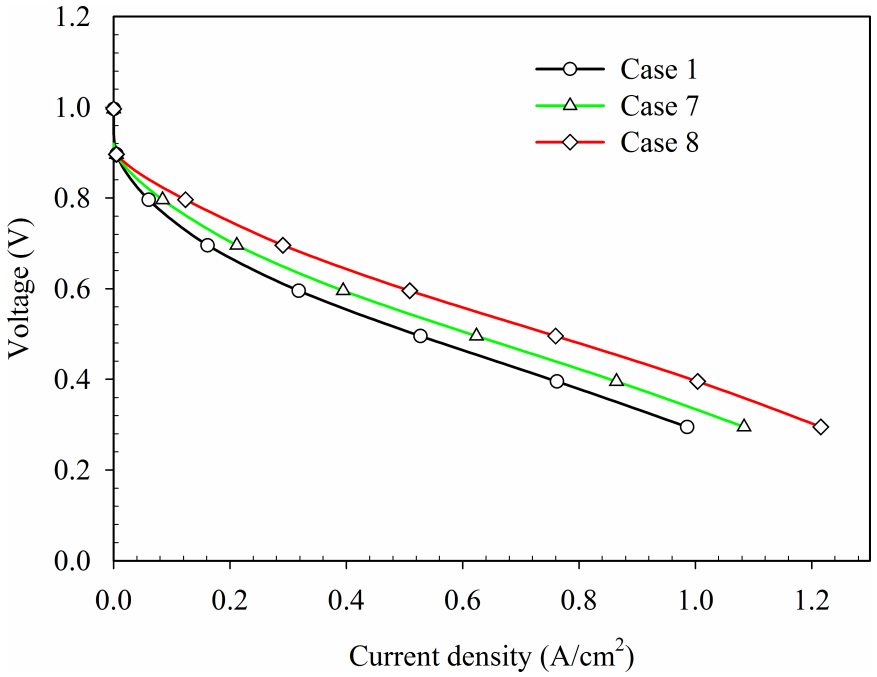

Figure 7.8: Overall performance for Case 1 (base case - γ_e=1.0, m_{Pt}=0.004 kg/m^2, m_C=0.006 k/gm^2, L_M=0.22, δ_{CL}=1.00 $\times 10^{-5}$ m) and different platinum loading: Case 7 (m_{Pt}=0.006 kg/m^2) and Case 8 (m_{Pt}=0.01 kg/m^2).

7.4.2 Carbon loading (Cases 1, 9-10)

For Cases 9 (m_C = 0.016 kg/m^2, δ_{CL} = 2.39 $\times$ 10^{-5} m) and 10 (m_C = 0.0026 kg/m^2, δ_{CL} = 4.29 $\times$ 10^{-6} m), the carbon loading has been modified (see Table 7.1) in such a manner that the catalyst layer porosity is kept unaltered and the catalyst layer thickness has been changed in order to allocate the carbon mass loading within the domain. An increase of the catalyst layer thickness, due to reduction of the platinum and carbon mass ratio, reduces the effective specific area per unit catalyst layer volume. Accordingly, as presented in Figure 7.9, Case 9 (i.e. f= 0.20) exhibited a current density of 0.663 A/cm^2 in comparison to 0.762 A/cm^2 in Case 1 mainly due to the depletion of the reaction rate coefficient (Equations (3.68) and (3.69)) due to the reduction of the effective surface area to volume ratio of the catalyst layer. By contrast, Case 10 (i.e. f= 0.60) showed a 6.0% increase in current density (=0.810 A/cm^2) in comparison to Case 1 (=0.762 A/cm^2). The thinner catalyst layer in Case 10 than in Case 1 reduces the resistance to species diffusion, thus reducing the concentration loss on both

Table 7.3: Physical properties of the catalyst layer.

	δ_{CL} (m)	m_{Pt} (kg/m^2)	m_C (kg/m^2)	f (%)	$L_{Pt/C}$	L_M	ϵ_{CL}
Case 1	1.00×10^{-5}	0.004	0.006	0.400	0.352	0.220	0.428
Case 7	1.00×10^{-5}	0.006	0.006	0.500	0.361	0.220	0.419
Case 8	1.00×10^{-5}	0.01	0.006	0.625	0.380	0.220	0.400
Case 9	2.39×10^{-5}	0.004	0.016	0.200	0.380	0.220	0.400
Case 10	4.29×10^{-6}	0.004	0.0026	0.606	0.380	0.220	0.400
Case 11	1.00×10^{-5}	0.004	0.006	0.400	0.352	0.150	0.498
Case 12	1.00×10^{-5}	0.004	0.006	0.400	0.352	0.300	0.348
Case 13	7.82×10^{-6}	0.004	0.006	0.400	0.450	0.150	0.400
Case 14	1.17×10^{-5}	0.004	0.006	0.400	0.300	0.300	0.400

anode and cathode sides. Moreover, in addition to the reduction of the Ohmic loss due to the thinner catalyst layer, the water sorption at the anode catalyst layer in this case (i.e. Case 10) has increased to 5.92 $1/m^3s$, which is higher than that in Case 1 (=3.72 $1/m^3s$), which results in a higher conductivity and, consequently a smaller Ohmic loss. All of these contribute to higher current density of Case 10 than in Case 1. Therefore, for the analysed cases, a thinner catalyst layer has been proved to be more effective on the improvement of the overall performance of the fuel cell. In addition to that, the thinner layer of ionomer covering the agglomerate in Cases 9 and 10 than in Case 1 diminishes the resistance opposed to the ions and species. On the other hand, the average liquid water volume fraction of 0.191 (i.e. 19.1% flooding) present at the anode catalyst layer and gas diffusion layer increases the possibility of flooding.

7.4.3 Volume fraction of ionomer (Cases 1, 11-14)

In the present study, the kinetic parameters of the HOR/ORR were kept fixed (i.e. transfer coefficient (α) and exchange current density ($j_{0^{ref}}$)). However, the

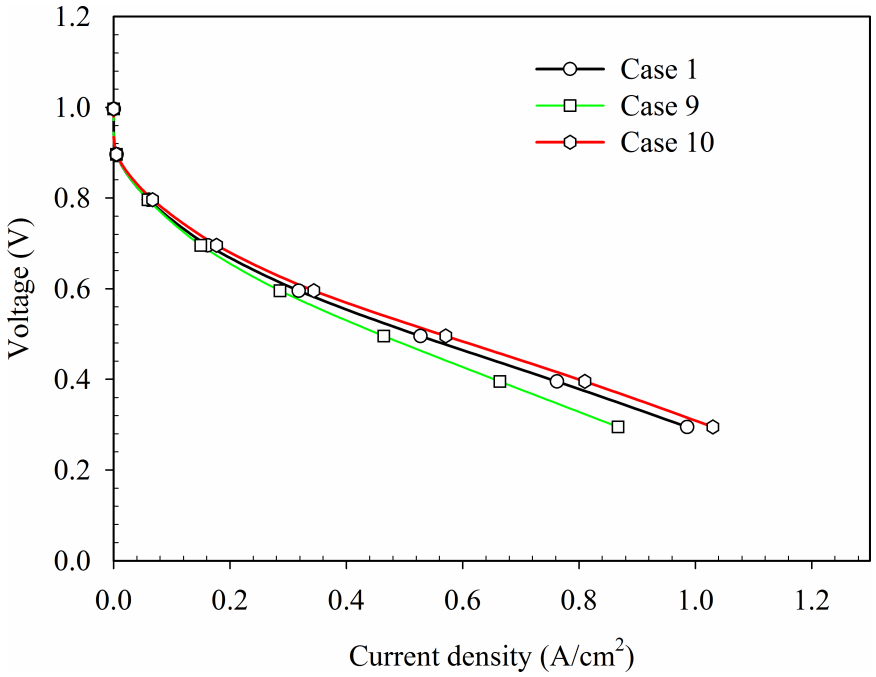

Figure 7.9: Overall performance for Case 1 (base case - γ_e=1.0, m_{Pt}=0.004 kg/m^2, m_C=0.006 k/gm^2, L_M=0.22, δ_{CL}=1.00 $\times$ 10^{-5} m) and different carbon loading: Case 9 (m_C=0.016 kg/m^2, δ_{CL}=2.39 $\times$ 10^{-5} m) and Case 10 (m_C=0.0026 kg/m^2, δ_{CL}=4.29 $\times$ 10^{-6} m).

ionomer volume fraction has effect on the ionic conductivity and the membrane water content diffusion coefficient, as presented on Equations (3.119) and (3.95), respectively. Moreover, the ionomer volume fraction has an impact on the volumetric current density, i_{CL}, as the thickness of the ionomer (δ_M) is calculated based on the ionomer volume fraction. In Cases 11 and 12, the ionomer volume fraction was modified but the total catalyst layer thickness was kept unchanged for the purpose of numerical experimentation. This consequently modified the catalyst layer porosity. In Cases 13 and 14, the ionomer volume fraction was changed for a given set of values of $L_{Pt/C}$ and ϵ_{CL} and consequently the catalyst layer thickness, δ_{CL}, changed. The second approach is closer to the reality, whereas the first approach addresses the possibility that might arise as a result of material development. As mentioned earlier, ϵ_{CL} and L_M affect all the transport mechanisms.

7.4.3.1 Fixed catalyst layer thickness

The overall performance of the cases analysed for the variation of the volume fraction of ionomer content in the catalyst layer is presented in Figure 7.10. Even though the volume fraction of the catalyst layer pores increased as consequence of the reduction of ionomer volume fraction to 0.15 (Case 11), the overall performance of the fuel cell deteriorated in comparison to Case 1 (where L_M= 0.22). For the cell voltage of 0.4 V, the current density in Case 11 (=0.590 A/cm^2) is approximately 30% smaller than in Case 1 (=0.762 A/cm^2). This behaviour originates mainly due to the corrections in the ionic and membrane water content diffusion coefficients (see Equations (3.119) and (3.95)). An opposite behaviour is observed when the ionomer volume fraction is increased to 0.30 (i.e. Case 12). As both ions and water diffusion rate coefficients increase with an increase of the ionomer volume fraction, the overall performance of Case 12 is superior to Case 1. Nevertheless, it is worth mentioning that the concentration loss in Case 14 starts to become significant for high current density, which can be seen in Figure 7.10 for the 0.3 V output case. Therefore, for a typical fuel cell operating condition (e.g. 0.6 V output), an ionomer volume fraction of 0.30 is recommended.

7.4.3.2 Fixed catalyst layer porosity

Figure 7.10 shows that Case 13, which has thinner catalyst layer than in Case 1, yields of 0.701 A/cm^2 in comparison to 0.762 A/cm^2 in Case 1. The reduction of the volume fraction of ionomer in Case 13 overcomes the enhancement of the electrons conductivity due to the increases in platinum loading (see Equation (3.111)) and effective surface, which, for a fixed voltage, increases the Ohmic losses at both catalyst layers in comparison to that in Case 1. Nevertheless, when comparing the overall performance of Case 13 and Case 12, the latter showed higher current density production. The performance enhancement of Case 13 is mainly associated with the larger effective surface area of the catalyst layer in comparison to Case 11. By contrast, Case 14 exhibits a higher current density (0.811 A/cm^2) than in Case 1 (0.762 A/cm^2). This is a consequence of the faster diffusion of ions and water content in the catalyst layer in Case 14 and thus the Ohmic loss within the catalyst layer is smaller than in Case 1, which increases the

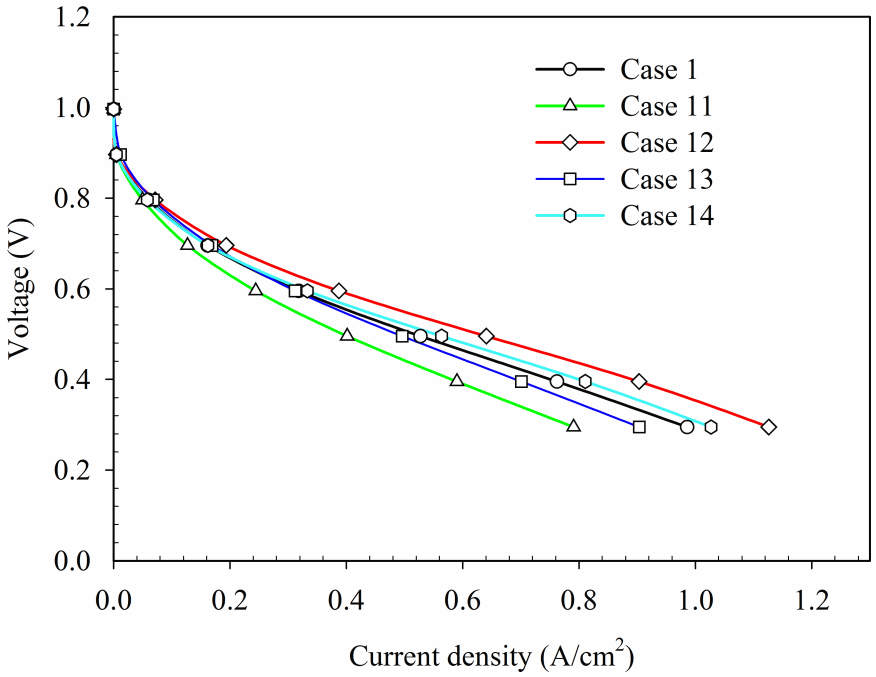

Figure 7.10: Overall performance for Case 1 (base case - γ_e=1.0, m_{Pt}=0.004 kg/m^2, m_C=0.006 k/gm^2, L_M=0.22, δ_{CL}=1.00 $\times$ 10^{-5} m) and different carbon loading: Case 11 (L_M=0.15 kg/m^2, δ_{CL}=1.00 $\times$ 10^{-5} m), Case 12 (L_M=0.30 kg/m^2, δ_{CL}=1.00 $\times$ 10^{-5} m), Case 13 (L_M=0.15 kg/m^2, δ_{CL}=7.82 $\times$ 10^{-6} m), Case 14 (L_M=0.30 kg/m^2, δ_{CL}=1.17 $\times$ 10^{-5} m).

overpotential at anode and cathode catalyst layers in Case 14 in comparison to Case 1. For the range of ionomer volume fraction studied in this work, an ionomer volume fraction of 0.30 has been found to yield the best overall performance of the fuel cell. Nevertheless, the augmentation of the ionomer volume fraction is limited by aspects such as the reduction of the catalyst layer porosity and the thickening of the ionomer film (e.g. higher concentration loss) and increase of the catalyst layer thickness (e.g. increase of the Ohmic loss).

7.5 Summary

In this chapter, a three-dimensional multiphase agglomerate model for an AEM fuel cell has been developed in order to perform a detailed parametric analysis in terms of the variations of relative humidity at the inlet, ionomer water uptake, ionomer volume fraction, platinum and carbon loading. The relative humidity

at the inlet has been proved to have a significant influence on the fuel cell performance. The back diffusion of regents has been found to play an important role on the membrane hydration, which acts to increase the ionic conductivity. Therefore, an increase in the current density has been obtained under higher relative humidity at the anode side. Moreover, back diffusion has been shown to be responsible for partial supply of the reagents in the cathode catalyst layer for the ion formation.

The overall performance of AEM fuel cell has been found to improve with increasing membrane water uptake. When the relative humidity is kept at 50% at the cathode inlet, an increased oxygen partial pressure enhances oxygen diffusion to the reactive sites within the catalyst layer. Moreover, the water consumed for the ion formation is partially obtained by the water back diffusion from the anode to the cathode side.

The variation of the platinum loading affects the effective surface area to volume ratio of the catalyst layer, which increases with platinum loading, allowing ions to easily reach the reactive sites. Furthermore, a reduction of the activation loss has been observed with increasing platinum loading. The catalyst layer thickness decreases with decreasing carbon loading when the catalyst layer porosity is kept unaltered, and this improves the overall performance of the fuel cell due to the combination of reduced Ohmic loss and the thinning of ionomer layer thickness.

An increase in ionomer volume fraction enhances both ions and membrane water content diffusion at the cost of increase in thickness of the ionomer and consequently reduction in reactants permeability through the agglomerate film. However, this has limited influence as its increase is directly related to the decrease of the porosity in the catalyst layer when the catalyst layer thickness is kept unaltered. It is worth noting that ionomer swelling might significantly affect the overall performance of the AEM fuel cell when operating under high relative humidity conditions. Hence, the implementation of such phenomenon is necessary to unveil its effect on the many inter-related phenomena such as membrane water content, ionic diffusion (i.e. Ohmic loss) and water back diffusion through the membrane just to name a few.

Chapter 8

Conclusions and Future Work

The numerical macro-homogeneous model proposed is governed by 12 coupled governing equations: mass, momentum, species, energy, electronic potential, ionic potential, membrane water content and liquid water. The aforementioned equations are interrelated by the reaction rate, several transportation and phase change phenomena such as electro-osmotic drag, sorption/desorption, evaporation/condensation and back diffusion. Based on the proposed macro-homogeneous model presented in the previous chapters of this thesis, several modifications have been implemented in order to build an improved three-dimensional agglomerate model for an AEM fuel cell. Both macro-homogeneous and agglomerate models have been numerically implemented in a commercial finite-volume CFD software and grid independence and convergence criteria test were performed. In addition to that, the validation of the models has been performed by comparing simulation results with experimental data. Finally, both macro-homogeneous and agglomerate models were used in a single-channel fuel cell and an extensive parametric analysis was performed.

Firstly, the macro-homogeneous models have been widely used in the existing literature to describe the transportation and the several interrelated phenomena presented during the operation of an AEM fuel cell. As one can see in Chapter 5, the proposed macro-homogeneous model has not shown significant impact on the overall performance of the fuel cell when comparing the current density of co-flow and counter-flow modes. Similar results have been observed by Ge et al. [28] on the study of flow modes on PEM fuel cells. Further investigation also

shows that this behaviour is independent of the operating temperature. Nevertheless, the operating temperature has been proven to have a significant impact on the overall performance of the fuel cell. This is mainly associated with the enhancement of the electrochemical kinetics and the hydration of the membrane due to the electro-osmotic drag. Nevertheless, it is worth noting that membrane stability under high operating temperatures (353-368 K) is still one of the challenges regarding the material development [21]. As previously observed by Zhang et al.[101], efficient water management can significantly improve the overall performance of the fuel cell. For the range of relative humidity tested, a positive impact has been observed on the overall performance of the fuel cell when operating under high relative humidity (90-100%). Enhancing the membrane water content transportation through the membrane by maintaining high relative humidity at the catalyst layers, offers an augmentation of the overall performance of the fuel cell, as the ionic conductivity is highly sensitive to the membrane humidification. On the other hand, the excessive liquid water formation at the anode side might contribute to the porous clogging, thus negatively affecting the species transportation through the pores (i.e. rising of the concentration loss). Hence, maintaining the liquid water formation under control by reducing the cathode relative humidity supply (i.e. increasing the back diffusion) can possibly result in an augmentation of the overall performance of the AEM fuel cell. Therefore, despite the limitations in relation to the characterisation of the catalyst layer (i.e. platinum and carbon loading) and limited capacity to describe subtle transportation within the catalyst layer, the macro-homogeneous model is a powerful tool to numerically describe an AEM fuel cell and to predict the overall performance of an AEM fuel cell in a qualitative sense.

Secondly, an extensive comparison between the macro-homogeneous and the agglomerate models has been performed. From the overall performance point of view, the macro-homogeneous model over-predicts the current density produced by the fuel cell in comparison to the agglomerate model. This over-estimation arises due to the absences of species and ions transportation resistances in the macro-homogeneous model. The increase of the Ohmic resistance is a consequence of the dehydration of the membrane, as the reaction rate is reduced and the electro-osmotic drag transport is negatively affected. Even though the Ohmic

loss corresponds to approximately 70% of the losses in the performed analysis, the most affected by the implementation of the agglomerate were the concentration and the activation losses. The inclusion of a second characteristic length (i.e. ionomer thickness), leads to slowing down the diffusion of hydrogen and oxygen from the pores to reactive sites due to the extra resistance imposed by the ionomer layer covering it. Nevertheless, as hydrogen diffuses faster than oxygen in the ionomer medium, the concentration loss is more crucial at the cathode catalyst layer. With respect to the activation loss, a pronounced impact of the catalyst layer composition has been observed when the fuel cell is operated at lower output voltage conditions.

One of the important aspects of the agglomerate model is the capacity to take into account the effective specific platinum area per unit of catalyst layer volume, which is directly related with the exchange current density of the catalyst layer. Hence, a more realistic approach to describe how easily the electrochemical reaction can take place has been considered.

Another important addition to the agglomerate model is the implementation of the effectiveness factor. Significant differences have been observed in the effectiveness factor of anode and cathode catalyst layers. When operating at 0.5 V cell voltage, the utilisation of the anode catalyst layer was significantly higher in comparison to the cathode catalyst layer, especially close to the membrane/catalyst layer interface. It has been observed that increasing the ratio of reaction and oxygen diffusion rates (i.e. approaching membrane/catalyst layer interface) decreases the utilisation of the cathode catalyst layer, indicating that the ORR is determined by the oxygen diffusion rather than the electrochemical reaction. The opposite effect has been observed in the anode catalyst layer, as due to the faster hydrogen diffusion rate, the reaction rate has been observed to be the limiting factor (i.e. high effectiveness factor). Additionally, the effect of the operating temperature and relative humidity on the overall performance of the fuel cell has been analysed. As expected, an over prediction by the macro-homogeneous model in comparison to the agglomerate model has been observed for both temperature and relative humidity.

Finally, the latest version of the agglomerate model has been used to numerically simulate a generic AEM fuel cell. Modifications in the effective specific

platinum surface area per unit catalyst layer volume (a_{Pt}^{eff}), the effective specific agglomerate surface area (a_{agg}) and the the thickness of the ionomer covering the platinum dispersed carbon particles were necessary to precisely represent the phenomena transportation within the catalyst layer and the corresponding physical processes in the AEM fuel cell. In order to address the water management issues presented by Dekel [21], a detailed analysis of the effects of the inlet relative humidity has been performed. Among the different cases tested, special attention has been given to the asymmetric configuration where the anode and cathode inlet relative humidity were defined as 95% and 50%, respectively. This case has been reported to have the highest average current density in comparison to the other cases where relative humidity was varied. This is partially a consequence of the water vapour gradient between anode and cathode, thus resulting in a positive net water flow from anode to cathode (i.e. back diffusion), thus maintaining the membrane hydrated and enhancing the ions transportation from cathode to anode side. Another important aspect of the aforementioned configuration is the fact that, due to the lower relative humidity at the cathode flow channel inlet, the partial pressure of oxygen is higher, thus enhancing the oxygen diffusion from the flow channel to the catalyst/membrane interface. No major loss regarding the lower relative humidity at the cathode side is observed as the water vapour necessary for the ORR is partially provided via back diffusion.

With respect to the ionomer water uptake, Bharath et al. [10] has recently reported values as high as $\lambda_e = 25$ at 100% relative humidity. Nevertheless, this value was extrapolated for higher realistic values given the advancements in material development. An increase of the average current density has been observed when increasing the ionomer water content by a factor of 1.5 and 2.0. This increment not only enhanced the ionic diffusion through the membrane due to the higher membrane hydration state, but also enhanced the ionic conductivity of the membrane. Thus, the overall Ohmic loss regarding the ions transportation through the membrane has been reduced.

With respect to the platinum and carbon loading, the agglomerate model has been proven to be a powerful tool to numerically evaluate the effect of different loadings on the overall performance. The increase of the platinum loading in the catalyst layer has been observed to be beneficial to the overall performance of

the fuel cell, as the effective surface area per unit volume of the catalyst layer increases. In addition to that, the exchange current density is increased, thus decreasing the activation loss in the anode and cathode catalyst layer. Nevertheless, the increase of platinum loading in the catalyst layer reduces the catalyst layer porosity, which has been observed for lower cell voltages (i.e. 0.3 V) to give rise to an increase in the concentration loss.

The effects of carbon loading have also been analysed in this thesis. The increase of the carbon loading, for a unaltered catalyst layer porosity, results in a thicker catalyst layer, thus increasing the resistance to the species transportation through the catalyst layer. In addition to that, the reduction of the platinum to carbon mass ratio, results in a reduced effective specific area per unit catalyst layer volume. Therefore, the exchange current density is decreases, leading to a higher activation loss at both anode and cathode catalyst layers. Opposite behaviour has been observed when the carbon loading is decreased, as due to the thinner catalyst layer, the species diffusion and Ohmic resistance are reduced, resulting in a higher average current density in comparison to the base case.

With respect to the variation of ionomer volume fraction in the catalyst layer, an augmentation of the current density has been observed when increasing the ionomer volume fraction. This was mainly associated with the increase of the ionic conductivity in the catalyst layers. Nevertheless, the augmentation of the ionomer volume fraction causes a reduction of the catalyst layer porosity or an increase of the Ohmic loss due to the catalyst layer thickening. When considering the lowering of the ionomer volume fraction, the simulation results have shown a reduction of the performance in comparison to the base case, mainly due to the increase in the ionic resistance in the catalyst layers. In spite of that, for the cases with lower ionomer volume fraction (i.e. $L_M = 0.15$), the thinner catalyst layer case showed better overall performance than the case where the porosity has increased. This is associated with the fact that the Ohmic loss is responsible for approximately 70% of the fuel cell losses for the parameters analysed in this work.

A summary of the key findings of this thesis is listed as follows:

- Despite the qualitative agreement with experimental results, the macro-homogeneous model over-predicts the overall performance of the AEM fuel

cell and fails to consider subtle transportations within the catalyst layer;

- The agglomerate model is capable of addressing different compositions of catalyst layer, thus adding versatility to the numerical simulation;
- Catalyst layer parameters such as ionomer volume fraction, platinum and carbon loadings have significant impact on Ohmic, concentration and activation losses, hence significantly impacting the overall performance of the fuel cell;
- A successful water management strategy is strongly dependent on the operating temperature and relative humidity at the flow channel inlets.

Based on the conclusions drawn from the research described in this thesis, a list of future work has been proposed as follows:

- Evaluation of the catalyst layer degradation due to air pollutants and its effect on the overall performance of the cell and comparison with experimental results [90, 103];
- Perform a transient numerical analysis of an AEM fuel cell utilising the agglomerate model;
- Numerical modelling of secondary pores between Pt/C particles and ionomer covering layer;
- Incorporation of the effects of the ionomer swelling due to the membrane hydration and evaluate its impact on the species and ions transportation;
- Development of numerical correlations to characterise and describe material properties related to AEM fuel cell;
- Simulation and modelling of multi-channel AEM fuel cells to evaluate current density and water phases distribution;
- Overall performance optimisation based on entropy generation analysis.

References

[1] National Fuel Cell Research Center. http://www.nfcrc.uci.edu. Accessed: 2010-09-30.

[2] Department of Energy. http://energy.gov. Accessed: 2010-09-30.

[3] Web of Knowledge. http://apps.webofknowledge.com. Accessed: 2010-09-30.

[4] K. Asazawa, T. Sakamoto, S. Yamaguchi, K. Yamada, H. Fujikawa, H. Tanaka, and K. Oguro. Study of anode catalysts and fuel concentration on direct hydrazine alkaline anion-exchange membrane fuel cells. *Journal of The Electrochemical Society*, 156(4):B509–B512, 2009.

[5] L. Barelli, G. Bidini, and A. Ottaviano. Optimization of a pemfc/battery pack power system for a bus application. *Applied Energy*, 97:777 – 784, 2012. ISSN 0306-2619. doi: https://doi.org/10.1016/j.apenergy.2011.11.043. URL http://www.sciencedirect.com/science/article/pii/S0306261911007409. Energy Solutions for a Sustainable World - Proceedings of the Third International Conference on Applied Energy, May 16-18, 2011 - Perugia, Italy.

[6] P. Berg, K. Promislow, J. St. Pierre, J. Stumper, and B. Wetton. Water management in pem fuel cells. *Journal of the Electrochemical Society*, 151 (3):A341–A353, 2004.

[7] D. M. Bernardi and M. W. Verbrugge. Mathematical model of a gas diffusion electrode bonded to a polymer electrolyte. *AIChE journal*, 37(8): 1151–1163, 1991.

[8] T. Berning, D. M. Lu, and N. Djilali. Three-dimensional computational analysis of transport phenomena in a pem fuel cell. *Journal of Power Sources*, 106(1):284–294, 2002.

[9] T. Berning, M. Odgaard, and S. K. Kær. A computational analysis of multiphase flow through pemfc cathode porous media using the multifluid approach. *Journal of the Electrochemical Society*, 156(11):B1301–B1311, 2009.

[10] V. J. Bharath, J. Millichamp, T. P. Neville, T. J. Mason, P. R. Shearing, R. J. C. Brown, G. Manos, and D. J. L. Brett. Measurement of water uptake in thin-film nafion and anion alkaline exchange membranes using the quartz crystal microbalance. *Journal of Membrane Science*, 497: 229 – 238, 2016. ISSN 0376-7388. doi: https://doi.org/10.1016/j.memsci.2015.09.027. URL http://www.sciencedirect.com/science/article/pii/S0376738815301915.

[11] R. B. Bird. Transport phenomena. *Applied Mechanics Reviews*, 55(1):R1–R4, 2002.

[12] R. Boddu, U. K. Marupakula, B. Summers, and P. Majumdar. Development of bipolar plates with different flow channel configurations for fuel cells. *Journal of Power Sources*, 189(2):1083–1092, 2009.

[13] V. DAG Bruggeman. Berechnung verschiedener physikalischer konstanten von heterogenen substanzen. i. dielektrizitätskonstanten und leitfähigkeiten der mischkörper aus isotropen substanzen. *Annalen der physik*, 416(7):636–664, 1935.

[14] F. C. Cetinbas, S. G. Advani, and A. K. Prasad. An improved agglomerate model for the pem catalyst layer with accurate effective surface area calculation based on the sphere-packing approach. *Journal of The Electrochemical Society*, 161(6):F803–F813, 2014.

[15] E. Cho, U. S. Jeon, H. Ha, S. A. Hong, and I. Oh. Characteristics of composite bipolar plates for polymer electrolyte membrane fuel cells. *Journal of Power Sources*, 125(2):178–182, 2004.

[16] G. Couture, A. Alaaeddine, F. Boschet, and B. Ameduri. Polymeric materials as anion-exchange membranes for alkaline fuel cells. *Progress in Polymer Science*, 36(11):1521–1557, 2011.

[17] C. E. Damian-Ascencio, A. Saldaña-Robles, A. Hernandez-Guerrero, and S. Cano-Andrade. Numerical modeling of a proton exchange membrane fuel cell with tree-like flow field channels based on an entropy generation analysis. *Energy*, 133:306–316, 2017.

[18] P. K. Das, X. Li, and Z. S. Liu. Analytical approach to polymer electrolyte membrane fuel cell performance and optimization. *Journal of Electroanalytical Chemistry*, 604(2):72–90, 2007.

[19] P. K. Das, X. Li, and Z. S. Liu. A three-dimensional agglomerate model for the cathode catalyst layer of pem fuel cells. *Journal of Power Sources*, 179(1):186–199, 2008.

[20] P. K. Das, X. Li, and Z. S. Liu. Effective transport coefficients in pem fuel cell catalyst and gas diffusion layers: Beyond bruggeman approximation. *Applied Energy*, 87(9):2785 – 2796, 2010. ISSN 0306-2619. doi: https://doi.org/10.1016/j.apenergy.2009.05.006. URL http://www.sciencedirect.com/science/article/pii/S0306261909001974.

[21] D. R. Dekel. Review of cell performance in anion exchange membrane fuel cells. *Journal of Power Sources*, 375:158–169, 2018.

[22] D. R. Dekel, I. G. Rasin, M. Page, and S. Brandon. Steady state and transient simulation of anion exchange membrane fuel cells. *Journal of Power Sources*, 375:191–204, 2018.

[23] H. Deng, S. Huo, Y. Chang, Y. Zhou, and K. Jiao. Transient analysis of alkaline anion exchange membrane fuel cell anode. *International Journal of Hydrogen Energy*, 38(15):6509–6525, 2013.

[24] Q. Duan, S. Ge, and C. Wang. Water uptake, ionic conductivity and swelling properties of anion-exchange membrane. *Journal of Power Sources*, 243: 773–778, 2013.

[25] S. Dutta, S. Shimpalee, and J. W. Van Zee. Three-dimensional numerical simulation of straight channel pem fuel cells. *Journal of Applied Electrochemistry*, 30(2):135–146, 2000.

[26] ANSYS Fluent. Users guide, 2014. 15.

[27] S. Ge, B. Yi, and P. Ming. Experimental determination of electro-osmotic drag coefficient in nafion membrane for fuel cells. *Journal of The Electrochemical Society*, 153(8):A1443–A1450, 2006.

[28] S. H. Ge and B. L. Yi. A mathematical model for pemfc in different flow modes. *Journal of Power Sources*, 124(1):1–11, 2003.

[29] T. Guan, P. Alvfors, and G. Lindbergh. Investigation of the prospect of energy self-sufficiency and technical performance of an integrated pemfc (proton exchange membrane fuel cell), dairy farm and biogas plant system. *Applied Energy*, 130:685 – 691, 2014. ISSN 0306-2619. doi: https://doi.org/10.1016/j.apenergy.2014.04.043. URL http://www.sciencedirect.com/science/article/pii/S0306261914003961.

[30] I. Gunasekara, M. Lee, D. Abbott, and S. Mukerjee. Mass transport and oxygen reduction kinetics at an anion exchange membrane interface: microelectrode studies on effect of carbonate exchange. *ECS Electrochemistry Letters*, 1(2):F16–F19, 2012.

[31] M. Han, J.H. Xu, S. H. Chan, and S. P. Jiang. Characterization of gas diffusion layers for pemfc. *Electrochimica Acta*, 53(16):5361 – 5367, 2008. ISSN 0013-4686. doi: https://doi.org/10.1016/j.electacta.2008.02.057. URL http://www.sciencedirect.com/science/article/pii/S0013468608002879.

[32] M. A. Hickner, A. M. Herring, and E. B. Coughlin. Anion exchange membranes: current status and moving forward. *Journal of Polymer Science Part B: Polymer Physics*, 51(24):1727–1735, 2013.

[33] J. T. Hinatsu, M. Mizuhata, and H. Takenaka. Water uptake of perfluorosulfonic acid membranes from liquid water and water vapor. *Journal of the Electrochemical Society*, 141(6):1493–1498, 1994.

[34] G. Hoogers. *Fuel cell technology handbook*. CRC press, 2002.

[35] J. Huang, Z. Li, and J. Zhang. Review of characterization and modeling of polymer electrolyte fuel cell catalyst layer: The blessing and curse of ionomer. *Frontiers in Energy*, 11(3):334–364, Sep 2017. ISSN 2095-1698. doi: 10.1007/s11708-017-0490-6. URL https://doi.org/10.1007/s11708-017-0490-6.

[36] S. Huo, H. Deng, Y. Chang, and K. Jiao. Water management in alkaline anion exchange membrane fuel cell anode. *International Journal of Hydrogen Energy*, 37(23):18389–18402, 2012.

[37] J. J. Hwang and W. R. Chang. Characteristic study on fuel cell/battery hybrid power system on a light electric vehicle. *Journal of Power Sources*, 207: 111 – 119, 2012. ISSN 0378-7753. doi: https://doi.org/10.1016/j.jpowsour.2012.02.008. URL http://www.sciencedirect.com/science/article/pii/S0378775312003096.

[38] G. Inoue and M. Kawase. Effect of porous structure of catalyst layer on effective oxygen diffusion coefficient in polymer electrolyte fuel cell. *Journal of Power Sources*, 327:1 – 10, 2016. ISSN 0378-7753. doi: https://doi.org/10.1016/j.jpowsour.2016.07.037. URL http://www.sciencedirect.com/science/article/pii/S037877531630893X.

[39] T. Isomura, K. Fukuta, H. Yanagi, S. Ge, and C. Y. Wang. Impact of low cathode humidification on alkaline membrane fuel cell performance. In *Meeting Abstracts*, number 6, pages 221–221. The Electrochemical Society, 2011.

[40] E. Jannelli, M. Minutillo, and A. Perna. Analyzing microcogeneration systems based on lt-pemfc and ht-pemfc by energy balances. *Applied Energy*, 108:82 – 91, 2013. ISSN 0306-2619. doi: https://doi.org/10.1016/j.apenergy.2013.02.067. URL http://www.sciencedirect.com/science/article/pii/S0306261913001864.

[41] K. Jiao and X. Li. Three-dimensional multiphase modeling of cold start

processes in polymer electrolyte membrane fuel cells. *Electrochimica Acta*, 54(27):6876–6891, 2009.

[42] K. Jiao, P. He, Q. Du, and Y. Yin. Three-dimensional multiphase modeling of alkaline anion exchange membrane fuel cell. *International Journal of Hydrogen Energy*, 39(11):5981–5995, 2014.

[43] K. Jiao, S. Huo, M. Zu, D. Jiao, J. Chen, and Q. Du. An analytical model for hydrogen alkaline anion exchange membrane fuel cell. *International Journal of Hydrogen Energy*, 40(8):3300 – 3312, 2015. ISSN 0360-3199. doi: https://doi.org/10.1016/j.ijhydene.2014.12.091. URL http://www.sciencedirect.com/science/article/pii/S0360319914034880.

[44] R. B. Kaspar, M. P. Letterio, J. A. Wittkopf, K. Gong, S. Gu, and Y. Yan. Manipulating water in high-performance hydroxide exchange membrane fuel cells through asymmetric humidification and wetproofing. *Journal of The Electrochemical Society*, 162(6):F483–F488, 2015.

[45] G. Kaur. *Solid Oxide Fuel Cell Components*. Springer, 2015.

[46] P. S. Khadke and U. Krewer. Mass-transport characteristics of oxygen at pt/anion exchange ionomer interface. *The Journal of Physical Chemistry C*, 118(21):11215–11223, 2014.

[47] N. Khajeh-Hosseini-Dalasm, M. J. Kermani, D. G. Moghaddam, and J. M. Stockie. A parametric study of cathode catalyst layer structural parameters on the performance of a pem fuel cell. *International journal of hydrogen energy*, 35(6):2417–2427, 2010.

[48] Y. S. Kim and K. S. Lee. Fuel cell membrane characterizations. *Polymer Reviews*, 55(2):330–370, 2015. doi: 10.1080/15583724.2015.1011275. URL https://doi.org/10.1080/15583724.2015.1011275.

[49] T. J. Ko, S. H. Kim, B. K. Hong, K. R. Lee, K. H. Oh, and M. W. Moon. High performance gas diffusion layer with hydrophobic nanolayer under a supersaturated operation condition for fuel cells. *ACS applied materials and interfaces*, 7(9):5506–5513, 2015.

[50] K. Kreuer. *Fuel cells: selected entries from the encyclopedia of sustainability science and technology*. Springer Science & Business Media, 2012.

[51] I. Kruusenberg, L. Matisen, Q. Shah, A. M. Kannan, and K. Tammeveski. Non-platinum cathode catalysts for alkaline membrane fuel cells. *International Journal of Hydrogen Energy*, 37(5):4406–4412, 2012.

[52] L. K. Kwac and H. G. Kim. Investigation of gas flow characteristics in proton exchange membrane fuel cell. *Journal of mechanical science and technology*, 22(8):1561–1567, 2008.

[53] Y. Leng, L. Wang, M. A. Hickner, and C. Y. Wang. Alkaline membrane fuel cells with in-situ cross-linked ionomers. *Electrochimica Acta*, 152:93–100, 2015.

[54] M. C. Leverett. Capillary behavior in porous solids. *Transactions of the AIME*, 142(01):152–169, 1941.

[55] X. Li. *Principles of fuel cells*. CRC Press, 2005.

[56] Y. Li, T. Zhao, and W. Yang. Measurements of water uptake and transport properties in anion-exchange membranes. *International Journal of Hydrogen Energy*, 35(11):5656–5665, 2010.

[57] X. Liu, G. Lou, and Z. Wen. Three-dimensional two-phase flow model of proton exchange membrane fuel cell with parallel gas distributors. *Journal of Power Sources*, 195(9):2764–2773, 2010.

[58] K. W. Lum and J. J. McGuirk. Three-dimensional model of a complete polymer electrolyte membrane fuel cell–model formulation, validation and parametric studies. *Journal of Power Sources*, 143(1):103–124, 2005.

[59] B. S. Machado, N. Chakraborty, and P. K. Das. Influences of flow direction, temperature and relative humidity on the performance of a representative anion exchange membrane fuel cell: A computational analysis. *International Journal of Hydrogen Energy*, 42(9):6310 – 6323, 2017. ISSN 0360-3199. doi: https://doi.org/10.1016/j.ijhydene.2016.12.003. URL http://www.sciencedirect.com/science/article/pii/S036031991633542X.

[60] B. S. Machado, N. Chakraborty, M. Mamlouk, and P. K. Das. A three-dimensional agglomerate model of an anion exchange membrane fuel cell. *Journal of Electrochemical Energy Conversion and Storage*, 15(1):011004, 2018.

[61] G. Merle, M. Wessling, and K. Nijmeijer. Anion exchange membranes for alkaline fuel cells: A review. *Journal of Membrane Science*, 377(1):1–35, 2011.

[62] J. Mishler, Y. Wang, R. Mukundan, J. Spendelow, D. S. Hussey, D. L. Jacobson, and R. L. Borup. Probing the water content in polymer electrolyte fuel cells using neutron radiography. *Electrochimica Acta*, 75:1–10, 2012.

[63] P. D. Neufeld, A. R. Janzen, and R. A. Aziz. Empirical equations to calculate 16 of the transport collision integrals ω (l, s)* for the lennard-jones (12–6) potential. *The Journal of Chemical Physics*, 57(3):1100–1102, 1972.

[64] M. Nie, L. Y. Zhang, C. Y. Jiang, X. H. Tian, Q. Li, X. W. Liu, S. J. Du, S. Lu, D. Lei, X. H. Wang, J. H. Yuan, Z. Z. Zhao, and M. Z. Wu. New energy and new power–the prospect of increasing use of polymers in fuel cells. *Plastics, Rubber and Composites*, 45(1):31–42, 2016.

[65] T. J. Omasta, L. Wang, X. Peng, C. A. Lewis, J. R. Varcoe, and W. E. Mustain. Importance of balancing membrane and electrode water in anion exchange membrane fuel cells. *Journal of Power Sources*, 375:205 – 213, 2018. ISSN 0378-7753. doi: https://doi.org/10.1016/j.jpowsour.2017.05.006. URL http://www.sciencedirect.com/science/article/pii/S0378775317306274.

[66] Z. Pan, L. An, T. S. Zhao, and Z. K. Tang. Advances and challenges in alkaline anion exchange membrane fuel cells. *Progress in Energy and Combustion Science*, 66:141–175, 2018.

[67] A. Parthasarathy, S. Srinivasan, A. J. Appleby, and C. R. Martin. Pressure dependence of the oxygen reduction reaction at the platinum microelectrode/nafion interface: electrode kinetics and mass transport. *Journal of the Electrochemical Society*, 139(10):2856–2862, 1992.

[68] S. Patankar. *Numerical heat transfer and fluid flow*. CRC press, 1980.

[69] S. Peng, J. Gong, X. Xu, P. C. Sui, S. Lu, and Y. Xiang. Numerical and experimental analyses on deviated concentration loss with alkaline anion-exchange membrane fuel cells. *The Journal of Physical Chemistry C*, 119 (43):24276–24281, 2015.

[70] I. Pilatowsky, R. J. Romero, C. A. Isaza, S. A. Gamboa, P. J. Sebastian, and W. Rivera. *Thermodynamics of Fuel Cells*, pages 25–36. Springer London, London, 2011. ISBN 978-1-84996-028-1. doi: 10.1007/978-1-84996-028-1_2. URL https://doi.org/10.1007/978-1-84996-028-1_2.

[71] J. Ran, L. Wu, Q. Ge, Y. Chen, and T. Xu. High performance anion exchange membranes obtained through graft architecture and rational cross-linking. *Journal of Membrane Science*, 470:229–236, 2014.

[72] R. C. Reid, J. M. Prausnitz, and B. E. Poling. The properties of gases and liquids. 1987.

[73] X. Ren, S. C. Price, A. C. Jackson, N. Pomerantz, and F. L. Beyer. Highly conductive anion exchange membrane for high power density fuel-cell performance. *ACS applied materials & interfaces*, 6(16):13330–13333, 2014.

[74] Y. W. Rho, S. Srinivasan, and Y. T. Kho. Mass transport phenomena in proton exchange membrane fuel cells using o2/he, o2/ar, and o2/n2 mixtures ii. theoretical analysis. *Journal of the Electrochemical Society*, 141(8):2089–2096, 1994.

[75] Y. W. Rho, O. A. Velev, S. Srinivasan, and Y. T. Kho. Mass transport phenomena in proton exchange membrane fuel cells using o2/he, o2/ar, and o2/n2 mixtures i. experimental analysis. *Journal of the Electrochemical Society*, 141(8):2084–2089, 1994.

[76] D. H. Schwarz and N. Djilali. 3d modeling of catalyst layers in pem fuel cells effects of transport limitations. *Journal of the Electrochemical Society*, 154(11):B1167–B1178, 2007.

[77] Z. Siroma, S. Watanabe, K. Yasuda, K. Fukuta, and H. Yanagi. Mathematical modeling of the concentration profile of carbonate ions in an anion exchange membrane fuel cell. *Journal of The Electrochemical Society*, 158 (6):B682–B689, 2011.

[78] Y. J. Sohn, J. Choi, and K. Kim. Numerical analysis on water transport in alkaline anion exchange membrane fuel cells. *Electrochemistry*, 83(2): 80–83, 2015. doi: 10.5796/electrochemistry.83.80.

[79] T. E. Springer, TA Zawodzinski, and S. Gottesfeld. Polymer electrolyte fuel cell model. *Journal of the Electrochemical Society*, 138(8):2334–2342, 1991.

[80] W. Sun, B. A. Peppley, and K. Karan. An improved two-dimensional agglomerate cathode model to study the influence of catalyst layer structural parameters. *Electrochimica acta*, 50(16-17):3359–3374, 2005.

[81] A. Suzuki, U. Sen, T. Hattori, R. Miura, R. Nagumo, H. Tsuboi, N. Hatakeyama, A. Endou, H. Takaba, M. C. Williams, and A. Miyamoto. Ionomer content in the catalyst layer of polymer electrolyte membrane fuel cell (pemfc): Effects on diffusion and performance. *International Journal of Hydrogen Energy*, 36(3):2221 – 2229, 2011. ISSN 0360-3199. doi: https://doi.org/10.1016/j.ijhydene.2010.11.076. URL http://www.sciencedirect.com/science/article/pii/S0360319910022913. The Third Annual International Conference on Hydrogen Safety.

[82] Y. R. J. Thomas, A. Benayad, M. Schroder, A. Morin, and J. Pauchet. New method for super hydrophobic treatment of gas diffusion layers for proton exchange membrane fuel cells using electrochemical reduction of diazonium salts. *ACS applied materials and interfaces*, 7(27):15068–15077, 2015.

[83] K. M. S. Uddin, L. K. Saha, and N. Oshima. Water transport through the membrane of pem fuel cell. *American Journal of Computational and Applied Mathematics*, 4(6):225–238, 2014.

[84] J. R. Varcoe, P. Atanassov, D. R. Dekel, A. M. Herring, M. A. Hickner, P. A. Kohl, A. R. Kucernak, W. E. Mustain, K. Nijmeijer, K. Scott, T. Xu, and

L. Zhuang. Anion-exchange membranes in electrochemical energy systems. *Energy & environmental science*, 7(10):3135–3191, 2014.

[85] H. K. Versteeg and W. Malalasekera. *An introduction to computational fluid dynamics: the finite volume method*. Pearson Education, 2007.

[86] C. Wang. Fundamental models for fuel cell engineering. *Chemical reviews*, 104(10):4727–4766, 2004.

[87] J. Wang and H Wang. Flow-field designs of bipolar plates in pem fuel cells: Theory and applications. *Fuel cells*, 12(6):989–1003, 2012.

[88] Y. J. Wang, J. Qiao, R. Baker, and J. Zhang. Alkaline polymer electrolyte membranes for fuel cell applications. *Chemical Society Reviews*, 42(13): 5768–5787, 2013.

[89] A. Z. Weber and J. Newman. Coupled thermal and water management in polymer electrolyte fuel cells. *Journal of The Electrochemical Society*, 153 (12):A2205–A2214, 2006.

[90] J. A. Wrubel, A. A. Peracchio, B. N. Cassenti, T. D. Myles, K. N. Grew, and W. K. S. Chiu. Anion exchange membrane ionic conductivity in the presence of carbon dioxide under fuel cell operating conditions. *Journal of The Electrochemical Society*, 164(12):F1063–F1073, 2017.

[91] H. Wu. Mathematical modeling of transient transport phenomena in pem fuel cells. 2009.

[92] H. Wu, X. Li, and P. Berg. On the modeling of water transport in polymer electrolyte membrane fuel cells. *Electrochimica Acta*, 54(27):6913–6927, 2009.

[93] L. Xing, M. Mamlouk, and K. Scott. A two dimensional agglomerate model for a proton exchange membrane fuel cell. *Energy*, 61:196–210, 2013.

[94] L. Xing, X. Song, K. Scott, V. Pickert, and W. Cao. Multi-variable optimisation of pemfc cathodes based on surrogate modelling. *international journal of hydrogen energy*, 38(33):14295–14313, 2013.

[95] L. Xing, X. Liu, T. Alaje, R. Kumar, M. Mamlouk, and K. Scott. A two-phase flow and non-isothermal agglomerate model for a proton exchange membrane (pem) fuel cell. *Energy*, 73:618–634, 2014.

[96] L. Xing, M. Mamlouk, R. Kumar, and K. Scott. Numerical investigation of the optimal nafion® ionomer content in cathode catalyst layer: an agglomerate two-phase flow modelling. *international journal of hydrogen energy*, 39(17):9087–9104, 2014.

[97] L. Xing, P. K. Das, X. Song, M. Mamlouk, and K. Scott. Numerical analysis of the optimum membrane/ionomer water content of pemfcs: The interaction of nafion® ionomer content and cathode relative humidity. *Applied Energy*, 138:242–257, 2015.

[98] J. Xu, P. Gao, and T. S. Zhao. Non-precious co3o4 nano-rod electrocatalyst for oxygen reduction reaction in anion-exchange membrane fuel cells. *Energy & Environmental Science*, 5(1):5333–5339, 2012.

[99] J. Yan and M. A. Hickner. Anion exchange membranes by bromination of benzylmethyl-containing poly (sulfone) s. *Macromolecules*, 43(5):2349–2356, 2010.

[100] R. Zeng, J. Handsel, S. D. Poynton, A. J. Roberts, R. C. T. Slade, H. Herman, D. C. Apperley, and J. R. Varcoe. Alkaline ionomer with tuneable water uptakes for electrochemical energy technologies. *Energy & Environmental Science*, 4(12):4925–4928, 2011.

[101] H. Zhang, H. Ohashi, T. Tamaki, and T. Yamaguchi. Water movement in a solid-state alkaline fuel cell affected by the anion-exchange pore-filling membrane properties. *The Journal of Physical Chemistry C*, 117(33):16791–16801, 2013.

[102] Y. Zhao, H. Yu, F. Xie, Y. Liu, Z. Shao, and B. Yi. High durability and hydroxide ion conducting pore-filled anion exchange membranes for alkaline fuel cell applications. *Journal of Power Sources*, 269:1–6, 2014.

[103] N. Ziv, W. E. Mustain, and D. R. Dekel. The effect of ambient carbon dioxide on anion-exchange membrane fuel cells. *ChemSusChem*, 11(7):1136–1150, 2018.